The interaction between oscillating-grid turbulence and a sediment layer

Wan Hanna Melini Wan Mohtar

A thesis submitted to the University of Nottingham for the degree of Doctor of Philosophy

School of Civil Engineering
University of Nottingham

The University of Nottingham

12th October 2011

To my parents, who always believed in me,

and,

to my children, in whom I'll always believe ...

Abstract

The critical conditions for incipient sediment motion induced by oscillating-grid gene-rated turbulence interacting with a sloping sediment layer were investigated experimentally. Near-spherical monodisperse sediments were used throughout with relative densities of 1.2 and 2.5 and mean diameters (d) ranging between 80 and 1087 μm. Interaction characte-ristics were analysed in terms of the critical Shields parameter θ_c, defined using the peak root mean square (r.m.s) horizontal velocity component in the near-bed region. Bed slope effects on θ_c were investigated by tilting the bed (and the grid) at angles between 0 and the repose limit. In all cases, the grid was aligned to be parallel to the bed surface, so that the oscillation direction is always normal to bed surface. The measured values of θ_c on a horizontal bed were comparable to the values reported in the traditional Shields diagram with θ_c seen to increase monotonically for hydraulically smooth bedforms and to be approximately constant for hydraulically rough bedforms. To account for bed slope effects, the measured values of θ_c were compared with a force-balance model based on the conditions for incipient grain motion on a sloping bed. For hydraulically smooth bedforms, where the bed roughness is small compared to the boundary-layer depth, the model was derived to account for how viscous stresses act to damp the drag and lift forces acting on the near surface sediment. For hydraulically rough bedforms, where this viscous-damping effect is not present, the model assumes the standard approach with the drag and lift forces scaling with the square of the near-bed (inviscid) velocity scale. In both cases the model predicts the bedforms to become more mobile as the bed slope is increased. However, the damping effect of the viscous sublayer acts as a stabilizing influenced for hydraulically smooth bedforms, to reduce the rate at which the bed mobility increases with bed slope. The measured values of θ_c in the hydraulically rough bedforms were in agreement with the trends predicted by this model. However, measured θ_c in smooth bed cases were lower than predicted, and fall on the hydraulically rough trend when bed slope is $< 20°$. When the bed slope reaches the repose limit, θ_c falls between the smooth-bed and rough-bed cases. Measurements of sediment trajectories due to the turbulence interacting with the bed were obtained, for a range of impact conditions. Observations of the sediment trajectories du-ring the interaction show the individual sediment grains to be predominantly displaced in a circular 'splash'. Data showed that the 'splash' feature and particle entrainment within the turbulence structure was within one eddy turnover time.

Acknowledgment

Words cannot describe how much I am in debt to my supervisor, Dr Rick Munro for his supports, meetings, discussions, time and continuous interest in supervising me. But mostly, I thank him for his patience.

Big appreciation also is conveyed to my internal examiners, Dr Matthew Scase and Dr John Owen who have contributed valuable ideas and suggestions.

A big thank you goes to the Civil Engineering technicians especially Damien Goy, Mike Langford and Andy Stone who helped me with experimental setup, and have treated me with kindness during my stay in the L2 lab.

Next, I would like to give a warm and well deserved appreciation to my lunchmates, Zainab, Hetty, Yam and my officemates, Bro Amanullah, Ka Sarkawt, Ka Botan, Bro Salah and Sydney. Their genuine friendship and the support offered during the time of struggling or when the motivation hits low is much cherished. Although I am not in the same room with other students in EFM, whenever problem arise, they have been helpful. To Bruce, Julia, Athina and Evgenia, I thank you.

I am forever thankful to the Government of Malaysia and Universiti Kebangsaan Malaysia who has financed my study and granted me the study leave.

Throughout my life, my family particularly my parents, Cik and Ayoh have been my biggest supporters. Without their inspiration, prayers and unconditional love, I would not be who I am today, nor would I have accomplished as much I have. Also to my dearest brothers and sisters, who have shared, and together made my life journey a wonderful one. I am also blessed to have the supports from my extended family, true friends and wonderful people around me. Their encouragement whether direct or indirectly given are truly valued.

My daughter Suri Shahnaz, who came into the world at the beginning of my PhD, is one of the person I personally need to thank too. Although she is small and only cares about Disney princesses, she is definitely in her own way understands of the important task her mother needs to do. And last but not least, this thesis would not be materialised without the strength and supports shown by my husband, Izzi, who shared my tears, especially throughout the grueling writing period. Although I did not put you in dedication, I hope you know that I have dedicated my life to you.

Contents

List of Tables

List of Figures

Chapter 1

Introduction

1.1 Background

This study focussed on bed-load sediment transport in water flows. The erosion, transport and re-deposition of sediments in the near-bed region are important phenomena in many industrial, environmental and geophysical processes. Typical examples include the erosion and reshaping of coast lines and river basins, the reduction of soil fertility, sewage outflow and filtration systems and the contamination of drinking water supplies in developing countries. A problem of great significance on a geophysical scale is the transfer of sediments from the land into the oceans by the combined effects of coastal, river and wind erosion. It has been estimated that the global flux of sediment from the continents into the oceans is over 18 billion tons per year, of which over 64% is deposited due to the suspended sediment loads carried by the world's rivers, with the largest deposits being from rivers like the Amazon, Brahmupatra and Ganges (Chakrapani, 2005).

Important parameters in predicting bed-load sediment transport in water flow are the fluid forces acting on the particles. Movement of the near-surface sediment is governed by the drag F_D and lift forces F_L acting on the exposed grains, which are dependent, respectively on the local flow velocity and the velocity gradient in the vicinity of the sediments. A sediment particle will be set into motion when the hydrodynamic fluid forces F_D and F_L overcome the stabilizing forces of submerged particle weight and bed friction. Force balance models give the fundamental quantity used to describe bedload sediment transport as the dimensionless Shields parameter θ (Shields, 1936), defined as

$$\theta = \frac{\tau_b}{(\rho_s - \rho)gd}, \tag{1.1}$$

where $\tau_b = \rho u_*^2$ is the bed shear stress, u_* is shear velocity, i.e. a characteristic velocity defined at near-bed region, d the mean grain diameter and ρ_s and ρ are the sediment and fluid densities, respectively. The concept of using τ_b arises from the fact that in steady, uniform flows, the statistics of the near-bed turbulence scale with the shear velocity u_*.
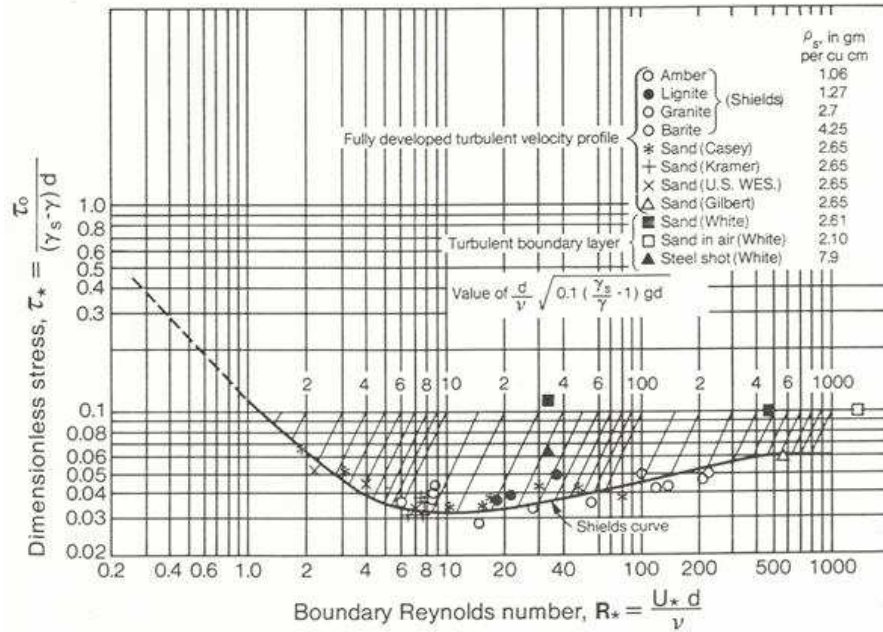
Figure 1.1: Modified Shields diagram, Vanoni (1975). The boundary Reynolds number R_* is equivalent to Re_* and τ_* is equivalent to θ_c defined in this thesis .

Predictive formulae for bedload transport are mainly defined in terms of θ and the critical Shields parameter

$$\theta_c = \frac{\tau_{bc}}{(\rho_s - \rho)gd}, \tag{1.2}$$

where $\tau_{bc} = \rho u_{*c}$ is the corresponding critical (or threshold) bed shear stress and u_{*c} is the critical shear velocity. The determination of θ_c provides an approximation of the conditions under which particle is brought into motion from being stationary, and is the most fundamental parameter in the field of sediment transport mechanics. Pioneering work on measuring θ_c for a wide range of particle sizes and densities was conducted via

laboratory simulated open channel flow by Shields (1936). The values of θ_c were obtained by a reference-based method, extrapolating paired measurements of shear stress and bedload transport rate to a zero level of sediment transport. His work provides a fundamental means or basis of determining θ_c as a function of a particle's Reynolds number $Re_* = u_{*c}d/\nu$ in the Shields diagram, shown here in its modified form in Figure 1.1. Re_* describes the near bed flow features, which depend on the physical sediment characteristics (i.e. size d and bed roughness k_s) and the flow condition (i.e. the thickness of viscous sublayer δ_v). Bed roughness or grain roughness is usually presented in terms of the diameter (or size) of a particle in the sediment bed. If the particles are fully submerged within the viscous sublayer (that is a thin layer developed adjacent to the sediment bed where the flow within is laminar), the bed flow is considered to be hydraulically smooth, that is the effect of viscous forces acting on particles is significant. If there are particles height larger than δ_v, the flow then is described as hydraulically rough. The transition between hydraulically smooth to rough bedforms is the transitional region, that is the size of particle is comparable to the viscous sublayer. Shields (1936) identified the limit of the three aforementioned regions in terms of bed roughness, i.e., the bed flow is hydraulically smooth when $d/\delta_v < 5$, transitional when $5 \leq d/\delta_v \leq 70$ and rough when $d/\delta_v > 70$. Note that as $\delta_v \sim \nu/u_*$, the particle Reynolds number $Re_* \sim d/\delta_v$.

The Shields diagram was developed from bed shear stress data measured in a steady turbulent channel flow. In such flows, the flow near the bed is simplified by the fact that the statistical distribution of the turbulent fluctuations, which give rise to the hydrodynamic drag and lift forces that induce sediment motion, are scaled with the mean averaged velocity. Hence, the integral parameter used in standard models (as used in Shields and other studies) is the time-averaged mean bed shear stress. However, it has been found that using θ_c obtained from the Shields diagram often yields poor and inconsistent results when applied to real flows or in complex flows (Paintal, 1971; Shvidchenko and Pender, 2000; Wu et al., 2008). This is due to the fact that in such flows where the simplifications of uniformity and stationarity no longer hold, the intensity of turbulent fluctuations in the near-bed region can vary significantly with bed position and time. This is because of factors such as external turbulence generated by flow obstacles (Sumer et al., 2003), local bed geometry (Nelson et al., 1995) or intermittent bursting and ejection events associated with the development of coherent vortex structures within the near bed region (Niño and Garcia, 1996). In such scenarios, the turbulent fluctuations near the bed no longer scale with the mean flow characteristics and the θ_c value obtained from the Shields curve is no

longer valid. Despite this, the Shields diagram is still the most widely used and accepted criterion.
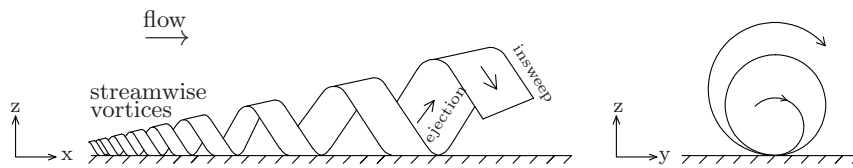
Figure 1.2: A funnel vortex. Redrawn from Kaftori (1995a).

The aforementioned studies propose that sediment transport is predominantly driven by the fluctuating drag and lift forces exerted on exposed sediment grains. It has been suggested that critical sediment motion is best represented by the maximum forces acting on the particles rather than the mean bed shear stress (Giménez-Curto and Corniero, 2009). These fluctuating forces are directly related to the instantaneous fluctuating velocities, indicating that the turbulence structure at near bed is ultimately responsible for sediment entrainment (McLean, 1994). Clearly, clarification of the complex and intermittent turbulence-sediment interaction in the near-bed region is required. Recent studies have attempted to examine the role played by (unsteady) coherent vortex structures in the entrainment and transport of sediments. Funnel-shaped streamwise vortices (as shown in Figure 1.2) have the potential to develop in near-bed region of a turbulent channel flow. These coherent turbulent structures displace the sediment into narrow, longitudinal troughs and ridges (by the streamwise vortices) or entrain the sediments from the bed and into the outer flow through an ejection-sweep cycle (bursting phenomena) (Sumer and Deigaard, 1981; Kaftori et al., 1995; Niño and Garcia, 1996). Ejection events resuspend the particles to the outer flow whilst sweep events transport the suspended particles back to the sediment bed. This near-bed coherent structure is present in both hydraulically smooth and rough regions (Sumer and Deigaard, 1981). Munro et al. (2009) identified analogous behaviour using an isolated coherent vortex structure in the form of vortex ring interacting with (artificial) sediment layer thereby, inducing sediment erosion. In the same study, a light attenuation technique was used to obtain detailed time resolved measurements of sediment erosion levels during the interaction period, and over the entire impact region. It was shown by Munro et al. (2009) that, during this interaction, the intense vortical flow establishes local regions of high-momentum fluid (or sweeps) immediately above the bed surface which distort (or disrupt) the structure of the boundary layer and inner viscous sublayer. Consequently, the adjacent near-surface sediment is exposed to increased

hydrodynamic drag and lift forces. The aforementioned study suggests that under the appropriate conditions, the exposed sediment can be displaced along the bed to accumulate in near-by regions of comparatively low-momentum fluid, or resuspended into the outer fluid above the bed surface. All of the studies mentioned so far focussed on the significant contribution of turbulence or energetic burst and identified the bed roughness length-scale and the viscous sublayer thickness as the key factors controlling sediment displacement and resuspension.

The Shields diagram and most of the critical sediment motion related studies have developed empirical predictive formulae based on a horizontal or nearly horizontal bed. However in many naturally occurring flows, the bed is not typically a horizontal plane. In spite of this, comparatively few studies have analysed how θ_c is affected by bed slope. Theoretical (force balance) models predict that a sediment bed becomes more mobile (or unstable) as the bed slope is increased, due to the additional down-slope gravitational force (Wiberg and Smith, 1987). The model was derived by analysing forces acting on a sediment particle resting on a non-horizontal bed slope. However, some field studies (Mueller et al., 2005) and open channel experiments (Lamb et al., 2008) have demonstrated the contrary, in asserting that the sediment layer becomes more stable with increasing bed slope. Lamb et al. (2008) attributes this counter-intuitive result to how the near-bed turbulence in a steady open channel flow is affected by the decrease in flow depth (h), and the corresponding increase in relative bed roughness k_s/h, that occurs as the bed slope is increased (where k_s is the roughness length scale). Experimental work in a closed-conduit eliminated the relative roughness effect and confirmed the theoretical prediction (Whitehouse and Hardisty, 1988; Chiew and Parker, 1994; Dey and Debnath, 2000). Chiew and Parker (1994) experimentally measured θ_c in a closed-conduit flow with bed slope varied systematically within a range of $-10°$ (i.e. uphill) to $+31°$ (downhill). Measured θ_c from experimental collapse into the theoretical line, where the theory describes well the incipient condition for the transport of sediments on bed slope, even at high slope angle. Note that the theoretical prediction was developed using velocity profile in turbulent boundary layer i.e., more appropriate for describing the hydraulically rough region. Studies of (Chiew and Parker, 1994) and (Dey and Debnath, 2000) only mainly focussed on the sediments categorised as the hydraulically rough bedforms. However, an accurate prediction of θ_c on fine sediments i.e. hydraulically smooth bedforms using this (force-balance model) theory might not be the case.

The aim of this study is to use zero-mean flow turbulence to analyse how fluctuating

turbulent components interact with a sediment layer, particularly at the threshold of sediment motion. Zero-mean flow turbulence is a turbulent flow which has an approximate zero mean fluid velocities, is isotropic and homogeneous. This isolate the mean flow component and produced dominant fluctuating velocity components. This method has been used previously to investigate geophysical phenomena such as mixing at density interface (Hopfinger and Toly, 1976; Nokes, 1988), turbulence evolution at a near solid boundary (Hannoun et al., 1988; Bodart et al., 2010) and to study how suspended particles affect turbulence (Poelma, 2004). It is worth highlighting that this technique has been used previously to determine conditions for critical sediment motion (Medina, 2002; Bellinsky et al., 2005). This study, however, presents objective experimental work conducted in a more consistent, robust and rigorous manner by addressing the critical velocity scale, a larger variance of Re_* and includes both hydraulically smooth and rough bedforms and also incorporates the effect of bed slope.

1.2 Oscillating grid turbulence

Near homogeneous, zero-mean turbulence can be produced by oscillating a symmetrical grid in a water tank (Hopfinger and Toly, 1976; Atkinson et al., 1987; Bellinsky et al., 2005). The basic oscillating-grid mechanism is shown in Figure 1.3. A symmetric grid is connected to a driving wheel, which oscillates the grid in vertical direction. The grid consists of an array of bars and is positioned below the water surface. The salient aspects to consider in this basic arrangement are the grid design i.e. the mesh size M, the diameter of grid bars d_g and the grid solidity $\sigma = \frac{2Md_g - d_g^2}{M^2}$ (defined as the ratio of the area of bars to the total area of the grid). Mesh size is defined as the distance between the centres of two neighbouring openings. The intensity of the turbulence generated by the oscillating-grid depends on M, d_g, σ as well as stroke S (the distance of half cycle of oscillation) and frequency f_g (the number of oscillation cycles per unit time). The grid consists of an array of bars and is positioned at distance (usually at $2S$) below the water surface.

When the planar horizontal grid starts to oscillate in a direction normal to its plane, it produces a layer of intense turbulent motion near the grid. This layer consists of a wake created by the motion of each of the grid bars and quasi-steady 'jet' flows emerging from the openings of the grid. The continuous periodic grid motion causes the wakes and jets to interact creating a thickened turbulent layer via entrainment of the surrounding fluid. At sufficient distance from the grid, the jet-wake interaction breaks down into turbulence
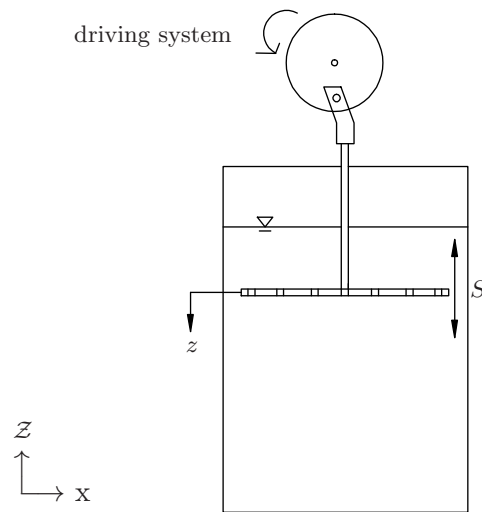
Figure 1.3: Schematic drawing of a typical oscillating-grid setup. In this figure, the grid is positioned at mid-position of the stroke length. The symbol S represents the length of half cycle of oscillation known as stroke and z corresponds to the distance away from grid where $z = 0$ is identified as the virtual origin.
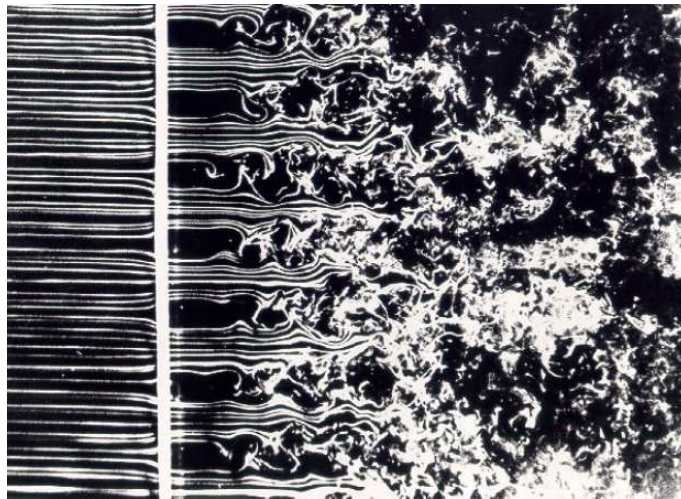
Figure 1.4: A visualization of grid-generated turbulence. Photograph by T. Corke and H. Nagib, reproduced from Van Dyke (1982). This is produced by passing a steady mean flow through a symmetrical (passive) grid.

which is propagated downwards by the jet motions. At distances further away from the grid, the turbulence is considered quasi-isotropic and homogeneous parallel to the grid plane. In the absence of mean velocity (gradients), the homogeneous turbulence spatially decays along vertical direction as there exists no turbulence production to sustain it. In a laboratory frame, the flow is statistically stationary and the turbulence statistics only vary in the direction perpendicular to the grid plane. Utilising this frame of reference, the grid turbulence can be modelled as statistically homogeneous (invariant in translation) and isotropic flow (invariant in rotation). Figure 1.4 shows an example of this type of flow, a snapshot dye visualization in a turbulent flow produced by passing a steady mean flow through a stationary symmetrical grid. It should be emphasised that although this is not oscillating-grid generated turbulence, the basic quasi-isotropic homogeneous turbulence characteristics generated remain the same, in that the turbulence decays in the perpendicular direction to the grid plane.

This form of grid-generated turbulence has been studied for over 80 years, starting as early as 1930's with Rouse (1939), to study the characteristics of sediment suspension. However, the grid turbulence properties and the optimum experimental parameters were neither extensively explored nor discussed. Following this, a detailed turbulence mapping of the bulk of a homogeneous fluid far from the grid started with the experimental work of Turner (1968) and Thompson and Turner (1974). The quasi-isotropic homogeneous region is found at two mesh spacings ($z = 2M$) away from the virtual origin (where the virtual origin describes the reference level ($z = 0$) and is usually taken at the grid midplane) (Atkinson and Damiani, 1986; Cheng and Law, 2007). See Figure 1.3 for a better illustration of the position of the virtual origin. In this kind of turbulent flow, the most appropriate lengthscale is an integral length scale l, a convenient measure of the size of the energy containing (large) eddies. Thompson and Turner (1974), for example, used a hot-film probe rotating on a plane parallel to the grid to obtain the l by an integration of the spatial autocorrelation function of the root mean square (r.m.s.) horizontal velocity components.

Applying the Reynolds decomposition separates the turbulent fluctuating components **u**' from the mean part of the flow velocity **U**. Thus a dynamical equations (from Navier-Stokes equation) governing the fluctuations component can be derived, which directly give the equation for the average kinetic energy per unit mass of the fluctuating motion for constant density flow, and is written (using standard tensor notation) as

$$\left[\frac{\partial}{\partial t} + U_j\frac{\partial}{\partial x_j}\right]k = \frac{\partial}{\partial x_j}\left\{-\frac{1}{\rho}\overline{pu_i'}\delta_{ij} - \frac{1}{2}\overline{q^2u_j'} + 2\nu\overline{s_{ij}u_i'}\right\} - \overline{u_i'u_j'}\frac{\partial U_i}{\partial x_j} - 2\nu\overline{s_{ij}s_{ij}}, \quad (1.3)$$

where $k = \frac{1}{2}(\overline{u_i'^2})$ is the turbulent kinetic energy per unit mass, p' is the pressure fluctuation, ρ the fluid density, s_{ij} is the fluctuating strain-rate tensor and over-bar denotes the averaging over fluctuating components. The term $\overline{q^2} = 2k$. For a statistically stationary (steady) turbulent flow, $\frac{\partial k}{\partial t} \approx 0$. Furthermore, since $U_j \approx 0$ within the quasi-isotropic homogeneous turbulence, it follows that there is no convection of k by the mean flow (giving $U_j\frac{\partial k}{\partial x_j} \approx 0$) and no production of turbulent kinetic energy from the mean flow gradient (leading to $\overline{u_i'u_j'}\frac{\partial U_i}{\partial x_j} \approx 0$). Hence, Equation (1.3) is reduced to the turbulent transport and dissipation terms $\epsilon = 2\nu\overline{s_{ij}s_{ij}}$ only, and is written

$$0 = -\frac{\partial}{\partial x_j}(\frac{1}{\rho}\overline{p'u_j'} - \frac{1}{2}\overline{q^2u_j'} + 2\nu\overline{s_{ij}u_i'}) - \epsilon. \quad (1.4)$$

For the case considered here, the turbulence statistics vary spatially in the vertical z-direction only. Hence, neglecting the viscous transport term $\frac{\partial}{\partial x_j}2\nu\overline{s_{ij}u_i'}$ due to high Reynolds number Re_M (Tennekes and Lumley, 1972), Equation (1.4) is simplified to (reverting back to vector notation, with $x_3 = z, u_3' = w'$)

$$0 = -\frac{\partial}{\partial z}(\frac{1}{\rho}\overline{p'w'} - \frac{1}{2}\overline{q^2w'}) - \epsilon, \quad (1.5)$$

where w' is the vertical fluctuating component.

The term ϵ will be discussed first. The energy dissipation rate ϵ is primarily determined by the large length scales in the turbulent flow. This implies that in homogeneous turbulence, according to Batchelor (1953), an eddy viscosity of order ul is acting on a shear of order u/l to produce a 'dissipation' of energy from the energy-containing eddies to smaller eddies. Thus, the rate of dissipation energy in homogeneous turbulence can be expressed as,

$$\epsilon = A(ul)\frac{u^2}{l^2} = A\frac{u^3}{l}, \quad (1.6)$$

where A is a constant of order unity, $u = (\overline{u'^2})^{1/2}$ is the r.m.s. horizontal velocity and l is the integral length scale. The large scale (energy containing) eddies determine the rate of energy transfer and the small scales convert this energy into heat at similar rate. At

high Reynolds number, the viscous forces in the motion are entirely secondary, and may be ignored for all except the small scale eddies, at which the dissipation occurs (Batchelor, 1953).

The transport (divergence) term in Equation 1.5 is now looked into. The vertical energy flux $\overline{q^2 w'}$ and the pressure term $\overline{p' w'}$ are proportional to u^3 (Hopfinger and Toly, 1976). The term q^2 are $\mathcal{O}(u^2)$, ergo multiply by the vertical velocity w', which is assumed as $w' \approx u'$ due to isotropy, the energy flux term is $\mathcal{O}(u^3)$. Hopfinger and Linden (1982) argued that the pressure fluctuation term $\frac{1}{\rho}\overline{p' w'}$ are equal order of $\frac{1}{2}\overline{w' q^2}$, thus the term $\frac{1}{\rho}\overline{p' w'}$ is $\mathcal{O}(u^3)$. The transport term in Equation (1.5) thus can be written as

$$\frac{1}{\rho}\overline{p' w'} - \frac{1}{2}\overline{q^2 w'} = r u^3, \tag{1.7}$$

where the coefficient $r = 2.2$ when A is unity (Hopfinger and Linden, 1982). Substituting Equation (1.6) and Equation (1.7) into Equation (1.5), the energy equation can be written as

$$\frac{du^3}{dz} = -\frac{B u^3}{l}, \tag{1.8}$$

where $B = A/r$. It was demonstrated that the integral lengthscale l increases linearly with increased distance from the virtual origin z as $l = \beta_l z$, where β_l is an empirical coefficient (Thompson and Turner, 1974). Substituting $l = \beta_l z$ into Equation (1.8) and integrating gives

$$u = u_0 (z/z_0)^{-B/3\beta_l}, \tag{1.9}$$

where $u = u_0$ at $z = z_0$.

Hopfinger and Toly (1976), who employed oscillating-grid to generate turbulence to investigate turbulence mixing at density interface, incorporated the grid geometry M, stroke S and frequency of oscillation f_g into Equation (1.9). The horizontal r.m.s. turbulent velocity u (which was obtained experimentally) was logarithmically plotted as a function of distance z and a relation of $u \propto z^{-n_u}$ with n_u close to 1 was obtained. Furthermore, Hopfinger and Toly (1976) also obtained a near constant B/β_l (value of 3), although β_l and B were found to be individually varied with the grid geometry and the stroke (Hopfinger and Linden, 1982). Thus, the power $-B/3\beta_l$ in Equation (1.9) gives the value of ≈ 1, comparable with the empirically obtained value of $n_u = 1$.

Incorporating external parameters i.e. grid geometry, oscillation frequency and stroke to Equation (1.9) need expressions for u_0 and z_0. Hopfinger and Toly (1976) found $u_0 = (f_g S) C_u S^{1/2}$ where C_u is the empirical constant and is a function of M and $z_0 \approx M^{1/2}$. By replacing u_0 and z_0 respectively, and proposing a similar derivation for the r.m.s. vertical velocity component (due to isotropy), Equation (1.9) becomes

$$\frac{u}{f_g S} = C_u S^{1/2} M^{1/2} z^{-n_u}, \tag{1.10a}$$

$$\frac{w}{f_g S} = C_w S^{1/2} M^{1/2} z^{-n_w}, \tag{1.10b}$$

where C_u, C_w, n_u, n_w are empirical constants and dependent on the grid parameters S and M (Hopfinger and Linden, 1982). The equation formulated by Hopfinger and Toly (1976) as in Equation (1.10) is henceforth referred to the HT equation in this thesis. Their experiments found the respective constants i.e. C_u, C_w, n_u, n_w to be 0.25, 0.27, 1 and 1, respectively. This equation has been accepted, particularly for horizontal velocity components and is often employed in oscillating-grid turbulence studies, where the range of S are comparable to the values used by Hopfinger and Toly, for example, Silva and Fernando (1994); Cheng and Law (2007); Bellinsky et al. (2005). It should be noted that the utilisation of the linear HT relation is dependent on the grid comprising square bars. Other shapes such as circular bars may have nonlinear relation (Thompson and Turner, 1974).

Equations (1.10) is only valid in the quasi-isotropic homogeneous region, which is usually found at a certain distance away from the grid. Previous studies found that the turbulence decay relationships held when $z > 2M$ or $z > 4S$ for smaller strokes (Hopfinger and Toly, 1976; Atkinson et al., 1987; Silva and Fernando, 1992). To obtain a quasi-isotropic homogeneous turbulence, significant secondary circulation in the water tank should be minimised. The presence of secondary flow produces non-zero mean flow which has a substantial influence on the decay power law, where $n_u \neq 1$ in Equation (1.10a) (Silva and Fernando, 1992; McKenna and McGillis, 2004). To ensure that secondary flow is not generated in the tank, some specific control measures pertaining to the grid design, grid solidity and frequency of the grid oscillation are required. According to Fernando and DeSilva (1993), the grid end condition should be designed in such a way so that the sidewalls act as a plane of symmetry. Furthermore, the distance between the wall and the

grid should be small, in line with usual practice at 3 to 4 mm (Voropayev et al., 1995). Also, the solidity of grid σ should be less than 40% (Mohamed and LaRue, 1990). McDougall (1979) and Shy et al. (1997) also proposed that the frequency of the grid oscillation should not exceed 7 Hz. Failing to comply with the aforementioned measures would result in the creation of large scale secondary flows. It was reported by Fernando and DeSilva (1993) that this type of flow may occur due to the formation of stronger jets near the grid (due to high $\sigma > 0.4$) and these jets continue to carry the mean momentum from the oscillation. Another mechanism is due to the Reynolds shear stress gradients induced by the oscillatory grid motion, which is advected downwards by jets. In this case, an appreciable mean flow would exist $\mathbf{U} \neq 0$ and the turbulent kinetic energy is rapidly propagated downwards away from the grid by the mean flow (Fernando and DeSilva, 1993). When this happens, the turbulence decay is significantly changed and Equation (1.10) is rendered invalid.

1.3 Problem statement

Through an extensive literature review and rigorous experimental work, this study investigates the process of turbulence-sediment interaction and in particular, the critical conditions for the threshold of sediment motion in the presence of zero-mean turbulence generated by an oscillating-grid. The aim is to examine the interaction of zero-mean turbulence with a sediment layer, so that the role of the turbulent fluctuations can be analysed in isolation.

The main objective here is to determine the critical conditions for incipient sediment motion in terms of the critical Shields parameter θ_c, which here is expressed in terms of the r.m.s. turbulent velocity. The variation of θ_c is analysed in terms of its dependency on sediment type (size and relative density), and also in terms of its dependency on bed slope, from the horizontal up to the repose limit. Furthermore, this study focuses on how θ_c varies between the hydraulically rough to hydraulically smooth bed flow regions.

To achieve the overall aim, the experimental rig designed was first tested to assess its ability to generate the quasi-isotropic homogeneous turbulent flows. The grid generated turbulence is calibrated by investigating its agreement with the established universal turbulence decay law as described in Equation (1.10). The velocity measurements are obtained using time-resolved Particle Image Velocimetry (PIV).

In addition, this study also examines the zero-mean turbulence interaction with a horizontal sediment bed and particularly focuses on particle trajectories under the influence

of an energetic eddy. The velocities of displaced sediment grains were obtained using a simple adaptation of standard PIV. This provides a qualitative description on how the turbulence interact and displace the sediments. These experiments were performed with $\theta > \theta_c$, i.e., so that the near-bed turbulence intensity was sufficiently high to exceed the required critical criteria for sediment motion.

1.4 Outline of thesis

The motivation behind this research is that of critical conditions that give rise to incipient sediment motion by turbulence. In this study, grid-generated turbulence is presented using r.m.s. velocity components, a second order turbulence statistics. Key questions to be asked about this are; how is the critical Shields parameter profile against dimensionless grain boundary measured by turbulence? How does bed slope affect the measurement of θ_c?

As the main focus here is the effect of turbulence on incipient sediment motion, turbulence is generated (in the absence of mean flow) by using oscillating-grid. In Chapter 2, analysis of the spatial turbulence characteristics generated in a sediment-free case is conducted. Results obtained are compared to the standard turbulence decay law developed in Hopfinger and Toly (1976). It is found that the turbulence generated is a close approximation of a zero-mean, quasi-isotropic homogeneous turbulence.

In Chapter 3, experimental observations of critical Shields parameter for varying sediment size and density are made. Particular attention is paid to the effect of bed slope. The measured values of θ_c are compared with an established force balance model based on the conditions for incipient grain motion on a sloping bed. The model was re-derived to account separately for smooth and rough bedforms. An alternative approach to investigate the critical conditions for incipient sediment motion is by consider turbulence as an ensemble of elemental vortex structures in the form of vortex ring (Munro et al., 2009). Vortex ring is a simple coherent turbulent structure, and is modeled as a single idealised eddy. Chapter 4 extends the study of Munro et al. (2009) by including the effect of bed slope. Results obtained are compared with the θ_c measured (due to oscillating-grid turbulence) in Chapter 3. Chapter 5 illustrates a qualitative description on how the zero-mean turbulence interacts, and moves the near-surface sediment grains. Finally, in Chapter 6, conclusions of these results are given.

Chapter 2

Oscillating-grid turbulence: System calibration

Experiments were first performed to determine the characteristics of the turbulence produced by the oscillating-grid mechanism. The characteristics were compared with those observed by Hopfinger and Toly (1976) and Thompson and Turner (1974). This chapter is dedicated to determining the spatial variation of turbulence characteristics with distance from the grid, in particular the r.m.s. horizontal velocity u and the integral length scale l.

2.1   Overview of the oscillating-grid turbulence experiments

A schematic representation of the oscillating-grid apparatus used in this study is shown in Figure 2.1. An acrylic tank with dimensions of $35.4 \times 35.4 \,\mathrm{cm}^2$ in cross section and 50 cm in height was used. The tank was placed on a steel frame and partially filled with tap water up to 40 cm. The grid shown in Figure 2.1(b) is a 7×7 array of 1 cm width (d_g) aluminium square bars with grid solidity of 0.36 and a center-to-center mesh size (M) of 5 cm. The grid was positioned 10 cm below the water free surface. The end condition of the grid array is designed in such a way that the wall of tank acted as a plane of symmetry and the gap between the grid and the walls is 2.5 mm. The grid is connected by a 1 cm diameter steel rod through a linear bearing to a circular drive wheel. The stroke of grid oscillation (S) is altered by changing the radius of the circular drive wheel motion. The grid was oscillated in an initially still fluid by applying strokes S between 4 to 10 cm, and the frequency of oscillation was varied between 1 to 6 Hz.
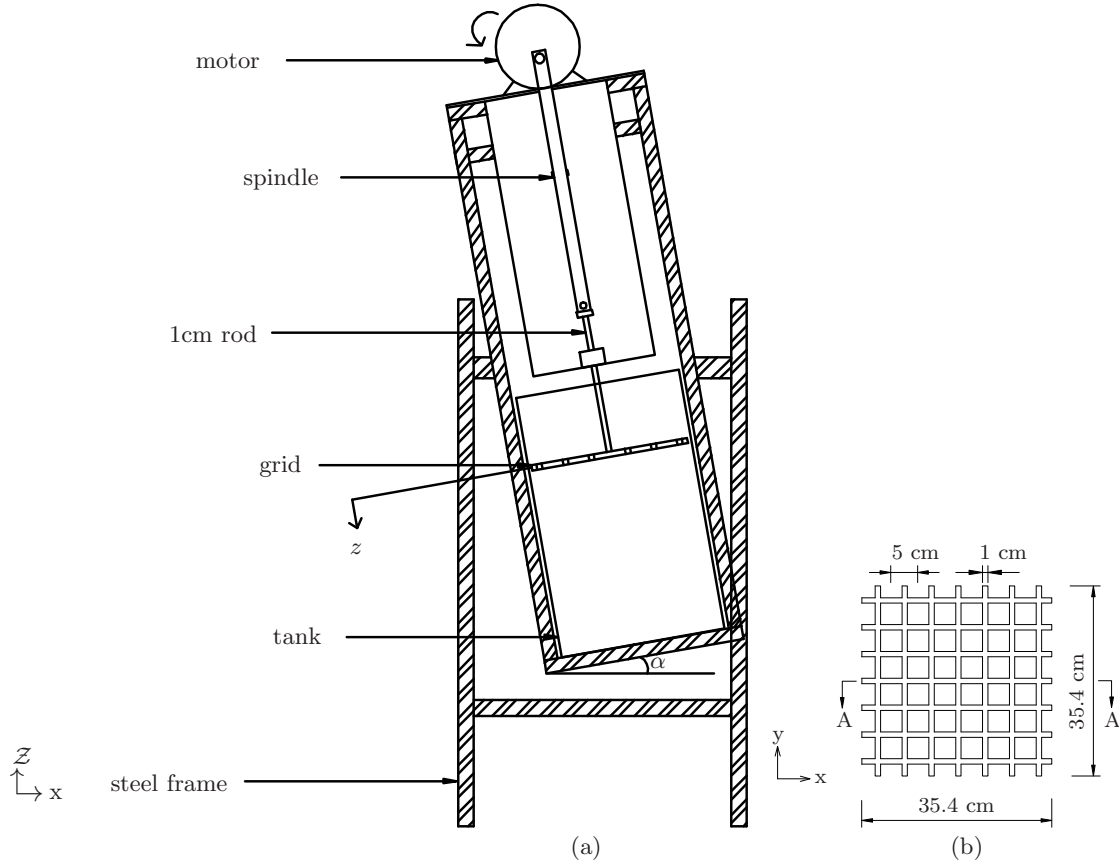
Figure 2.1: The schematic drawing of (a) OGT tank front view and (b) plan view of grid made of crossed bars. Symbols α and z denote the angle of tilted tank and distance from the virtual origin, respectively. A-A in (b) denotes where the light sheet is illuminated, aligned with the central bar at the center of the grid. Note that a hinge was placed to the steel frame to enable the tank to be tilted up to maximum α of 30°.

Label	Stroke, S (cm)	Frequency f_g (Hz)	Reynolds number Re_M ($\times 10^3$)
A1	4	1.5	3.0
A2		3.5	7.0
A3		6	12.0
B4	8	1.3	5.2
B5		3.2	12.8
B6		4.8	19.2
C7	10	1.7	8.5
C8		3.4	17.0
C9		4	20.0

Table 2.1: Summary of the experimental characteristics.

A total of nine experiments were performed and the experimental parameters are listed in Table 2.1. The oscillation frequency f_g was varied by adjusting the motor speed which is regulated by a motor controller. The frequency was calibrated by taking a series of grid oscillation images using a high speed camera and the time for each stroke was calculated. To prevent secondary circulations at high oscillation frequencies, only frequencies less than 6 Hz were considered. The consequent level of turbulence could then be represented by the grid Reynolds number, $Re_M = f_g SM/\nu$, where ν is fluid kinematic viscosity. The turbulent flow condition corresponding to the values of Re_M are shown to lie within the range $3000 < Re_M < 20000$ (see Table 2.1). Figure 2.1 also illustrates that the frame is designed to be able to tilt up to maximum of 30°, simultaneously tilting the sediment bed and the oscillating grid. The experimental procedure which utilises the tilting mechanism is described in the subsequent chapter.

It has been shown previously that the quasi-isotropic homogeneous region exists up to approximately $2M$ away from the virtual origin (Hopfinger and Toly, 1976; Atkinson et al., 1987). This was the basis of the calibration experiments in this study, whereby the grid was placed at the minimum distance of approximately 30 cm from the bottom of the tank. This distance was considered sufficient to eliminate the effects of inhomogeneity resulting from turbulence interaction with the bottom of the tank, at least for the range of Re_M considered.

2.1.1   Details of the PIV measurements

Data acquisition only commenced after at least 5 minutes from the start of oscillation, thereby allowing the turbulence to reach a statistically stationary state. The midplane of the flow field was illuminated by a narrow, vertical light sheet (of thickness 3 mm) coinciding with the midplane of the grid (shown in Figure 2.1(b) as the A-A cross section). The light sheet was generated by two arc lamps, which were placed in a slotted light box (to help channel the light) mounted on an adjustable frame that could be tilted up to $\alpha \leqslant 30°$.

Pliolite particles with nominal diameter d of $200\,\mu$m and has relative density s, compared to water, of 1.02 were used as flow field tracers. Having a seeding density of 6.384×10^{-4}, the tracer particles did not affect to the fluid viscosity. The trajectories of the illuminated particles were recorded using a high speed digital camera (a Dantec Nanosense III, with 1280×1024 pixel resolution and maximum sampling of 1000 Hz), using a 105 mm

Micro Nikkor lens. The images were taken at sampling rate of 200 Hz. The camera was positioned to view horizontally through the front transparent sidewall of the tank (i.e. corresponding to the view shown in Figure 2.1). The field of view from the underside of the grid to the tank bottom corresponded to $20 \times 30 \, \text{cm}^2$.

The velocity profiles were calculated from pairs of images with a cross-correlation algorithm using the commercial software package Digiflow (Dalziel Research). The interrogation area was $20 \times 20 \, \text{pixel}^2$ equivalent to approximately $0.2 \times 0.2 \, \text{cm}^2$, with a 50% overlap between analysis points. Because the interrogation area was 10 times the size of tracer particles, a sufficient amount of particles was permitted within the interrogation window, hence improving the accuracy of the fluid velocity measurements. For each experimental setup, velocity fields were obtained by analysing 18000 to 21000 pairs of images (90 to 105 seconds of sampling time), giving spatial and temporal data of the velocity motions in the fluid.

The pixel image coordinates were converted to physical coordinates using the inherent linear-mapping procedure in Digiflow. For this, an array of $1 \times 1 \, \text{cm}^2$ squares was placed in the light sheet plane and an image was taken. The physical grid was then used to identify orthogonal points that could be used in the mapping procedure. For each set of experiments, the time-resolved fluid velocity data was obtained for the duration of the experiment. The processed velocity fields were used to determine both the mean and r.m.s. horizontal and vertical velocity components.

2.2 Preliminary analysis: Turbulence statistics

2.2.1 Integral length scale and r.m.s. velocity components

Let $\mathbf{u} = (\tilde{u}, \tilde{w})$ denote the velocity components obtained using PIV, where $\tilde{u}(x, z, t)$ and $\tilde{w}(x, z, t)$ denote the horizontal and vertical velocity components, respectively. Using the Reynolds decomposition, the corresponding fluctuating components $u'(x, z, t)$ and $w'(x, z, t)$ can be written as

$$u' = \tilde{u} - \overline{u}, \tag{2.1a}$$

$$w' = \tilde{w} - \overline{w}, \tag{2.1b}$$

where $\overline{u} = \overline{u}(x, z)$ and $\overline{w} = \overline{w}(x, z)$ denote the time-averaged mean velocity components. For each pixel in the PIV image, we have

$$u'_{ijn} = u'(x_i, z_j, t_n), \tag{2.2a}$$

$$w'_{ijn} = w'(x_i, z_j, t_n), \tag{2.2b}$$

where $x_i = i\delta_x$ $(i = 0, 1, ..., L)$, $z_j = j\delta_z$ $(j = 0, 1, ..., K$, and $t_n = n\delta_t$ $(n = 0, 1, ..., N)$, with $\delta_x \approx 0.0192$ cm, $\delta_z \approx 0.019$ cm and $\delta_t = 0.05$ s denote the resolution in x, z and t respectively. Typical values of L, K and N are 1280, 800 and 18000, respectively. Noting that the data obtained in this study are discrete and therefore using overbar notation to denote time averaging, the mean horizontal velocity $\overline{u}$ is defined by,

$$\overline{u}(x_i, z_j) = \frac{1}{N} \sum_{n=1}^{N} \tilde{u}(x_i, z_j, t_n), \tag{2.3}$$

whilst, the root mean square (r.m.s.) horizontal velocity $u(x_i, z_j)$ is defined as

$$u(x_i, z_j) = (\overline{u'^2_{ij}})^{1/2} = \sqrt{\frac{1}{N-1} \sum_{n=1}^{N} (\tilde{u}(x_i, z_j, t_n) - \overline{u}(x_i, z_j))^2}. \tag{2.4}$$

In the same fashion as the equations above, the mean vertical $\overline{w}(x_i, z_j)$ and r.m.s. vertical velocity $w(x_i, z_j) = (\overline{w'^2_{ij}})^{1/2}$ can be defined. Using $<>$ to denote spatial averaging, the variation of turbulence characteristics with distance z is obtained by spatially averaging along x,

$$\langle \overline{u}(z_j) \rangle = \frac{1}{L} \sum_{i=1}^{L} \overline{u}(x_i, z_j), \tag{2.5a}$$

$$\langle u(z_j) \rangle = \frac{1}{L} \sum_{i=1}^{L} u(x_i, z_j). \tag{2.5b}$$

The spatially averaged of mean vertical $\langle \overline{w}(z_j) \rangle$ and the r.m.s. vertical velocity $\langle w(z_j) \rangle$ are defined similarly to Equation (2.5).

The planar velocity measurements obtained enabled a direct evaluation of the spatial autocorrelation of turbulence component over an image area. The integral length scale of
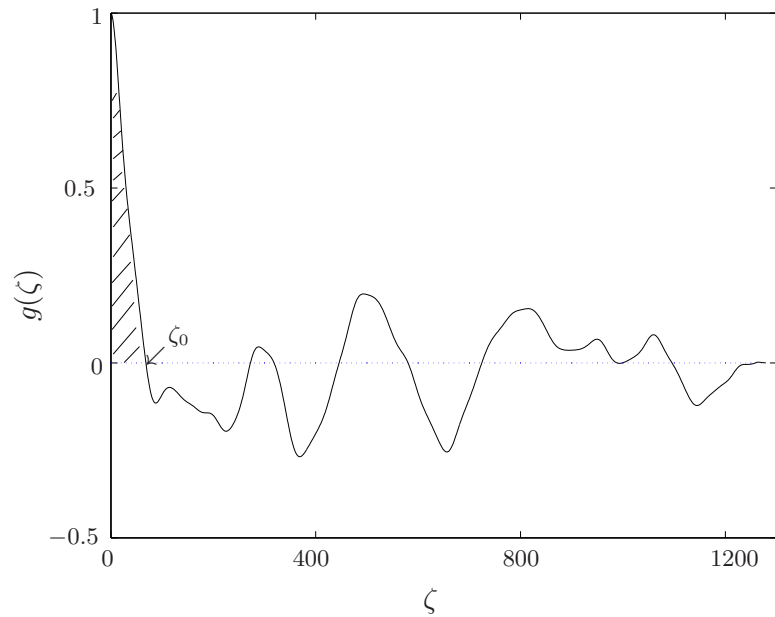
Figure 2.2: An example of normalised autocorrelation function $g(\zeta)$ of r.m.s. horizontal velocity u against spatial lag ζ. The integral length scale l is defined as the integration over hatched area ($\zeta = 0 \rightarrow \zeta_0$). Turbulence data is produced from experiment using $S = 4$ cm, $f_g = 6$ Hz and $Re_M = 12000$ and at $z/M = 2.5$.

horizontal velocity component is thus computed as

$$l = \int_0^{\zeta_0} g(\zeta)d\zeta, \tag{2.6}$$

where $g(\zeta)$ is the normalised horizontal autocorrelation coefficients and ζ denotes the spatial lag. The integral length scale through spatial autocorrelation (for each vertical position z_j and time step) is then formulated as

$$g(z_j, t_n, \zeta_k) = \frac{\sum\limits_{i=1}^{L-\zeta} \tilde{u}(x_i, z_j, t_n)\tilde{u}(x_{i+\zeta_k}, z_j, t_n)}{\sum\limits_{i=1}^{L} \tilde{u}(x_i, z_j, t_n)^2}, \tag{2.7}$$

where $\zeta_k = 0, 1, 2, 3, ..., L-1$ is the discrete lag.

At each time step we have length scales calculated as the normalised area under the autocorrelation curve, shown in Figure 2.2 as the hatched area,

$$l(z_j, t_n) = \delta_x \sum_{\zeta=0}^{\zeta_0} g(z_j, t_n, \zeta_k), \tag{2.8}$$

where ζ_0 is the first lag where $g(z_j, t_n, \zeta_k) = 0$ (see Figure 2.2). The time averaged integral length scale is then calculated as,

$$l(z_j) = \frac{1}{N} \sum_{n=1}^{N} l(z_j, t_n). \tag{2.9}$$

Consequently, the turbulent Reynolds number $Re_l = ul/\nu$ can be calculated, where data in this study is within the range of $110 < Re_l < 670$.

2.2.2 Determination of averaging time and sampling rate

Cheng and Law (2007), in their oscillating-grid experiments with fluid velocity measured using PIV, reported a minimum averaging time $T = 80$ s to obtain converged statistically invariant r.m.s. velocity components. Lower averaging times resulted velocity statistics that were either overestimated or underestimated. Although this served as a useful basis, a different setup was employed here and so a minimum T needed to be determined. Let $\tilde{u}(t)$ denotes the time series at some fixed point (x_i, z_j). The convergence of the mean velocity $\overline{u}_{conv}$ is calculated as

$$\overline{u}_{conv}(N_t) = \frac{1}{N_t} \sum_{n=1}^{N_t} \tilde{u}(t_n), \tag{2.10}$$

and the convergence of r.m.s. velocities u_{conv} was obtained as

$$u_{conv}(N_t) = \sqrt{\frac{1}{N_t} \sum_{n=1}^{N_t} (\tilde{u} - \overline{u}_{conv})^2}, \tag{2.11}$$

where $n = 1, 2, 3, ..., N_t$ and $0 \le N_t \le N$ is the averaging time interval.
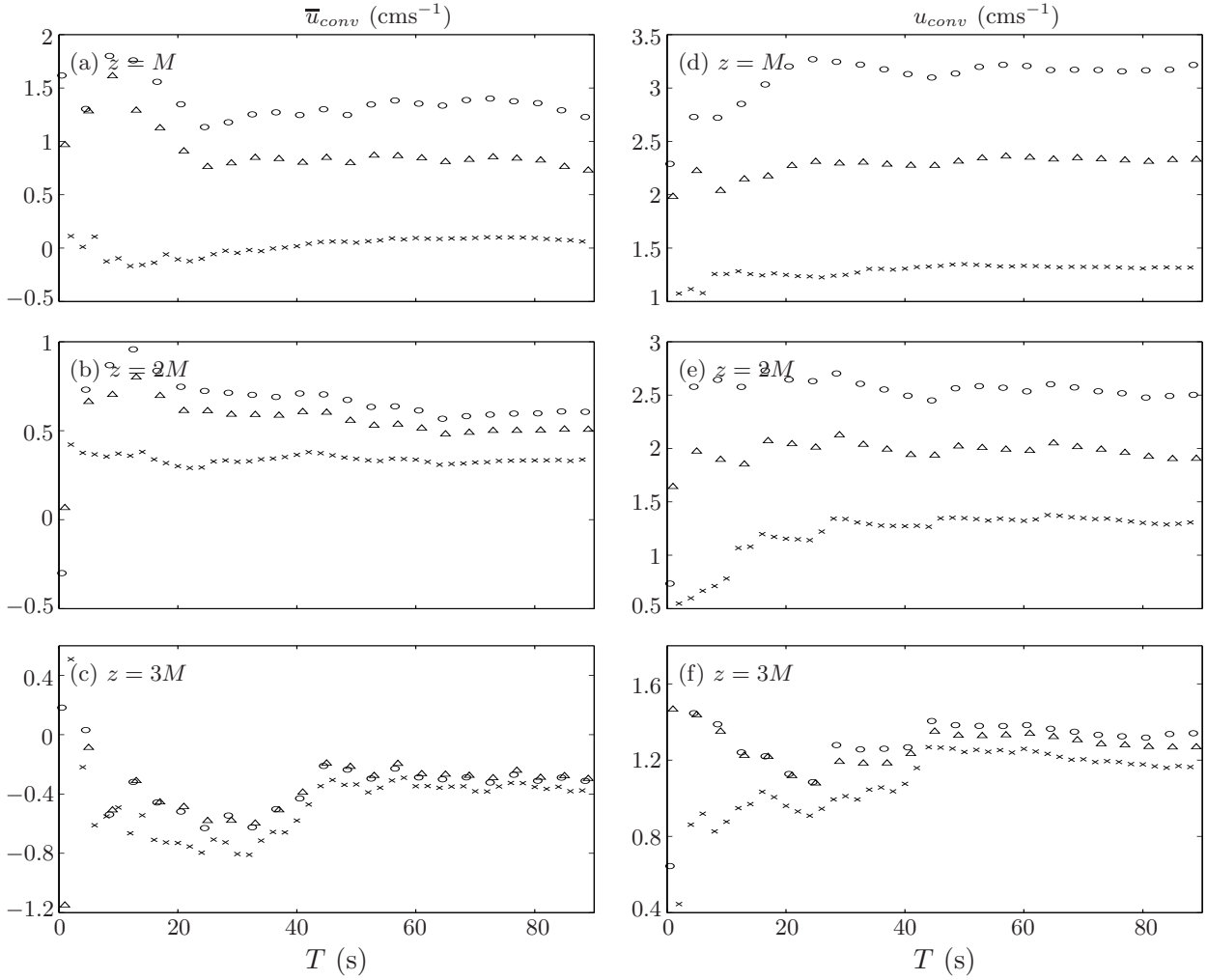
Figure 2.3: Analysis of time averaging T dependence for mean horizontal velocity components $\overline{u}$ (a) - (c) and r.m.s. horizontal velocity u (d) - (f) at distances, $z = M, 2M$ and $3M$ respectively. Also included is the effect of sampling rate where legend represents ∘ (200 Hz), △ (100 Hz) and × (50 Hz).
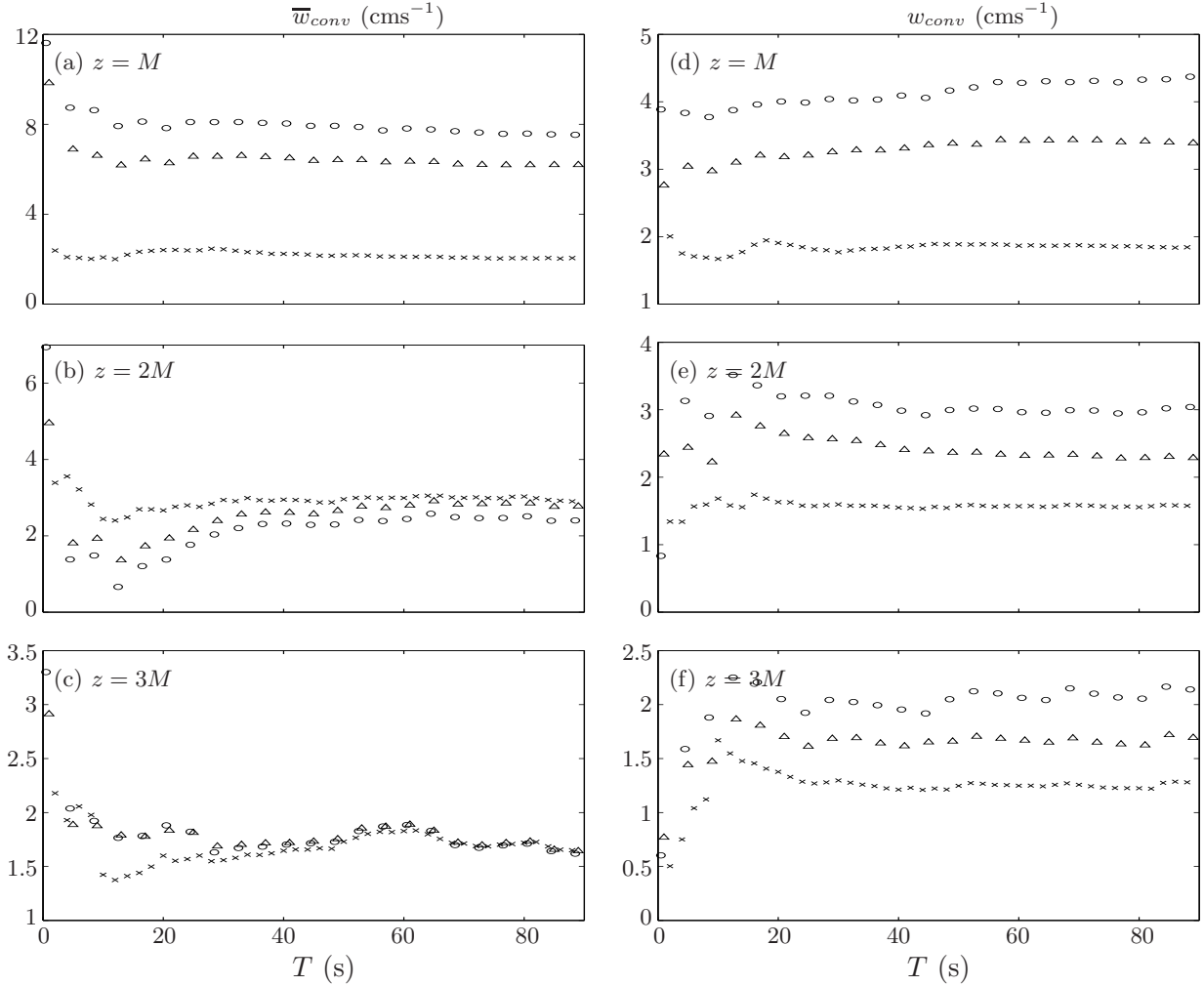
Figure 2.4: Analysis of time averaging T dependence for mean vertical velocity components $\overline{w}$ (a) - (c) and r.m.s. horizontal velocity w (d) - (f) at distances $z = M, 2M$ and $3M$ respectively. Also included is the effect of sampling rate where legend represents ○ (200 Hz), △ (100 Hz) and × (50 Hz).

Figures 2.3 and 2.4 show the time averaging T dependence on the convergence of the horizontal and vertical velocity components, respectively when the time averaging over T is between $0 \leq T \leq 90$ s, which is equivalent to $0 \leq N_t \leq 18000$. Three time series were obtained at a fixed point (x, z) for different heights of $z = M, 2M$ and $3M$ away from the grid, respectively. Velocity components were obtained at a sampling rate of 200 Hz. These heights were chosen to increase progressively from the near grid source to evaluate the effect of inhomogeneity (at grid source) on the convergence of velocity. The plot also illustrates the effect of varying the camera sampling rate at 200, 100 and 50 Hz,

respectively in calculating the mean and r.m.s. velocities. For the sampling rate of 200 Hz, the mean and r.m.s. velocities were obtained using Equations (2.10) and (2.11) using $n = 1, 2, 3, .., N_t$. Corresponding velocities for each sampling rate (i.e. 100 and 50 Hz) were obtained by re-processing the same velocity data in Digiflow and calculated the mean and r.m.s. turbulent velocities at every second and fourth images for 100 Hz ($n = 1, 3, 5, .., N_t$) and 50 Hz ($n = 1, 5, 9, .., N_t$), respectively.

Both figures clearly show that the sampling camera rate is important in measuring the mean and r.m.s. velocities, particularly near the grid ($z = M$). At this distance, lower $\overline{u}, \overline{w}$ and u, w were obtained when they were calculated using sampling rates of 100 Hz and 50 Hz, respectively. High turbulent intensity due to the grid oscillation at this distance requires higher sampling rates to be able to capture (at high accuracy) the movement of tracer particles, so that the measured values are representative of the turbulent flow. Near the grid, values of $\overline{u}$ and u reached a convergence limit at $T \approx 40$ s, where as $T \approx 30$ s were required for convergence for $\overline{w}$ and w components, independent of sampling rate. As the distance z increases further away from the grid at $z = 2M$, the horizontal velocity components values reached convergence at longer time averaging of $T \approx 60$ s and for the vertical velocity components were at $T \approx 45$ s. As the turbulence being propagated away from the grid and reached $z = 3M$, the effect of sampling rate happen to be less significant particularly for the mean velocity ($\overline{u}$ and $\overline{w}$) components and reached a convergence value at $T \approx 45$ s. Note that the values measured using sampling rate of 50 Hz are still lower than those measured at a higher sampling rate (i.e. 100 and 200 Hz). Figures 2.3 and 2.4 indicate that for mean $\overline{u}$ and $\overline{w}$ and r.m.s. velocities u and w, $T = 45$ s is shown to be the vicinity of convergence, independent of sampling rate. Data in Figure 2.3 suggests that the converged mean horizontal velocity $\overline{u} \approx 0$, indicating negligible horizontal mean flow. The u component was seen to steadily decrease with increasing z away from the grid. At distance $z = 3M$, $\overline{u}$ is approximately zero, giving u as the dominant velocity component.

Figure 2.4 shows that the mean vertical velocity $\overline{w} \neq 0$ even at $z = 3M$, which is expected as a consequence of uniaxial forcing of the grid. The $\overline{w}$ value is dependent on stroke S, where smaller S produced $\overline{w} \approx 0$ at $z > 2M$, but as S gets larger, $\overline{w}$ deviates from zero (Yi, 2002). Note that as the data in Figure 2.4 was obtained from the turbulence generated using $S = 8$ cm at high frequency $f_g \approx 5$ Hz, giving high Reynolds number Re_M = 19200 (that is the highest Re_M in this study), a non-zero $\overline{w}$ even further away from the grid was observed, in agreement with Yi (2002). Although $\overline{w} \neq 0$, it was noted that $\overline{w}$ decreases as distance z increases further away from the grid. The r.m.s. vertical velocity w

component was shown to have higher value than u at relatively close proximity to the grid ($z = 1.5M$) and was shown to steadily decrease for $z \geqslant 2M$. It was also noted that as the turbulence decays moving far away from the grid, the w-component is still much higher than u, even at $z = 3M$ (see Figures 2.3(f) and 2.4(f)). Although this shows anisotropy even at distances far away from the grid, the w-component is found to be comparable to u, that is the turbulence can be considered as quasi-isotropic. Note that for the sediment threshold experiments, the frequency of grid oscillation $f_g \leq 3$ Hz giving $Re_M \leq 12000$. Therefore the influence of anisotropy within the quasi-isotropic homogeneous region is much less significant.

The effect of using a shorter mean averaging time for velocity calculation is clearly demonstrated in both Figures 2.3 and 2.4, where the statistical results are neither found to be consistent nor converged for $T \leq 40$ s. Data also implies that if the focus is within the region near the grid, it is more appropriate to use a camera sampling rate of 200 Hz for the measurement of fluid velocities, whereas at further distances from the grid, lower sampling rate (i.e. 100 Hz) is acceptable. For better accuracy, particularly in regions near the grid, the camera sampling rate was fixed at 200 Hz and the mean averaging time T was set at 45 s, corresponding to 12000 images to calculate the velocity components throughout this study.

Results shown in Figures 2.3 and 2.4, where the mean horizontal velocity is close to zero and the decay of r.m.s. u and w as z increases, give a preliminary evidence that the turbulence generated by the experimental procedure is zero-mean quasi-isotropic homogeneous turbulence. The characteristics of generated turbulence is expected to fit the description of grid turbulence in Hopfinger and Toly (1976).

2.3 Results: Characteristics of oscillating-grid turbulence

2.3.1 Mean flow

It is impossible to completely eliminate secondary flow in the OGT system and such flows should be recognised as an intrinsic feature in the oscillating-grid turbulence (McKenna and McGillis, 2004). Even so, care was taken to minimise the secondary flow in the oscillating-grid tank used in this study. Recall that the grid employed had solidity of 0.36, is comprised of square-bars and grid end conditions that ensure the wall behaves as a plane of symmetry. The maximum frequency f_g used in this study was 6 Hz, which is well

below the recommended limit of 7 Hz (McDougall, 1979) and 8 Hz (Shy et al., 1997).
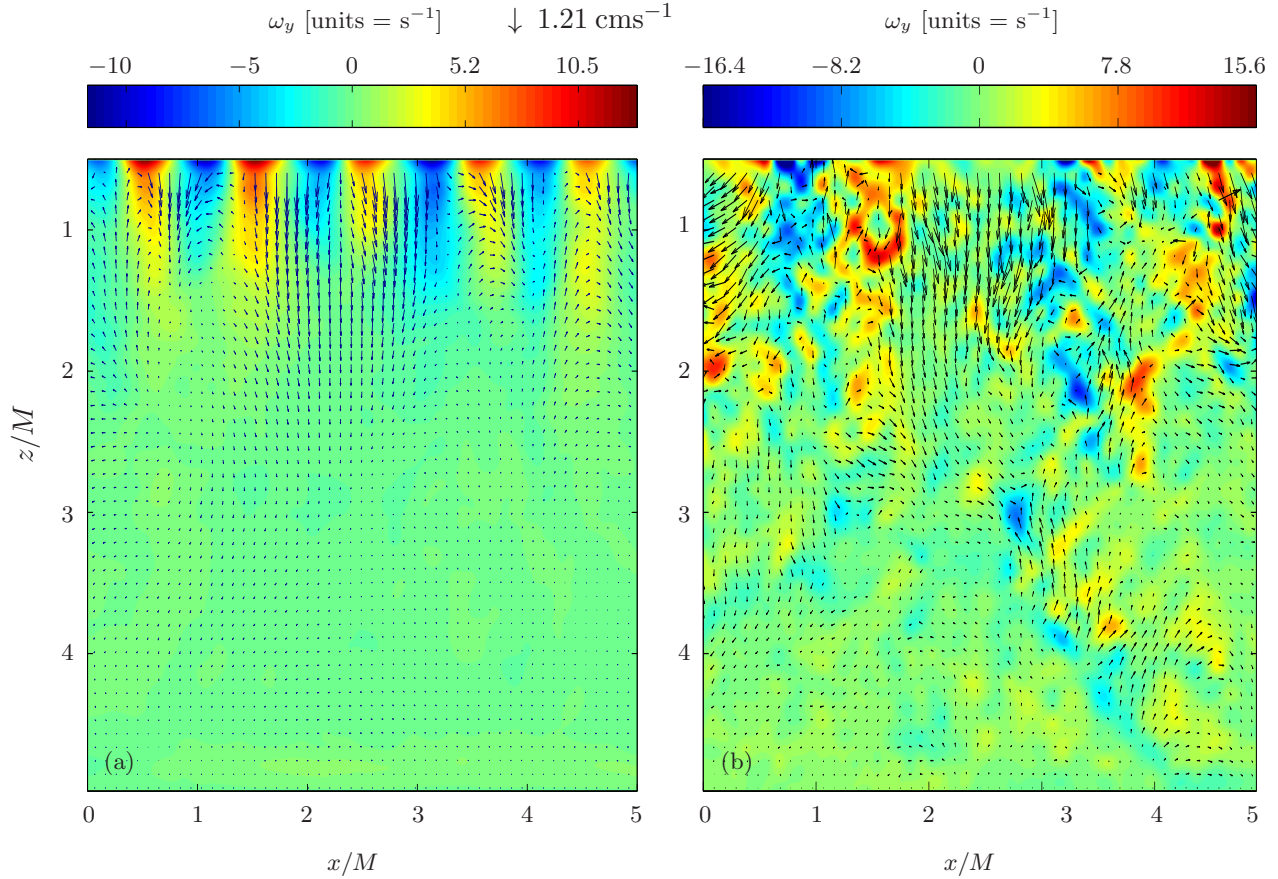
Figure 2.5: Mean velocity fields $\overline{u}(x, z)$ and vorticity visualization $\omega_y(x, z)$ in xz plane, where S=4 cm, f_g=6 Hz, $Re_M = 12000$. The down arrow ($\downarrow$) on the top right marks the maximum mean velocity value and the color bar representing the vorticity strength. Blue contour indicates negative vorticity (anticlockwise) and red-yellow contour indicates positive vorticity (clockwise). Plot in (b) shows an instantaneous velocity and vorticity fields, corresponding to the same experiments.

In an attempt to qualitatively ascertain that the mean flow was weak in the grid tank, the time-averaged mean velocity fields measurements were observed. The PIV results provided whole-field visualizations of the bulk flow structure i.e., where the velocity fields data spanned the complete depth of the tank in the z direction from the bottom of the grid stroke ($z = S/2 + d_g/2$) to the bottom of tank. Recall that z is the distance from virtual origin ($z = 0$) taken at the grid midplane. A complete two-dimensional snapshot of the mean velocity fields with the mean vorticity background is shown in Figure 2.5(a). The vorticity scale ω_y was defined as

$$\omega_y = \frac{\partial \tilde{u}}{\partial z} - \frac{\partial \tilde{w}}{\partial x}. \tag{2.12}$$

Because of the no-slip condition at the surface of the grid elements, each bar generated vorticity due to viscous forces at the edge of the grid, producing alternating negative and positive vorticities. Each coupling of positive-negative vorticity (blue-red contour) near the grid was visible as shown in Figure 2.5. The distance between each vorticity coupling spans $x \approx M$, in agreement with the mesh size. In Figure 2.5 the high vorticity distribution near the grid shows the presence of shear stress due to the wake and the jet produced from the oscillating motion. The interaction of jet and wakes creates a layer of intense turbulent motion near grid. The turbulent layer is thickened via entrainment of irrotational surrounding fluid, giving rise to large scale energetic motions, particularly around $z/M = 1$. The turbulent motions travel up to $z = 2M$, propelled by the strong localised jet structures. The strong vertical direction of jet flow is evident from the grid openings up to $z \approx 2.1M$, although the intensity is highest in the middle of the tank at $x/M = 0$.

At the distance $z \approx 1.5M$ from the grid, the intense interaction between jets and wakes breakdown into turbulence and no mean vorticity was observed. In an instantaneous fluid velocity fields as shown in Figure 2.5(b), vorticities and fluid motions were visible throughout the depth of the tank, even at $z = 4M$. However, time averaging canceled the randomly orientated vorticities and the residual angular momentum per unit volume tended to a zero value across the horizontal plane (see Figure 2.5(a)), particularly at $z > 2M$. Therefore, at distance $z/M > 2$, with insignificant shear stress and negligible large scale motions in the bulk flow it is apparent that no secondary flow and a quasi-isotropic homogenous turbulence exists.

The statistically stationary grid-generated turbulence within the quasi-isotropic homogeneous region is 'self-similar', in that the net energy coming from the energy-containing eddies is in equilibrium with the net energy cascading to smaller eddies where it is dissipated. This is similar to the inertial subrange, where in this region, the statistical properties of turbulence are only determined by the rate of dissipation of turbulent kinetic energy. Kolmogorov (1941) showed that the energy spectrum (i.e. the distribution of turbulent kinetic energy among the eddies of different size) within the inertial subrange has the relationship of $\phi(f) \sim \omega^{-5/3}$. By performing an energy spectrum, the existence of a quasi-isotropic homogeneous turbulence can be detected by assessing the slope (of energy

spectrum) in the inertial subrange, that is should be approximately -5/3. This has been employed by previous studies of Silva and Fernando (1994); Stiansen and Sundby (2001); Campagne et al. (2006).

Tennekes (1975), in his theoretical analysis of isotropic 'box' turbulence in the absence of mean flow, suggested that the Eulerian frequency spectrum is predominantly influenced by the angular frequency of $\omega = u\kappa$, where κ is wave number. The value of wave number can be calculated as $\kappa = 2\pi/\lambda$, where λ is the wavelength of a (velocity) signal. Wave number in the energy spectrum represents the lengthscale of eddies available in the flow. Since eddies of wave number κ in the inertial subrange have kinetic energy per unit mass of $(\epsilon\kappa^{-1})^{2/3}$, the resulting frequency spectra for the inertial subrange becomes $\phi(\omega) \sim (\epsilon\kappa^{-1})^{2/3}/\omega$, or can be written in the form

$$\phi(\omega) = C_1 \epsilon^{2/3} u^{2/3} \omega^{-5/3}, \tag{2.13}$$

where $\phi(\omega)$ is the spectral density at angular frequency ω and C_1 is a non-dimensional universal constant assumed to be $\mathcal{O}(1)$ and ϵ is the rate of dissipation of turbulent kinetic energy. Expressed in terms of the natural frequency, $f = \omega/2\pi$,

$$\phi(f) = C_2 \epsilon^{2/3} u^{2/3} f^{-5/3}, \tag{2.14}$$

where $\phi(f)$ is the energy spectral density at natural frequency and $C_2 = C_1(2\pi)^{-2/3}$. The $\phi(f)$ describes how the energy of a velocity time series is distributed with frequency.

Let $f(t_n)$ be an input signal (a sequence) of either horizontal or vertical velocity time series and let $\mathcal{X}(k)$ be a frequency spectrum, the result of the discrete Fourier transformation of a signal $f(t_n)$ as,

$$\mathcal{X}(k) = \sum_{n=0}^{N-1} f(t_n) e^{-\frac{2\pi i}{N} nk}, \tag{2.15}$$

where $n = 0, 1, ..., N-1$, i is imaginary unit and $e^{-\frac{2\pi i}{N}}$ is a primitive N^{th} root of unity.

By performing a fast fourier transform to compute the relations in Equation (2.15), the energy spectral density is calculated as

$$\phi(f) = \frac{\mathcal{X}(k)\mathcal{X}^*(k)}{2\pi}, \tag{2.16}$$

where $\mathcal{X}(k)$ and $\mathcal{X}^*(k)$ are the real and imaginary components respectively. Note that

horizontal and vertical energy spectrum which are denote as $\phi_u(f)$ and $\phi_w(f)$, respectively are obtained using Equations (2.15) and (2.16) using time series of horizontal and vertical fluid velocity, respectively.
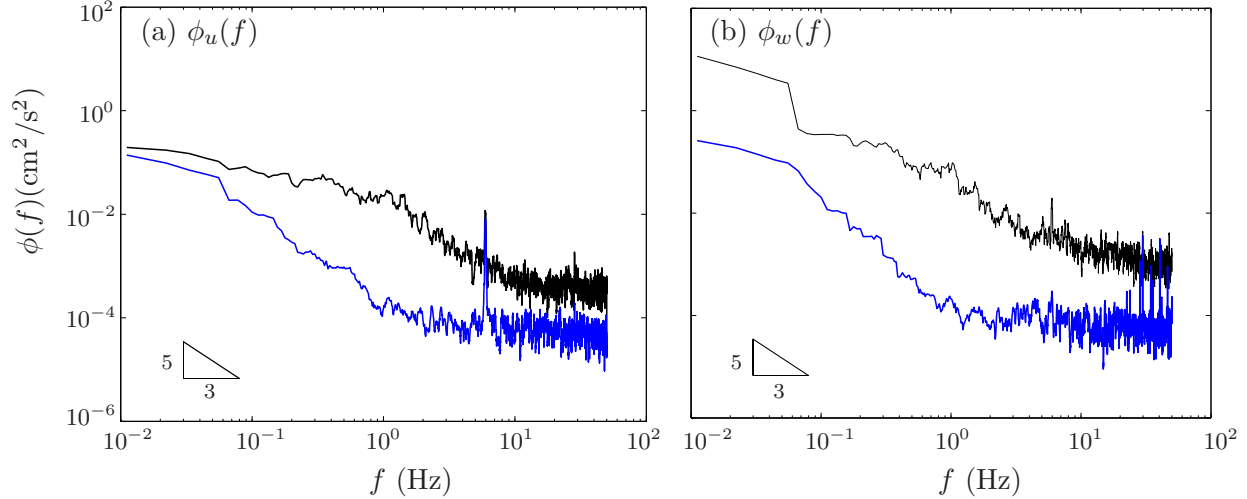
Figure 2.6: Spectrum of (a) horizontal and (b) vertical energy distributions, ϕ_u and ϕ_w, respectively, at distances of M (black solid line) and $3.5M$ (blue solid line) away from the grid. The data is generated using $S = 4$ cm, $f_g = 6$ Hz. The triangle-solid shows the slope $f^{-5/3}$.

Figure 2.6 shows a one dimensional energy spectrum of both horizontal and vertical velocity components, $\phi_u(f)$ and $\phi_w(f)$, respectively. The velocity time series were obtained at a fixed point (at the centre of the tank), with varying distances at $z = M$ and $z = 3.5M$. As the Reynolds number Re_M here ($2000 < Re_M < 20000$) is relatively small compared to the Reynolds number in naturally occurring turbulent flow, the $f^{-5/3}$ slope (showing inertial subrange) is not guaranteed. Restricting the Reynolds number restricts the frequency range, that is the range may not be wide enough to exhibit an inertial subrange. However, the data in Figure 2.6 suggests that the inertial subrange exists at $z = 3.5M$ within the frequency range of $0.078 \leq f \leq 1$ for the horizontal component and at frequency range of $0.4 \leq f \leq 1.5$ for the vertical component. Both the horizontal and vertical frequency spectra show a distinct peak at 6 Hz corresponding to the forcing frequency of the oscillating grid f_g, particularly near the grid ($z = M$). Note that for this particular set of data, $f_g = 6$ Hz. Figure 2.6(a) shows a higher peak (at 6 Hz) at $z = 3.5M$ than at $z = M$. The high turbulence intensity at near grid, where (large scale) eddies are interacting with each other, the eddies carrying information of f_g is less, hence

the shorter peak at $z = m$. Whereas, when the turbulence breaks down and propagates further away, the dominant forcing frequency is found to be more evident. As the setup employed here is an oscillating-grid tank, it is expected that even the turbulence in the homogeneous region shows a distinct f_g signal in its energy spectrum. This is because when the measurement of fluid velocity was taken (for each distance), the grid is still oscillating. Figure 2.6(b), however shows that at $z = 3.5M$, the peak at 6 Hz is indefinite. It is believed the information associated with the forcing frequency is lost in the process of turbulence breakdown and decay.

2.3.2   Onset quasi-isotropic homogeneous turbulence
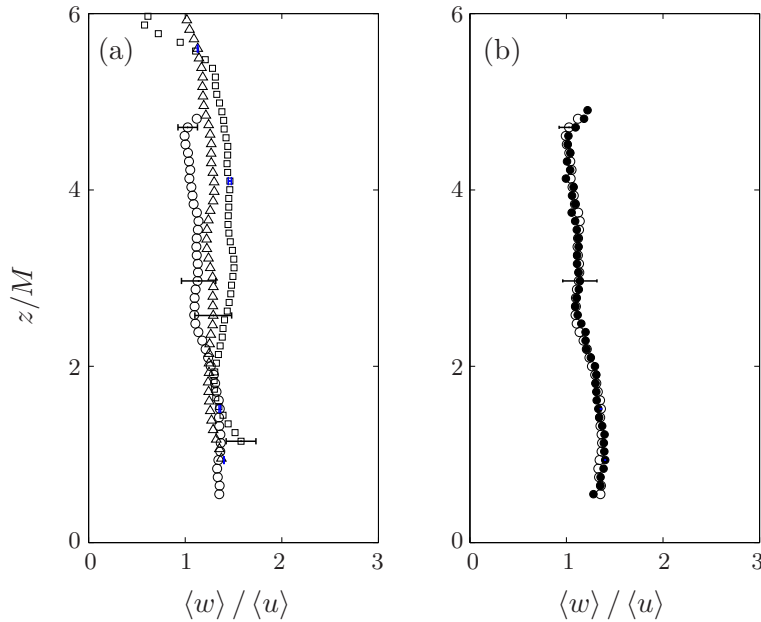
Figure 2.7: Evolution of degree of isotropy, represented by $\langle w \rangle / \langle u \rangle$ as a function of (a) stroke (b) frequency with distance z/M. The plots correspondence to $S= 4$ cm, f_g=1.5 Hz ($\circ$), S=8 cm, f_g=4.8 Hz ($\triangle$) and S=10 cm, f_g=1.7 Hz ($\square$). On (b) $S= 4$ cm, f_g=1.5 Hz ($\circ$) and S=4 cm, f_g=6 Hz ($\bullet$). Blue and black line denote the minimum and maximum error bar, respectively, for each data set.

Although previous analysis (in Figure 2.5) showed that the quasi-isotropic homogeneous turbulence region was found from $z > 2M$, the determination of the onset of quasi-isotropic homogeneous turbulence region was done by plotting isotropy w/u, the ratio of the r.m.s. vertical and horizontal turbulent velocities. It is important to investigate the onset of the homogeneous region to ensure the validity of Equation (1.10). By plotting

isotropy w/u against distance z, a more accurate idea of where the homogeneous region begins will be determined. Figure 2.7(a) shows the evolution of degree of isotropy w/u (plotted here as $\langle w \rangle / \langle u \rangle$), as a function of distance from the grid for $S/M = 0.8$, 1.6 and 2 with the Re_M varying between 3000 to 19000. Recall that the symbols $\langle w \rangle$ and $\langle u \rangle$ represent the spatially-averaged mean r.m.s. vertical and horizontal velocity, respectively. The component w is shown to have a larger value than u along the distance z, particularly at close proximity to the grid. Although $\langle w \rangle / \langle u \rangle$ was not exactly the ideal at 1 value, isotropy was achieved and remained constant beyond $z = 2.5M$ (at least within experimental error). The data shows an increase in isotropy with larger stroke, with corresponding $\langle w \rangle / \langle u \rangle$ values of 1.1, 1.3, 1.5 for $S/M = 0.8, 1.6, 2$, respectively. For the strokes used in this study, the $\langle w \rangle / \langle u \rangle$ ratio was found to be fairly constant around $1.1 \sim 1.5$ in the homogenous region, in agreement with previous research of Cheng and Law (2007); McKenna and McGillis (2004). Figure 2.7(a) shows that for each stroke, the $\langle w \rangle / \langle u \rangle$ profiles are all attained at a relatively comparable distance $z \approx 2.5M$. This indicates that the homogeneous region can be found at $z = 2.5M$, regardless of stroke used. In assessing the dependency of frequency f_g on the $\langle w \rangle / \langle u \rangle$ ratio, Figure 2.7(b) illustrates the isotropy of a 4 cm fixed stroke with two frequencies set at a minimum of 1.5 Hz and maximum of 6 Hz. The results show that the $\langle w \rangle / \langle u \rangle$ ratio becomes constant value around 1.1 at approximately the same distance $z = 2.5M$ as initially determined. The onset of homogeneity is therefore considered independent of f_g, in agreement with the findings of Cheng and Law (2007).

2.3.3   Integral length scale

In order to derive Equation (1.10), it is necessary that the integral length scale of the turbulence is linearly dependent on z within the homogeneous region. The longitudinal integral length scale l was obtained from the normalised autocorrelation of the velocity signal using Equation (2.6). Although this definition is somewhat arbitrary, it provides a measure of the extent of the region where the velocities are appreciably autocorrelated (Davidson, 2007). According to literature, the integral length scale l should increase as z increases. As an example, Figure 2.8 shows the normalised correlation coefficients $g(\zeta)$ obtained from r.m.s. horizontal velocity u plotted against spatial lag ζ; the data shown is taken from different heights $z/M = 2.5, 2.8$. As z moves further away from the grid, the spatial lag $\zeta = \zeta_0$ increases, indicating an increase of the integral length scale. Recall that
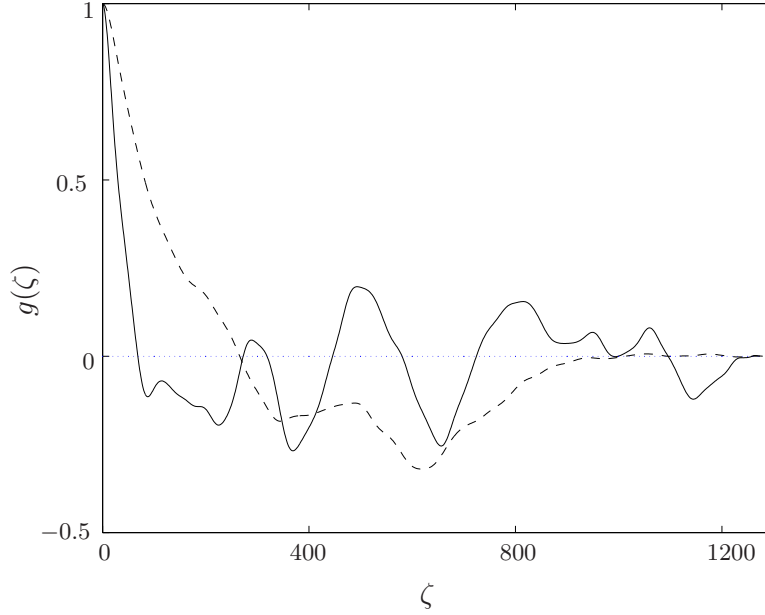
Figure 2.8: An example of normalised autocorrelation function $g(\zeta)$ of r.m.s. horizontal velocity u against spatial lag ζ at $z/M = 2.5$ and 2.8 corresponding to solid and dotted lines respectively. Turbulence data is produced from an experiment using $S = 4$ cm, $f_g = 6$ Hz and $Re_M = 12000$.

ζ_0 is the first point when $g(\zeta) = 0$.

S/M	0.8	1.6	2
β_l	0.097	0.112	0.134

Table 2.2: Summary of coefficients β_l obtained using r.m.s. horizontal velocity.

The computed integral length scale l for each stroke $S/M = 0.8, 1.6, 2$ are plotted as a function of z, shown here in Figure 2.9 as dimensionless variables l/S against z/M. Using a least square fit line, a linear $l = \beta_l z$ relationship was obtained and values of β_l for each stroke were computed. The empirical coefficients β_l for each stroke used are shown in Table 2.2. Although β_l is increasing with S/M, all values are well within the range of $0.1 \sim 0.3$ as reported in past oscillating-grid turbulence characteristics studies (Hopfinger and Toly, 1976; Hopfinger and Linden, 1982). As $S/M \geq 0.8$ was used here, the scale is proportional only to M (Hopfinger and Toly, 1976). However, the coefficient β_l was found to increase as S increases, in agreement with (Hopfinger and Linden, 1982). For a
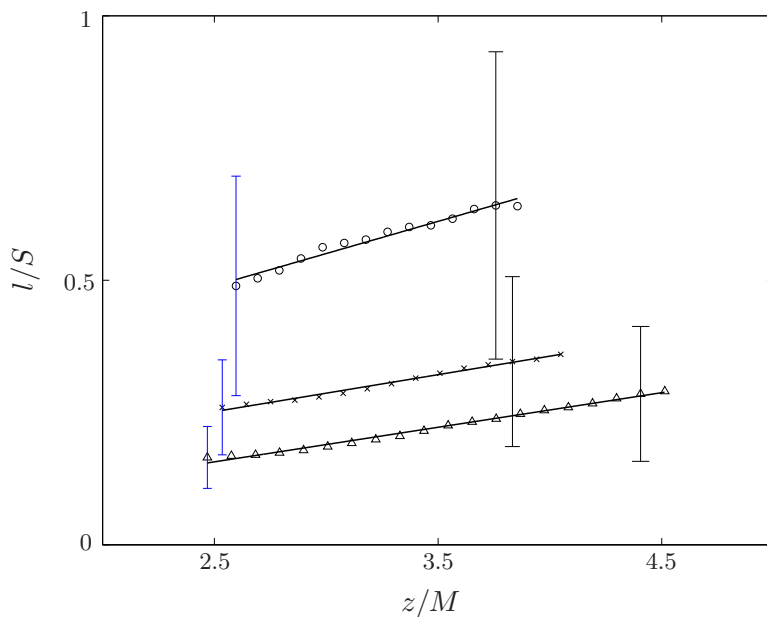
Figure 2.9: Dimensionless integral length scales l/S plotted linearly against dimensionless distance z/M, where data are represented with turbulence generated using $S = 4$ cm, f_g = 6 Hz ($\triangle$), $S = 8$ cm, $f_g = 4.8$ Hz ($\times$) and $S = 10$ cm, $f_g = 4$ Hz ($\circ$). Blue and black lines denote minimum and maximum error respectively.

given mesh size M described in the experiments (i.e. fixed at 5 cm), the coefficient β_l for the range of stroke used here (i.e. $S = 4,8$ and 10 cm) is taken as the averaged β_l values 0.11 ± 0.02, within the range reported by Thompson and Turner (1974). In all cases, the scale is linearly proportional to z, validating Equation (1.9). The estimation of maximum and minimum error associated with the measured values of l are also shown in Figure 2.9. The variation of error shown is somewhat pessimistic and is believed due to the arbitrary calculation of the integral length scale itself. The minimum error associated with the l measurements for strokes discussed here occurs within the specified homogeneous region closer to the grid, whereas maximum error occurs at larger z. As the turbulence decays, the smallest eddies decay the fastest due to their small turn over time compared to that of larger scale eddies. Thus, it can be surmised that the turbulence further away from the grid is dominated by large, slowly rotating eddies. The spatial horizontal velocity is then less when correlated at larger distance z, giving higher error.

2.3.4   The spatial decay of quasi-isotropic homogeneous turbulence

The isotropy plots show that the quasi-isotropic homogeneous region starts approximately $2.5M$ away from the grid. Recall that Equation (1.10) is only applicable within the homogeneous region. Inhomogeneity of the turbulence near the grid, if included in the region to calculate the empirical coefficients, will have a significant impact on their determination and the values may vary by up to 20% (Mohamed and LaRue, 1990). Using Equation (1.10) and Equations (2.5), the spatially averaged turbulent intensity with distance from the virtual origin is presented according to

$$\frac{\langle u \rangle}{f_g S} = C_u \left\{ \frac{z}{(SM)^{1/2}} \right\}^{-n_u} \tag{2.17a}$$

$$\frac{\langle w \rangle}{f_g S} = C_w \left\{ \frac{z}{(SM)^{1/2}} \right\}^{-n_w} \tag{2.17b}$$

The powers n_u, n_w and constants C_u, C_w were obtained by empirically from the data shown in Figure 2.10. A least square fit was applied from $z = 2.5M$, as suggested by the isotropy analysis, to $z = 4M$. The limit taken at $z = 4M$ is to eliminate the inhomogeneity effects occurring due to the presence of the tank base at $z \approx 5M$. Secondary circulations were observed when the turbulence interacted with the tank base, resulting in local inhomogeneity and anisotropy (Hannoun et al., 1988; Campagne et al., 2008). Also, further

away from grid, the turbulence may reach the final decay state, where the turbulence does not necessarily decay according to $u \propto z^{-1}$ (Silva and Fernando, 1994).
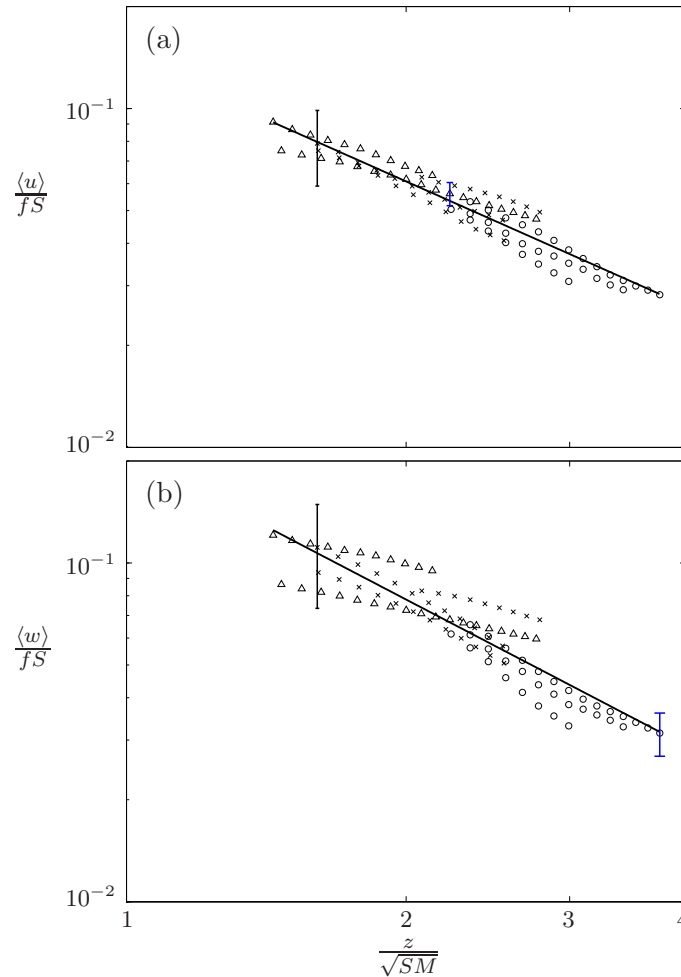
Figure 2.10: Measurements of (a) mean horizontal r.m.s. velocities and (b) mean vertical r.m.s. velocities within the quasi-isotropic homogeneous turbulence region. Data were generated using strokes of $S = 4$ cm ($\circ$), $S = 8$ cm ($\triangle$) and $S = 10$ cm ($\square$). The straight line shows the least square fit to all of the data. The blue line indicates the minimum error whilst the black line denotes the maximum error within the considered homogeneous region.

The assumption of quasi-isotropic turbulence $u \approx v \approx w$ suggests that the $n_w = n_u$. Instances in literature where the vertical velocity empirical constants have been examined are scarce. In the literature, (to the best of the author's knowledge) only two studies Silva

and Fernando (1992) and Yi (2002) examined n_w and C_w. Silva and Fernando (1992), using stroke $S/M < 0.8$, found that $n_w = 1$. Yi (2002) on the other hand used multiple strokes in his experiments (i.e. $S/M < 0.9$) and discovered that the power law n_w values are dependent on stroke with n_w decreasing with larger S. Such limited investigations focusing on n_w and mixed results encouraged further analysis to assess the vertical power decay law n_w. This was achieved by plotting the data according to Equation (2.17b).

Figure 2.10 shows the turbulence decay profile for both horizontal and vertical velocity components and the data for all strokes were included. A linear regression fit was applied for each profile . The fit is considered to be a good representation of the data and this is confirmed by the correlation coefficients of $r^2 = 0.91, 0.84$ for $\langle u \rangle$-components and $\langle w \rangle$-components, respectively. Furthermore, the measured values of $C_u = 0.14$ and $C_w = 0.21$ compare favourably with those of Hopfinger and Toly (1976) who found $C_u \approx 0.25$ and $C_w \approx 0.27$, respectively.

The measurements of the decay exponent $n_u = 1.22$ is comparable to $n_u = 1$ found by Hopfinger and Toly (1976). The vertical component decays much faster with $n_w = 1.44$ as the energy is used to transport the kinetic energy. The empirical constants measured in this study are compared with those reported in other related studies (shown in Table 2.3). The variation of C_u and C_w is expected as the oscillating-grid setup is different for each study. However, what more important is that both n_u and n_w are of similar order of magnitude and are comparable.

Although the values of n_w obtained are comparable to 1, the plot in Figure 2.10(b) suggests that an individual fit for each stroke is more appropriate. The empirical constants of n_u, n_w, C_u and C_w for each stroke were thus obtained using Equation (2.17) and are summarised in Table 2.4. The power constants n_u and n_w were between 0.92 and 1.43 and are within the range of those reported in other oscillating-grid turbulence studies (Thompson and Turner, 1974; Hopfinger and Toly, 1976). The data shows the dependency of n_u on S/M, with decreasing n_u for larger strokes in agreement with the findings reported by Nokes (1988) and Yi (2002). A similar decreasing trend of n_w with increasing S/M was also noticed. Larger strokes produced higher turbulent intensity consisting of high turbulent kinetic energy at large scales, which gave rise to a less rapid decay of energy. Within the homogeneous region, Table 2.2 shows that coefficient β_l increases with S, indicating that the integral length scale l (calculated using the $l = \beta_l z$ relationship) also increases for larger strokes. This also has been reported by Hopfinger and Linden (1982). Thus, the dissipation rate of the turbulent kinetic energy is dependent on stroke, whereby

Source	S/M	n_u	C_u	n_w	C_w	HR	Measurement technique	Method of HR determination
Hopfinger, 1976	0.8	1	0.25	-	-	$2M$	hot-film anemometer	isotropy $w/u \sim 1$
DeSilva, 1992	0.18 & 0.44	1	0.22	1	0.27	$4S$	LDV	fitting z^{-1} slope
Cheng, 2001	0.8	1	≈ 0.25	-	-	$3M$	DPIV	coincidence of u and w-components
Present study	0.8,1.6,2	1.22	0.14	1.44	0.21	$2.5M$	PIV	isotropy w/u reaches constant value

Table 2.3: Comparison of coefficients C_u, C_w and decay law exponents n_u, n_w with selected oscillating-grid turbulence researches. HR abbreviates for homogeneous region and represents the onset of quasi-isotropic homogeneous region.

S/M	n_u	n_w	C_u	C_w
0.8	1.23	1.43	0.137	0.194
1.6	0.94	0.98	0.116	0.158
2.0	0.92	0.93	0.120	0.155

Table 2.4: Summary of coefficients C_u, C_w and the decay law exponents n_u, n_w.

the dissipation is lower for larger stroke as the length scale l is larger. This is because the life span of an eddy (turn over time $= l/u$) within the quasi-isotropic homogeneous region is longer. The slower decay of turbulence generated with larger strokes can also be attributed to the weak secondary flows inherent in the tank (McKenna and McGillis, 2004). The mean velocity advection $U_j \frac{\partial}{\partial x_j}$ term (in Equation (1.3)) could be significantly nonzero and the mean flow could rapidly advect the turbulence away from the grid, changing the turbulence structure within the bulk flow. For the smallest stroke discussed i.e. $S= 4$ cm, there is a distinguished deviation between n_u and n_w (around $\sim 13\%$), with w component decaying faster with z. The r.m.s. vertical velocity decaying faster than u is expected due to the smaller vertical length scale, breaking up large scale eddies to smaller scales quicker. However, with increasingly large strokes i.e. increasing the turbulent Reynolds number Re_l, the differences between the constants n_u and n_w diminish, and they both approach unity.

We now look into the reliability of the measurements obtained in the selected previous studies. Table 2.3 shows the comparison of approaches in analysis with the previous studies of Hopfinger and Toly (1976), Silva and Fernando (1992) and Cheng and Law (2007). Note that these selected studies all investigated the basic quasi-isotropic homogeneous turbulence statistics using stroke $S \leq 0.8$, where as larger strokes $S \geq 0.8$ were employed in this study. Note that the established and widely used Equation (1.10) (in oscillating-grid turbulence studies) were derived by Hopfinger and Toly (1976) who measured the fluid velocity (at one point) using a hot-film anemometer. The turbulence spatial variation was obtained by rotating the probe on a rotating spindle. The probe is intrusive and affects the bulk flow, where the wake from the probe rotation becomes significant when the turbulent velocity is small, i.e. at low oscillation frequency f_g and at distances further away from the grid. The error associated with the fluid measurement were found to be $\pm 5\%$ to 10% (Hopfinger and Toly, 1976). Although the measurements obtained were probably less accurate than non-intrusive technique, their study however offered initial evidence on spatial turbulence homogeneity in an oscillating-grid tank.

Silva and Fernando (1992) used a non-intrusive method of Laser Doppler Velocimeter (LDV) and measured both the r.m.s. horizontal and vertical velocity components. The fluid measurements were taken at a sampling rate of 50 Hz and the turbulence statistics were obtained over a mean averaging time of $T = 100$ s. Although this technique provides highly accurate measurements, the fluid velocity was only obtained at one (fixed) point, thus direct evaluation of the spatial correlation of the turbulence (i.e. the calculation of integral length scale and homogeneity) was not available. Acknowledging this, Cheng and Law (2007) employed the PIV technique to investigate the characteristics of turbulence induced by an oscillating-grid. Their fluid velocity measurements however, were obtained at low camera sampling rate of 5 Hz (although a longer mean averaging time T was utilised than in the present study). Figures 2.3 and 2.4 show that a low sampling rate results in the underestimation of the turbulence values. It should be noted that although the magnitude of the turbulence values are affected, the turbulence decay exhibits a similar profile.

Thus, this study presents characteristics of turbulence generated by oscillating-grid in a more robust and rigorous manner than previous studies, by addressing the spatial homogeneity and obtaining the fluid velocity measurements at higher sampling rate.

2.4 Conclusions

This chapter analysed the oscillating-grid generated turbulence characteristics as a function of distance from the grid. The turbulence produced was quasi-isotropic and quasi-homogeneous with negligible mean shear flow and secondary circulations. The homogeneous region was found to start at $z \approx 2.5M$, independent of stroke and frequency of oscillation. Although the resulting data shows a decrease in the empirical decay law n_u, n_w when S/M increased, the value of n_u obtained was approximately 1, and in agreement with Hopfinger and Toly (1976). The n_u, n_w and coefficients C_u, C_w measured are comparable [within magnitude of $\mathcal{O}(1)$] with other previous OGT studies of Hopfinger and Toly (1976) Silva and Fernando (1992) and Cheng and Law (2007). This confirmed the findings that turbulent intensity decreases with z^{-1} and has a linearly increasing integral length scale with distance z.

Chapter 3

Critical criteria for incipient sediment motion

This chapter focusses on the critical conditions required to induce particle movement. The characteristics of the turbulence in the near-bed region will first be discussed. This will highlight the nature of the changes to turbulence structure and the occurrence of inhomogeneity due to the presence of a sediment bed.

The critical conditions for the threshold of sediment motion are characterised by the critical dimensionless Shields parameter θ_c, defined in terms of the r.m.s. horizontal velocity u, near to the bed. The critical θ_c variation is investigated as function of sediment characteristics (i.e. density and size) and bed slope (between $0°$ and the repose limit).

3.1 Experiment arrangement

The oscillating-grid apparatus is set up as described in the previous chapter, except that the grid is positioned closer to the tank base. A schematic representation of the tank setup for the sediment experiments is shown in Figure 3.1. The grid was positioned at a consistent distance $z = 3.2M$ (16 cm) and $3.6M$ (18 cm) from the virtual origin to the sediment bed. These distances were chosen to ensure that the quasi-isotropic homogeneous turbulence region was still observed, and so that the turbulence intensity was sufficiently high to displace the sediments. The primary objective of the experiments was to investigate the critical conditions required for incipient sediment motion, i.e. where the incoming homogeneous turbulence interacting with the sediment is just sufficient to
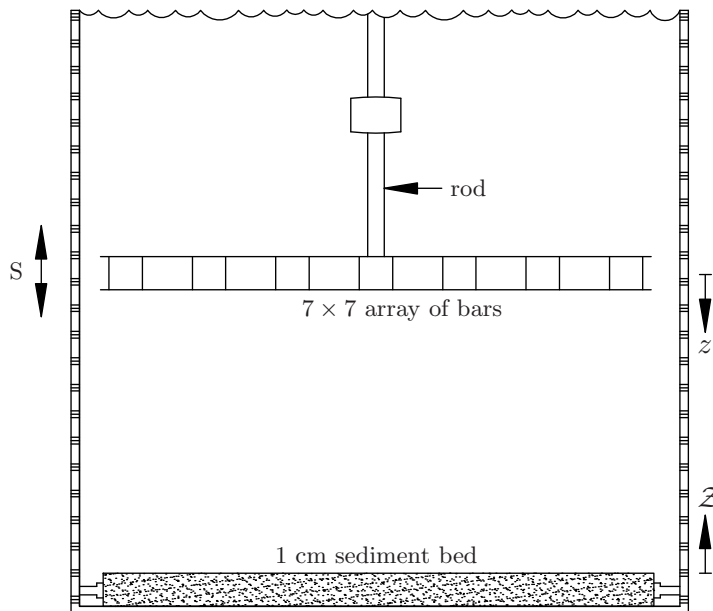
Figure 3.1: Sketch of the grid setup and the fixed rod position for sediment entrainment experiments. A sediment bed is placed at the bottom of the tank. The symbol $\mathcal{Z}$ denotes the distance from sediment bed, where $\mathcal{Z} = 0$ is the sediment bed.

initiate movement of the near-surface grains. For consistency, a stroke S of 8 cm was used throughout. Similarly, the other grid geometric parameters (i.e. M and d_g) remained fixed.

Label	Material	d_{50} (μm)	s	w_s(cm/s)	Re_p	$\varphi(°)$
A	Glass	1101.5	2.5	14.80	163.0	27.5
B	Glass	716.1		8.95	64.1	28.2
C	Glass	562.6		6.90	38.8	28.8
D	Glass	373.9		8.95	18.9	28.1
E	Glass	220.3		8.95	6.7	30.4
F	Glass	153.3		6.90	3.3	29.1
G	Glass	80.0		0.85	0.7	29.0
H	Diakon	751.1	1.18	2.78	20.9	30.8
I	Diakon	273.8		0.97	2.7	33.1
J	Diakon	157.4		0.41	0.7	32.2
K	Diakon	118.7		0.36	0.5	28.9

Table 3.1: The physical characteristics of sediment used.

Two different monodisperse sediment types were used, namely glass ballotini and diakon, with relative density $s = \frac{\rho_s}{\rho} = 2.5$ and 1.18, respectively, where ρ_s and ρ are sediment and fluid densities, respectively. The grain diameters d ranged between 80 and 1087 μm with a narrow size distribution about the mean diameter. The basic properties of the particles used are summarised in Table 3.1, where d, s, w_s and φ denote the particle diameter, relative density, the terminal settling velocity of a single particle and the angle of repose (in water), respectively. The values of w_s were measured in the laboratory and were repeated at least 10 times for each sediment type. Typical variability observed was between $5-10\%$. Also shown in Table 3.1 are the values of the particle Reynolds number $Re_p = w_s d/\nu$. The sediment used was nearly spherical and also homogeneously distributed but this will be discussed in a latter section.

Each sediment layer was formed in 1 cm deep square tray (of width 33 cm) placed at the base of the tank. The tray is fixed to the tank sidewalls by screws at each of the tray corners to ensure that the tray remained fixed throughout. Prior to tilting the tank to the desired angle, the sediment layer was formed by carefully drawing a flat scraper across the top rim of the tray. The small volume of excess particles removed during the scraping process were pushed against the tankwall side, and away from the region of interest. This method produced a flat, close-packed bed of consistent mean depth 1 cm, although, inevitably the bed was not completely flat. It is believed that the small amplitude and long wavelength of the initial bedform irregularities did not adversely affect the dynamics of the interaction. A bed thickness of 1 cm ensured that complete erosion of the particle layer did not occur and that the solid tank base played no role during the interaction. Once the bed was formed, the tank was then inclined to the desired angle and the bed slope was measured with a digital protractor with an accuracy of $\pm 0.1°$. To prevent the sediment bed from sliding on the smooth tray surface when tilted, the tray base was roughened by gluing a thin layer of Particle C to its surface. The effects caused by changes in bed slope were analysed by tilting the sediment layer, the tank and oscillating-grid mechanism at various angles α (see Figure 2.1). The corresponding bed slope is henceforth defined as $\beta = \tan \alpha$. For each sediment type, experiments were performed at bed angles in the range $\alpha \in [0, \varphi)$. Each of the repose angle values was determined (in quiescent water) by slowly increasing the bed angle from $\alpha = 0°$ until the bedform started to become unstable and collapse down the tray. The corresponding measured values of φ are shown in Table 3.1 and are averages taken from several repeats (by re-scraping the horizontal bed for each repeat). In all cases, $\varphi \in [27°, 33°]$ with typical variability of $\pm 1°$.

Since experiments could not be performed at $\alpha = \varphi$, the maximum value of α used was $25°$.

To allow the critical conditions for sediment movement to be determined accurately, the properties of the grid-generated turbulence had to be varied in a systematic and repeatable manner. Hence, for each experiment, the oscillation frequency f_g was gradually increased from 0.5 Hz with ≈ 0.25 Hz increments until the incipient particle movement was observed through visualization. For each frequency increment, the turbulent flow was allowed to develop for approximately 1 minute before being further increased, thereby allowing the turbulence to reach a new steady state. It is important to note that the criteria for incipient motion was taken from one of the (widely used) criteria set by Kramer (1935), that is when several of particles are in motion, in isolated spots, and in countable numbers. The critical frequency f_{gc} was recorded when intermittent sediment movements were observed at each quadrant of the bed for duration of 10 seconds. In order to minimise the error, each of the experiments were repeated and the incipient conditions recorded at least five times for each sediment type and bed slope. During the procedure, the sediment layer was re-scraped and flattened prior to repeating each test. The readings of f_{gc} for the smaller type of particle types were found to be more consistent than the larger particles, but in all cases the variability of f_{gc} was within $\pm 5\%$.

Once the critical conditions had been identified for a given sediment type, time-resolved measurements of the grid-turbulence (interacting with the bed) were then obtained using two-dimensional planar PIV. The fluid velocity measurements were sampled at 200 Hz using a high speed camera for a period of $T = 90$ s. The velocity fields were calculated directly from the captured images using the PIV algorithm in Digiflow (Dalziel) (as discussed in Section 2.1). In each experiment, the PIV images captured the region between the bottom of the grid ($z = S/2 + d_g/2$) to the sediment bed, with width between 15 to 20 cm (sufficiently away from the tank side walls). For the angled-bed cases ($\alpha > 0°$), the camera was tilted on its side at the corresponding angle α and aligned so that the surface of the sediment layer appeared horizontal to the base of each image. Since the relative density of diakon particles (here labelled H-K) ($s = 1.18$) is comparable to that of the pliolite (tracer) particles ($s = 1.02$), the PIV measurements for the critical condition for the diakon particles, the sediment bed was replaced with comparably sized ballotini particles to prevent the entrainment of diakon particles into the flow which would affect the PIV measurements. Attention was focussed on the measurements of the r.m.s. horizontal u and vertical w velocities at near-bed region. It should be noted that various size

ranges i.e. from $d = 80 \sim 1100\,\mu$m were used. However, particle J and K was omitted from the bed slope analysis at $\alpha \geq 20°$ due to the low turbulent Reynolds number Re_l produced at the point of critical threshold sediment motion. At low Re_l, it was found out that the turbulence structure was notably different from that observed from the standard profiles in previous research. This will be further discussed in detail in the next section.

It was decided to use artificial sediments instead of natural particles to eliminate the variability associated with the effects of consolidation time, irregularity in shape and gradation found in natural sediments. (Medina, 2002) using turbulence generated by oscillating-grid to characterise the critical condition for natural sediment motion concluded that sediments with longer consolidation time needed 60% higher critical lift-off r.m.s. velocity than sediments with shorter consolidation time. Additionally, the use of narrowly distributed sediment (about mean diameter) is also important to eliminate the 'armoring' effect which can exist in heterogenous sediment beds. It was also reported by Gyr (1983), Schmeeckle et al. (1998) and Nelson et al. (1995) that hydraulically rough boundaries with heterogeneous particles may also contribute to sediment dislodgement through vortex shedding from individual particles, particle clusters and bedforms. Therefore, utilising a uniform particle size distribution of sediment in this investigation is considered essential.

3.1.1 Particle Size Distribution

To obtain a detailed description of the size distribution, two methods of analysis were used, namely the laser diffraction technique (RODOS) for smaller particle sizes ($d < 500\mu$m) and macroscopic image analysis (using ImageJ software) for larger particle sizes ($d \geq 500\,\mu$m). Although it was desirable to use one technique for all sediment sizes, there were restrictions on using the laser diffraction technique on the larger particle sizes for several reasons. Firstly, the lens required for measuring larger particle ranges was not available. Secondly, the larger particles would have created a smaller sample size, thereby reducing the accuracy of the measurement.

This analysis was conducted to obtain the particle size distribution curve and to investigate the sphericity of the particles. From the curve, the mean diameter d_{50}, that is the sediment size at the 50% cumulative percentile (for each particle type) were obtained. Analysis also is extended to examine the geometric standard deviation $\sigma_g = \sqrt{d_{84}/d_{16}}$, which is the standard gradation parameter and gives the measure of a particle distribution. Sediments are categorised as 'uniformly graded' when $\sigma_g < 1.4$. Note that d_{84}

and d_{16} denote the sediment size at the 84% and 16% cumulative percentile, respectively. Throughout this study, the sediment size is defined as the mean diameter $d \approx d_{50}$.

Smaller particles sizes $d < 500 \, \mu$**m**

The size distribution for particles sizes $d < 500 \, \mu$m, was obtained by the laser diffraction technique using the dry disperser RODOS/M with vibratory feeder VIBRI (Sympatec GmbH). The analysis was conducted in a private external laboratory and the summary of the RODOS specification is given in Appendix B. Table 3.2 shows the particle diameter $d = d_{50}$ values, σ_g and the associated errors, presented here as a standard deviation σ_d for each particle type. It can been seen that all error estimates obtained, by averaging the standard deviation σ_d of 3 tests, are less than 5% of the mean values. The relative smallness of errors obtained is attributed to the fact that the particles are very spherical (see Figure 3.3). All smaller sediments ($d < 500 \, \mu$m) are found to be uniformly graded where the geometric standard deviation $1.1 \leq \sigma_g < 1.3$, well below the criteria.

Label	$d \, \mu$m	$\sigma_d(\pm\mu$m)	σ_g
D	373.9	2.2	1.16
E	220.3	9.4	1.20
F	153.3	2.0	1.15
G	80.0	2.0	1.29
I	273.8	8.4	1.27
J	157.4	0.1	1.10
K	118.7	1.3	1.24

Table 3.2: Error estimation of particle sizes with the laser diffraction technique (RODOS).

The near-uniformity of the sediments are supported by the fact that small ranges of sediment grain sizes were found in the particle size distribution curve as demonstrated in Figure 3.2. For clarity, distribution curves for Particle D (which is largely representative) and Particle G (which exhibits the largest degree of variability) are shown. Each corresponding curve is distinguished by a different line colour (see caption). The corresponding sediment sizes d_{50}, d_{84} and d_{16}, respectively were also shown, in order to better illustrate the particle size distribution. The small range between d_{16} and d_{84} was observed for both particle types discussed in Figure 3.2.

Smaller particle images were taken using a Leitz Orthoplan lens linked to a Zeiss AxioCam camera with 100× magnification. Figure 3.3 shows images of the smallest sizes
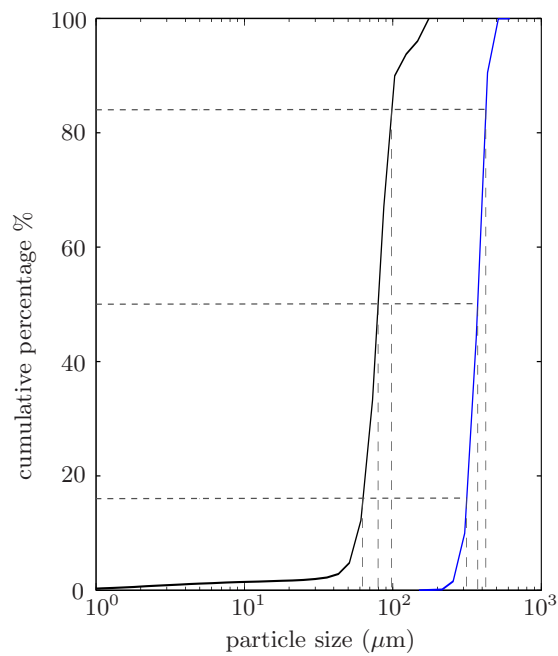
Figure 3.2: The cumulative particle distribution for sediment sizes $d < 500\,\mu$m of Particle D $d_{50} = 374\,\mu$m (blue line) and Particle G $d_{50} = 80\,\mu$m (black line). The background lines show corresponding sediment size at cumulative percentage of 16%, 50% and 84%, respectively.

of ballotini (Particle G) and diakon (Particle K). The particles are consistently spherical in shape. Note that all the smaller (with $d < 500\,\mu$m) sediments were found to have very similar near-spherical characteristics.
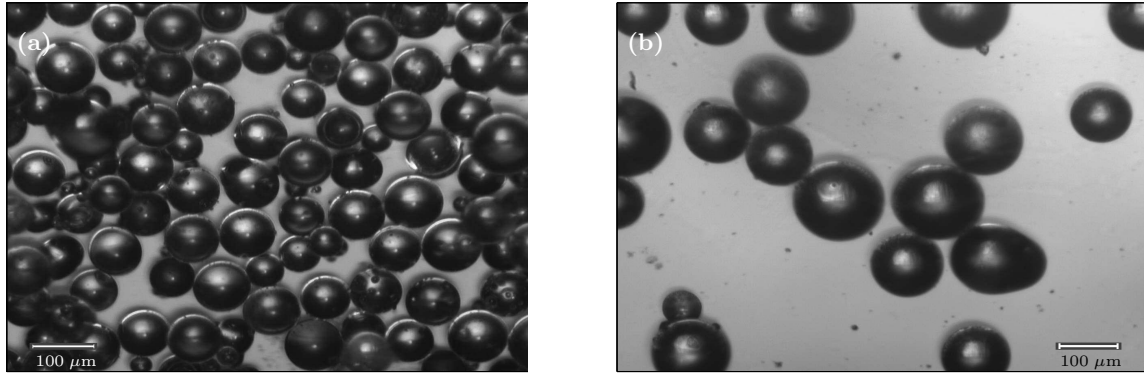
Figure 3.3: Images of (a) Particle G, $d \approx 80\,\mu$m and (b) Particle K, $d \approx 119\,\mu$m with $100\times$ magnification.

Particles with $d \geq 500\,\mu$m

The size distribution analysis for larger particle sizes $d \geq 500\,\mu$m was performed by image analysis with ImageJ, a public domain Java-based image processing program developed at the National Institute of Health (NIH). Images of each particle type were taken using IntelPlay (Intel PC) camera with $10\times$ magnification. An image of $1 \times 1\,\text{mm}^2$ squares was also taken, and is used to give the physical (length) scale of the images. The images were then uploaded to ImageJ and the sizes were obtained by calculating the diameter of each of the loose particles in each image. For each sediment size, the value of d_{50} was obtained by averaging over a total sediment population of 200, producing statistically reliable results.

Label	d_{50} (μm)	$\sigma_d(\pm\mu$m)	σ_g
A	1101.5	107.3	1.07
B	716.1	77.1	1.11
C	562.6	67.1	1.14
H	751.1	98.2	1.13

Table 3.3: Error estimation of larger particle sizes ($d_{50} > 500\,\mu$m) using macroscopic image analysis.
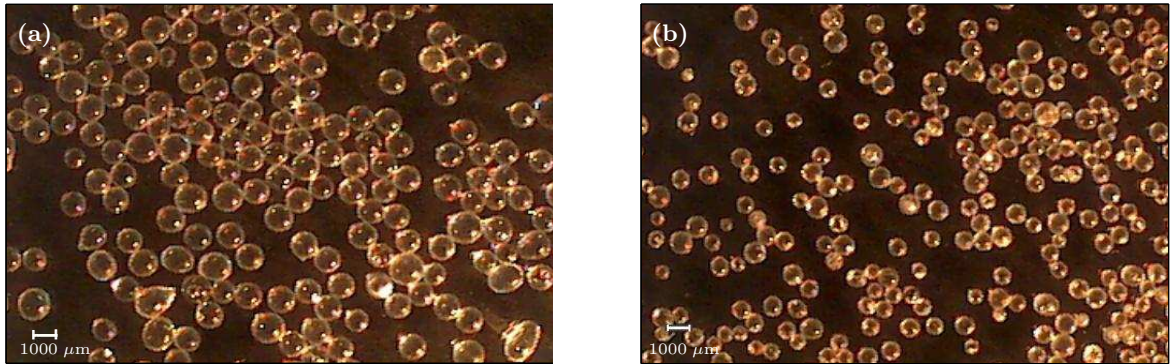
Figure 3.4: Macroscopic image of the larger particles. Sediment used here is (a) Particle A with $d \approx 1100 \, \mu$m (b) Particle H with $d \approx 750 \, \mu$m and with $10\times$ magnification.
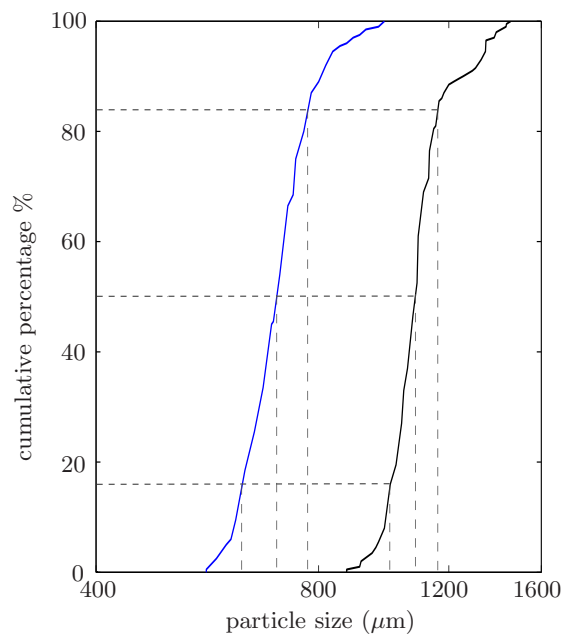
Figure 3.5: The cumulative particle distribution for sediment sizes $d > 500 \, \mu$m of Particle A $d_{50} = 1087 \, \mu$m (black line) and Particle B $d_{50} = 701 \, \mu$m (blue line).The background lines show corresponding sediment size at cumulative percentage of 16%, 50% and 84%, respectively.

The error estimation, calculated as standard deviation σ_d, for larger particles was found to be much bigger than the smaller particles as shown in Table 3.3. All errors are within 10% except for particle H, which has an associated error of 13%. Initially poor sorting of the H particles may have contributed to the large variation of size. Nevertheless, the sediments tend to be relatively well sorted, with the geometric standard deviation σ_g values varying from 1.07 to 1.14. The σ_g values for each particle type are found to be less than 1.4, well below the limit of uniformly graded sediment criteria. This is also supported by the narrow particle size distribution around mean as shown in Figure 3.5, that shows the distribution curves for Particles A and B, respectively. With σ_g values closer to 1, the larger particle size were more uniformly graded than the smaller particle sizes. Although magnified snapshots of all the larger particles available in this study were taken, Figure 3.4 highlights only the $10\times$ magnification of the largest ballotini (A) and diakon (H) particles. In all cases, the larger ballotini and diakon sediments were consistently near-spherical.

3.2 Turbulence in the near-bed region

Before the critical conditions for sediment motion are presented, the turbulence characteristics in the near-bed region (and the development of inhomogeneity due to the presence of the sediment bed) are first discussed. The profiles of the r.m.s. horizontal u and vertical w velocities in the near-bed region were analysed and compared with the previous experimental results and theoretical predictions described by Hunt and Graham (1978). Utilising the methods of rapid distortion theory (RDT), Hunt and Graham (1978) proposed the theoretical model describing the inviscid processes in a zero-mean flow boundary layer. This model describes the instantaneous response of an isotropic (and homogeneous) turbulence when an impermeable surface is inserted. One of the main predictions of the Hunt and Graham (1978) theory is that the tangential turbulent intensities increase at the expense of the normal ones near the surface.

3.2.1 Inhomogeneity

For the experiments described here, the flow in the near-bed region, known as the surface-influenced layer, evolves spatially and with time. This layer has thickness of order l to $2l$ above the bed surface and is divided into two regions (Magnaudet, 2003; Bodart et al., 2010). One, the thin viscous layer emerging adjacent to the bed surface due to the no slip condition, where the flow within is laminar. Secondly, outside this viscous sublayer,
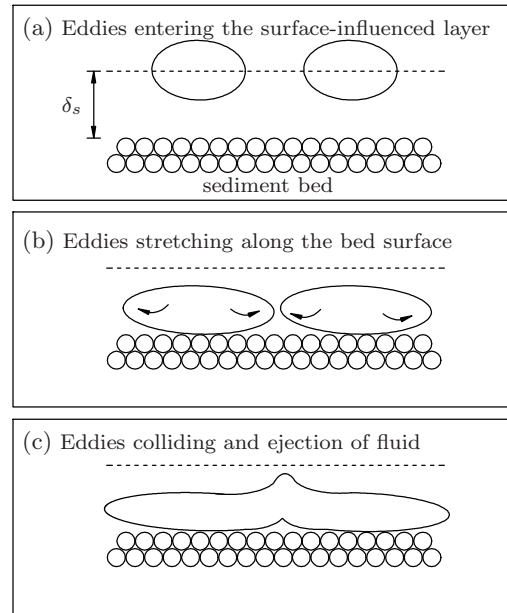
Figure 3.6: Schematic of changes in turbulence structure at near-bed region. δ_s denotes the thickness of the surface-influenced layer. Diagrams show (a) eddies entering δ_s, (b) eddies stretching (splat) and (c) collision of stretched eddies (antisplats).

is a region roughly one integral length scale (l) thick known as the 'source layer' where the superposition of the turbulent velocity fields on incoming quasi-isotropic homogeneous turbulence occurs. Previous studies have shown that within this surface-influenced layer, the structure of (initially quasi-isotropic homogeneous) turbulence changes (Hunt and Graham, 1978; Magnaudet, 2003; Bodart et al., 2010). Figure 3.6 shows a representation of how the turbulence structure adjusts to the presence of the sediment bed. Note that here the sediment bed is assumed to be a rigid boundary. When homogeneous fluid blobs enter the surface-influenced layer and impinge on the bed surface, the fluid blobs are subjected to the kinematic boundary condition $w = 0$. The impinged fluid blobs results in stagnation points occurrence at the boundary layer and is characterised by a negative gradient to the normal velocity. The associated high pressure provide a negative contribution to the normal component of the pressure-strain terms, which transfer the momentum from normal velocity component to the tangential velocity components. These are known as 'splat' events (see Figure 3.6(b)) (Perot and Moin, 1995; Magnaudet, 2003; Bodart et al., 2010). As the eddies reach the bed surface, the vorticity within the eddies is stretched tangentially parallel to the bed, increasing the diameter of the eddy. When the tangential motions resulting from the impingement of two neighbouring splats coincide as shown in

Figure 3.6(c), another stagnation point, where the normal velocity experiences a positive gradient, is produced. This results in fluid being ejected (in the normal direction) from the surface, and this event is known as an antisplats (Perot and Moin, 1995). The splat events correspond to the high momentum fluid being transported toward the sediment bed (sweep) and the antisplats correspond to the ejection of low momentum fluid into the outer flow above the bed. Similar sweep and ejection events have been observed due to the generation of coherent funnel vortices in the near boundary region of a turbulent channel flow (Recall Figure 1.2) (Kaftori et al., 1995). In viscid flow, the viscous friction along the bed prevents the total amount of kinetic energy from bulk flow being transferred to the tangential components by the splat events. Consequently, lower energy is restored back to the normal component by the antisplat event. Thus, it is possible that the antisplat events might not occur or only weak antisplats occur (Bodart et al., 2010). This continuous splat-antisplat process creates inhomogeneous and anisotropic turbulence in the near-bed region.
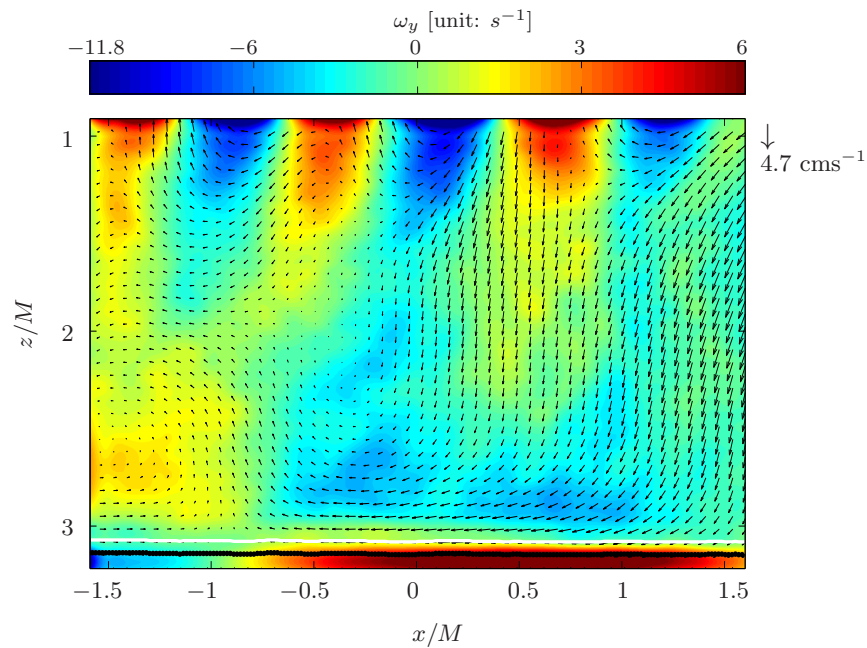
Figure 3.7: Mean velocity fields with time averaged vorticity as background. Turbulence data is produced using $S=8$ cm, $f_g = 2.2$ Hz, $Re_M = 8800$ and the velocity fields was averaged over $T = 45$ s. The arrow $\downarrow$ indicates the maximum value of velocity component. Blue contours indicate negative vorticity (clockwise) and red-yellow contours indicate positive vorticity (counterclockwise). Filled circle indicate the bed surface and the white solid line represents the distance equivalent to the interrogation window above the bed surface.

Figure 3.7 shows typical time-averaged mean velocity fields and vorticity distributions from $z \approx M$ to the sediment bed surface at $z \approx 3.2M$. The width spanning up to $3M$ at the centre of the tank (the tank side wall is approximately at $x/M = 3$ and $x/M = -3$). Coherent positive and negative vorticities are clearly present near the grid with each coupled vortex pair spanning a distance M (corresponds to the mesh size). At this point, high turbulent kinetic energy is available due to the interaction of wakes and jets. Moving away from this turbulence production layer, the vorticity starts to dissipate and enters the quasi-isotropic homogeneous region at $z \approx 2M$. Within this region, the turbulence decays spatially in the vertical direction and obeys the Equation (1.10) (discussed previously in Chapter 2). Further away, the flow enters the surface-influenced layer and is subjected to kinematic (impermeability $w = 0$) and dynamic (no slip $u, v = 0$) conditions. The influence of the kinematic boundary condition ($w = 0$) reduces the vertical velocity component (which will be discussed further in the next section). An energetic eddy impinging on the near-bed surface results in a vortex being stretched along the bed surface, increasing the diameter of the eddy. Figure 3.7 shows that within this region at $z \approx 3 - 3.2M$, high intensity positive and negative vorticities are visible at near the sediment bed. The mean velocity fields show a notable (large scale) secondary flow with negative vorticity at $-1.5 \leq x/M \leq -0.5$ and positive vorticity at $-0.5 \leq x/M \leq 1.5$. These opposite (of direction) large scale motions has the vertical size up to $\approx M$ above the bed surface (see Figure 3.7 at $-1.5 \leq x/M \leq -0.5$). The existence of these large scale motions at near-bed region resulted in a narrow margin of visible quasi-isotropic homogeneous turbulence (i.e. at $z = 2.5M$) in Figure 3.7, particularly at $-0.5 \leq x/M \leq -1.5$. Back to the near-bed region, when the fluid (blob) enters the viscous sublayer, the velocity gradient adjacent to the bed surface is high. Thus, the no slip condition at the bed surface induces vorticity of the opposite sign in the layer very close to the bed surface. For example, the induced large scale motion at $-0.5 \leq x/M \leq 1.5$ produced stretched eddies with positive vorticity, which spanned up to $2M$. The large scale motion at $-1.5 \leq x/M \leq -0.5$ also show corresponding stretched negative vorticity. However, the (significant in opposite direction) vorticites at sediment bed maybe an erroneous phenomena contributed from the fact when the images were processed in the Digiflow, the sediment bed was masked black. Such masking affected the calculation of vorticity i.e. the masked bed indicate that the flow within the bed is stationary (or zero), giving an erroneous high velocity gradient (shear). This resulted the distinctive opposite rotation of vorticities at $-1.5 \leq x/M \leq 1.5$. The solid white line in Figure 3.7 shows an area of inaccurate vorticity representation due

to the interrogation window in the PIV calculation.
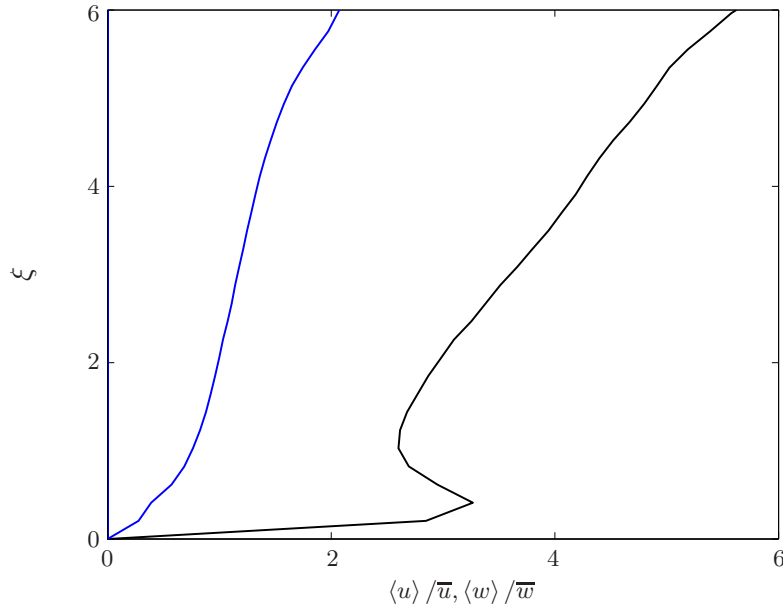
Figure 3.8: The horizontal $\langle u \rangle / \overline{u}$ (black solid line) and vertical $\langle w \rangle / \overline{w}$ (blue solid line) turbulence intensity against the normalised distance above the bed surface ξ. The data was generated by $S = 8$ cm and $f_g = 2.2$ Hz.

Figure 3.7 shows that the presence of the sediment bed changes the turbulence structure and that there is notable mean secondary flow in the near-bed region. This erroneously indicate that the mean velocity is the influential component and not the turbulence. Subsequent analysis will demonstrate that the turbulence is still the dominant component in the near-bed region. Figure 3.8 shows the horizontal and vertical turbulence intensity $\langle u \rangle / \overline{u}$, $\langle w \rangle / \overline{w}$, respectively, spanning from the bottom of the grid to the bed surface. The data shown corresponds to the turbulent flow plotted in Figure 3.7. It has been shown that the turbulence intensities, in particular the horizontal turbulence intensity $\langle u \rangle / \overline{u}$ is highest near the grid ($\xi = 6$). The horizontal fluctuating components are the dominant components throughout the bulk flow and the surface-influenced layer. Note that the vertical turbulence intensity $\langle w \rangle / \overline{w}$ is significantly lower than the horizontal components. This is due to the higher mean vertical velocity $\overline{w}$ contributed by the uniaxial of fluid forcing. With high turbulence intensity, particularly for the horizontal component, the turbulence in the near-bed region is appropriate to investigate the critical criteria of incipient sediment motion.

The r.m.s. velocity profiles and isotropy ($\langle w \rangle / \langle u \rangle$) for the whole depth are presented
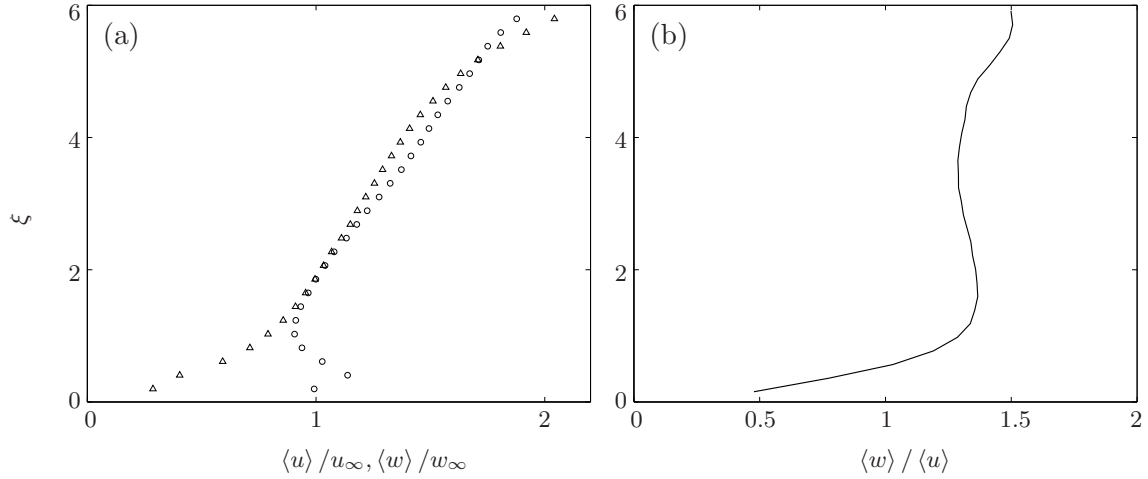
Figure 3.9: (a) The normalised r.m.s. horizontal ($\circ$) and vertical ($\triangle$) velocity components versus the normalised distance from surface. The r.m.s. velocities u_∞ and integral lengthscale l_∞ obtained within the homogeneous region were used for the normalization. (b) The evolution of isotropy $\langle w \rangle / \langle u \rangle$. Data is taken from $S= 8$ cm, $f_g = 2.1$ Hz and $Re_M = 8400$.

in Figure 3.9(a) and (b), respectively. The plot in Figure 3.9(a) displays both dimensionless horizontal and vertical fluctuations $\langle u \rangle / u_\infty$ and $\langle w \rangle / w_\infty$ against $\xi = \mathcal{Z}/l_\infty$, where $\mathcal{Z}$ is the vertical distance away from the sediment bed and $\mathcal{Z} = 0$ refers to the bed surface (see Figure 3.1). The subscript ∞ refers to the values of quantities in the homogenous region at $z = 2.5M$. Figure 3.9(a) shows that both the horizontal and vertical velocity components have highest values near the grid (at $\xi = 6$) and steadily decrease toward to the bed surface. For $0 \le \xi \le 1.5$, the vertical velocity component $\langle w \rangle / w_\infty$ decreases monotonically to zero and the horizontal velocity component $\langle u \rangle / u_\infty$ begins to amplify. The height $\xi = 1.5$ provides an initial boundary of the surface-influenced layer. The onset of the surface-influenced layer can also be determined by observing the isotropy $\langle w \rangle / \langle u \rangle$ values in the near-bed region, where the surface-influenced layer starts when the isotropy initially decrease to zero (Bodart et al., 2010). Figure 3.9(b) shows the isotropy $\langle w \rangle / \langle u \rangle$ profile in the bulk flow. Data illustrates that the isotropy $\langle w \rangle / \langle u \rangle$ is greatest near the grid, that is anisotropic region due to the production of the turbulent kinetic energy by the grid oscillation. Moving further away from the grid, the isotropy begins to decrease to a relatively constant value at approximately 1.3 before experiencing a sharp decrease at $\xi \approx 1.5$. The thickness of surface-influenced layer then, is approximately $1.5l$, which is comparable to the range (l to $2l$) reported by Magnaudet (2003). Note that for the

experiments described here, Figure 3.9 is a representative turbulence profile in the bulk flow for all of the data. Similar velocity profiles in the near-bed region for varying ranges of Re_l are shown in Figure 3.12. The plot is to examine the the limit of Re_l, which will be extensively discussed in next section. The changes of turbulence structure within the surface-influenced layer, that is the turbulence is inhomogeneous, the HT equation (i.e. Equation (1.10)) is invalid.
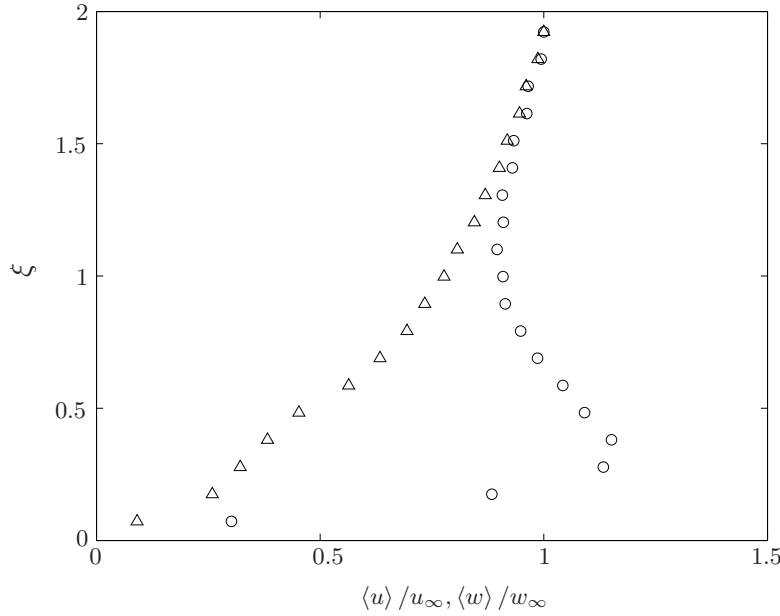
Figure 3.10: The dimensionless horizontal ($\circ$) and vertical ($\triangle$) r.m.s. velocity profile plotted against distance ξ above the sediment bed. The turbulence was generated using S=8 cm, f_g=2.2 Hz, $Re_M = 8400$, $Re_l = 508$.

Because the surface-influenced layer is of primary interest, Figure 3.10 plots both dimensionless r.m.s. horizontal u and vertical w velocity between $\xi = 0$ to 2. The data shows that the w component monotonically decreases as $\xi \to 0$, due to viscous damping. The strong damping of the normal turbulent intensity within the surface-influenced layer due to the kinematic boundary condition inhibits the transport of turbulence by itself (Perot and Moin, 1995). Figure 3.10 suggests that within the surface-influenced layer, the u component experiences an amplification between $0.3 \leq \xi \leq 1$, attaining a peak value at $\xi \approx 0.3$. The amplification of u is observed due to a large scale eddy impinging on the bed stretching the tangential vorticity components, amplifying the small scale horizontal turbulence (Hunt, 1984). The distance ξ where the near wall peak u is observed is within the range obtained by previous studies $0.2 \leqslant \xi \leqslant 0.4$ (Brumley and Jirka, 1987; Aronson

et al., 1997). The maximum amplification observed in $\langle u \rangle$ is about 20% higher than u_∞. For all the data, the maximum (amplification) of $\langle u \rangle$ observed were within the range of $0.8u_\infty$ to $1.2u_\infty$. The amplification depends on the flow strength. Hunt and Graham (1978) suggest that increasing the Reynolds number by a factor of 10 result in an amplification of 30%. Note that for all the range of Re_l used in this experiment, consistently similar trends to the data presented in Figure 3.10 were observed.
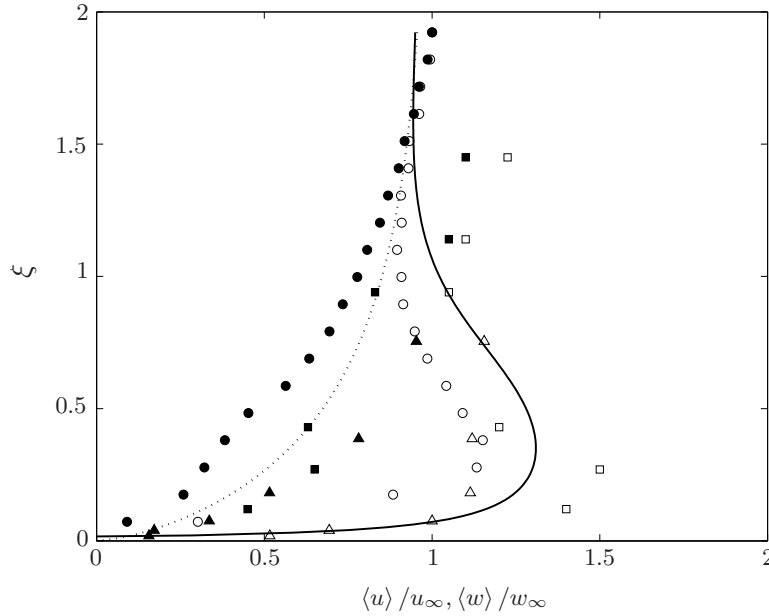
Figure 3.11: The r.m.s. velocity profiles within surface-influenced layer plotted together with data generated by $S = 8$ cm and $f_g = 2.2$ Hz, shown here as ($\circ$). Data extracted from Brumley (1987) and Hannoun (1998) are presented as ($\triangle$) and ($\square$), respectively. The predicted lines derived by Hunt (1978) are also shown as solid line and dashed line for u and w velocity components, respectively. Open bullets and filled bullets represent the dimensionless r.m.s. horizontal and vertical components, respectively.

The same data in Figure 3.10 was also compared with the results from previous experimental work and the theoretical prediction of Hunt and Graham (1978) as shown in Figure 3.11. The experimental data from previous work was obtained from Brumley and Jirka (1987) and Hannoun et al. (1988), who analysed the interaction of oscillating-grid turbulence with a free-surface and a solid plate, respectively. Although the dynamic boundary condition for a free surface (i.e. work of Brumley) is different (where only $w = 0$), it appears that the anisotropy of the fields is insensitive to the precise nature of the dynamic boundary condition across the surface-influenced layer (Bodart et al., 2010). Thus, a com-

parison of data with velocity profile obtained by Brumley and Jirka (1987) is allowed. Note that this analysis was conducted to compare the turbulence profile measured in this study with previous established findings, particularly when the boundary used here is a sediment bed, that is neither a free surface nor a solid boundary (which are available in the literature). The profile for u will be first discussed. Figure 3.11 shows that the r.m.s. horizontal velocity components produced similar profile. From $\langle u \rangle / u_\infty = 1$ at $\xi = 1$, the $\langle u \rangle / u_\infty$ values are amplified in the surface-influenced layer reaching a maximum peak at $\xi = 0.2 - 0.4$. All profiles showed an amplification before decreasing close to zero at the boundary due to viscous damping. The r.m.s. vertical velocity w within the surface-influenced layer is seen to monotonically decrease to zero at the boundary. Hunt (1984) reported that although there might be an amplification of w component, it is not significant due to the wall blocking effect. Both u and w velocity components within the surface-influenced layer were found to exhibit comparable profiles to the theoretical prediction of Hunt and Graham (1978). The near-wall peak for the u component is observed at $\xi \approx 0.3$ as predicted by the theoretical curves, shown in Figure 3.11. The r.m.s. horizontal and vertical velocity components measured here (shown here as (○)) had lower values compared to the theoretical prediction as illustrated in Figure 3.11. The underestimation of values measured is due to the viscous effect in the viscous sublayer, decreasing the availability of energy in the horizontal components to amplify. Note that the derivation of Hunt and Graham (1978) theory is developed based on the inviscid process at the boundary layer. The decrease in w and amplification of u within the surface-influenced layer confirmed the occurrence of 'splat-antisplat' events in the near-bed region.

It has been established that the generated turbulence provide comparable standard r.m.s. velocity profiles with the theoretical prediction and profile obtained from experimental works, particularly within the surface-influenced layer. Due to the varied range of turbulent Reynolds number Re_l used in the experiments, where at low Re_l it has been shown (by Perot and Moin (1995)) not to follow the theory of Hunt and Graham (1978), the limits for Re_l for the critical sediment motion experiments needs to be determined.

3.2.2   Range of turbulent Reynolds number Re_l

Previous studies have considered the range of Re_l for which the u amplification and decreasing w component (i.e. 'splats/antisplats' events) have been observed (Hunt and Graham, 1978; McDougall, 1979; Hannoun et al., 1988). Here, we analyse whether this structure

was consistently observed for the range of Re_l to be used in the experiments to identify the critical conditions for sediment movement (for the sediment types used here). Recall that Re_l is calculated as $Re_l = ul/\nu$. The velocity profiles for the range of turbulent Reynolds number $70 < Re_l < 570$ are then analysed, over which the r.m.s. velocity profiles predicted by Hunt and Graham (1978) is expected to be observed.

The findings of McDougall (1979) and Hannoun et al. (1988) suggest that the u amplification in the surface-influenced layer does not occur for Re_l within the range $40 < Re_l < 120$. The limit can serve as an initial basis. The horizontal and normal velocity components for five different Reynolds numbers Re_l are plotted in Figure 3.12 against distance above the bed surface $\xi = Y/l_\infty$. Note the variation in Re_l is only due to the frequency (f_g) changes since the stroke S was fixed and the grid geometry remained unchanged. Analysis of the u component will be discussed first. Figure 3.12(a) shows the r.m.s. horizontal velocity $\langle u \rangle /u_\infty$ behaviour in the region $\xi = 0$ to 2, for a Reynolds number range $120 < Re_l < 580$. The data shows an amplification of u for this range of Re_l, with the near wall peak reaching $\langle u \rangle /u_\infty \approx 1.2$ at $\xi = 0.3$ or 0.4. For $\xi \geq 1$, $\langle u \rangle /u_\infty \approx 0.8$ to 1.1. The profiles become steeper at the wall as Re_l increases, suggesting there are higher velocity gradients at the near-bed region. Note that when $Re_l > 200$, the amplification of u component reached almost 1.2. Furthermore Perot and Moin (1995) found when the Reynolds number is high, the increasing pressure-strain term enhanced the inter-component energy transfer from w to u and contributed to more amplification of the horizontal velocity components. For the lower $Re_l = 124$ value, although the amplification is still visible at $\xi \approx 0.4$, the r.m.s. horizontal velocity $\langle u \rangle /u_\infty \approx 0.8$. This suggests that for low Re_l, as the eddies impinge on the bed, the momentum energy transferred from the vertical velocity component to the horizontal velocity component (splats) was reduced due to viscous dissipation and was further decreased by the viscous friction (within the viscous sublayer). Thus, the energy to amplify tangential vorticity components is less, leaving relatively weak energy for u amplification.

Figure 3.12(b) shows that the $\langle w \rangle /w_\infty$ components consistently decrease monotonically in the surface-influenced layer for $120 \leq Re_l \leq 580$. At $\xi \leqslant 0.2$, independent of Re_l, the near wall profile collapsed onto a single profile that sharply decreases to zero in the viscous sublayer, where the viscous effect is significant.

The turbulence variation in the near-bed region for flow conditions with $Re_l \leq 100$ are plotted in Figure 3.13. The plot demonstrates that the $\langle u \rangle$ and $\langle w \rangle$ profiles for lower Re_l do not yield a qualitatively similar profile in comparison to flows with higher Re_l,
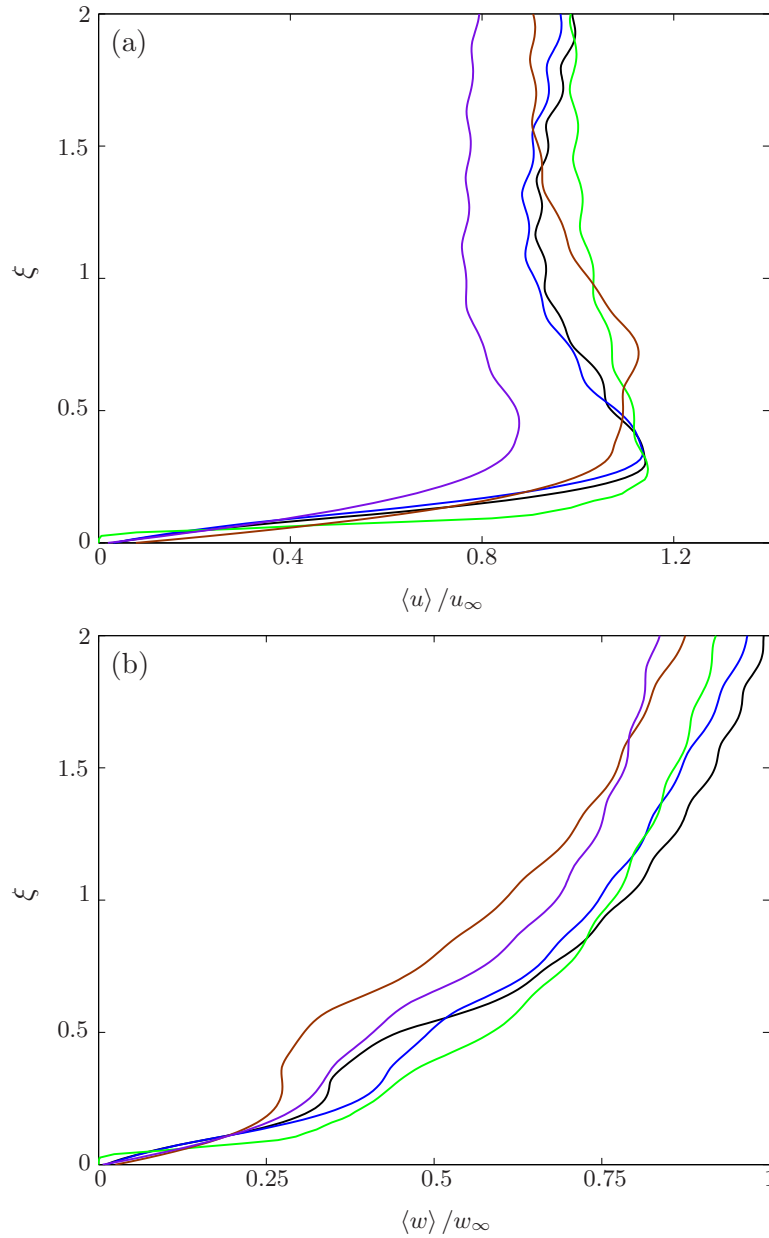
Figure 3.12: Comparison for turbulent Reynolds number $Re_l > 120$ of (a) horizontal and (b) vertical r.m.s. velocity components. Data correspond to from S=8 cm with varying frequency $0.9 \leqslant f_g \leqslant 3$ Hz. Solid lines of black, blue, green, brown and purple colours represent $Re_l = 570, 440, 325, 209, 124$, respectively.
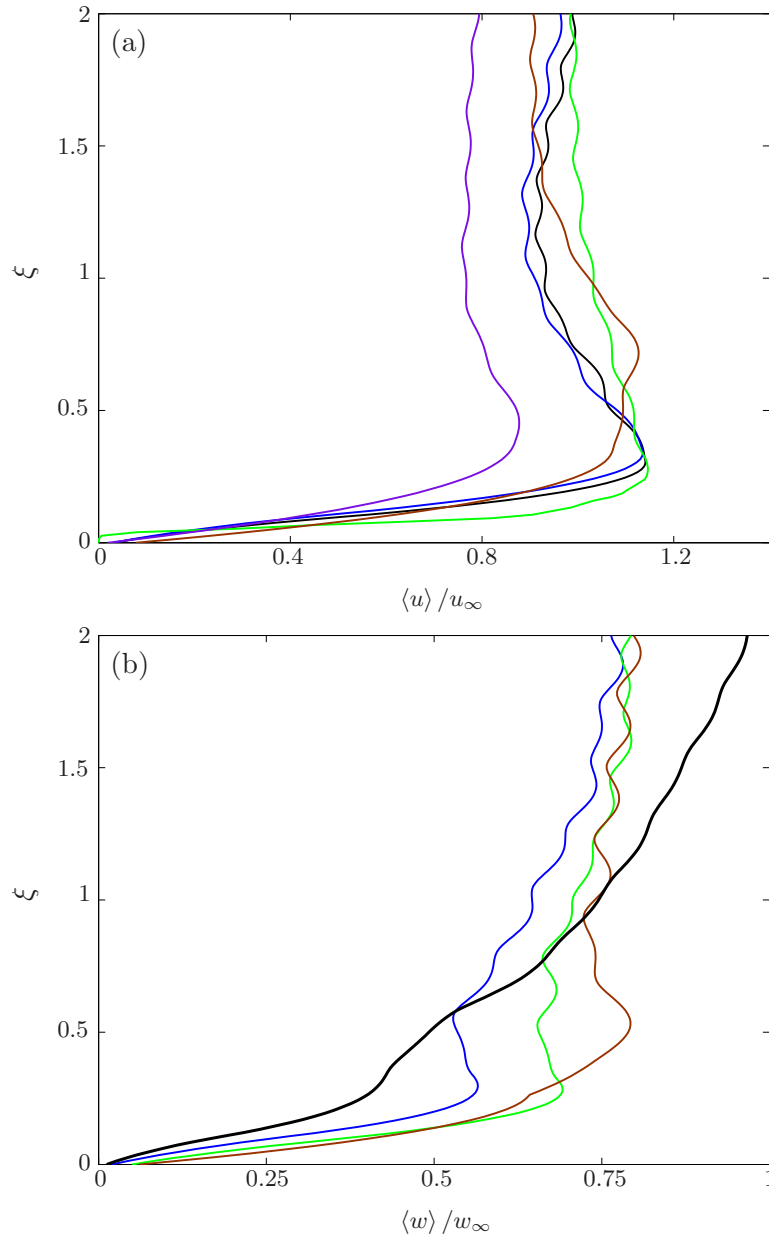
Figure 3.13: Comparison for turbulent Reynolds number $Re_l < 120$ for mean spatially averaged (a) horizontal $\langle u \rangle$ and (b) vertical $\langle w \rangle$ r.m.s. velocity components. Data correspond to S=8 cm with varying frequency $0.6 < f_g < 0.8$ Hz. Solid lines of blue, green and brown colours represent $Re_l = 95, 76$ and 74, respectively. The profile of $Re_l = 475$ shown as thick black solid line represents the comparison to the standard velocity profile at near bed region.

suggesting appreciable changes in the turbulence structure within the surface-influenced layer. Note that, the data for higher $Re_l = 475$ is also shown in Figure 3.13 for comparison. The r.m.s. horizontal velocity components have no amplification and a non-monotonic decrease of r.m.s. vertical velocity components at near-bed region were identified. A near-constant value of $\langle u \rangle / u_\infty$ was maintained up to $\xi = 0.3$ before decreasing to zero. The vertical component $\langle w \rangle / w_\infty$ also reaches a relatively constant value, then has a slight amplification at $\xi \approx 0.3$ before decreasing sharply to zero. For low Re_l, the thickness of the viscous sublayer increases (shown in Table 3.4), thus the viscous effect on the bulk flow is extended further within the surface-influenced layer, significantly affecting both u and w. The turbulence structure at lower Re_l is notably different than the standard profile produced at higher Re_l. Given the changes in turbulence structure for the lower Reynolds number Re_l, the experiments for the critical criteria for sediment motion were always in the range $Re_l > 100$.

Exp	Re_l	ξ	$\mathcal{Z}/M$	$\delta_v^\dagger/l_\infty$
I	570	0.308	0.110	0.084
II	440	0.383	0.100	0.095
III	325	0.404	0.113	0.111
IV	209	0.456	0.126	0.139
V	124	0.423	0.110	0.180
VI	74	N/A	N/A	0.232

Table 3.4: Summary of turbulent Reynolds number Re_l with corresponding dimensionless distance ξ where near wall maximum u velocity occurred and the dimensionless thickness of the viscous sublayer δ_v. Note that $\delta_v^\dagger$ denotes the viscous sublayer calculated as $\delta_v = 2l_\infty Re_l^{-1/2}$ as provided in the study of Magnaudet (2003). The third and fourth columns are the corresponding distances $\mathcal{Z}$ in terms of l_∞ and M where u amplification occurred.

To demonstrate the similarity of the turbulence profile in the near-bed region for $Re_l > 100$, Table 3.4 shows the heights ξ and Y/M where the maximum of $\langle u \rangle / u_\infty$ was observed for various values of Re_l. Also shown are the corresponding values of the viscous sublayer thickness δ_v made dimensionless with l_∞, which is noted to have an expected inverse relationship with the turbulent Reynolds number. For low Re_l, viscous damping plays a significant role dissipating the energy and resulting in weak amplification in the near-bed region. This supports the claim of Hunt and Graham (1978) stressing the importance of high Re_l for the occurrence of the near (solid) base peak.

It is interesting to see that for turbulent flow with $Re_l > 100$, the near-wall peak u occurred at a comparable dimensionless distance ξ around $0.3 \sim 0.4$ or at $\mathcal{Z}/M \approx 0.1 \pm 0.02$ (for the Re_l range discussed here). This suggests that the peak value of $\langle u \rangle / u_\infty$ in the surface-influenced layer provides a consistent near-bed velocity scale that can be used to define the Shields parameter θ.

3.3 Critical criteria for incipient sediment motion

This section describes the measurements of the critical conditions required for incipient sediment movement as a function of particle Reynolds number Re_p and bed slope β. Note that in the experiments described here, the bed shear stress τ_b is not measured. Hence, a method of approximating θ was required, using the available velocity data. The experiments of Lyn (1995) and Bellinsky et al. (2005), using oscillating-grids to measure the critical criteria for sediment motion, made the assumption that $\tau_b \sim \rho k$, where $k = \frac{1}{2}(u^2 + v^2 + w^2)$. The Shields parameter was defined as

$$\theta_c = \frac{k}{(s-1)gd}. \tag{3.1}$$

Assuming isotropy ($u \approx v \approx w$), Equation (3.1) becomes

$$\theta_c = \frac{1.5u^2}{(s-1)gd}. \tag{3.2}$$

This approach neglects the inhomogeneity that arises due to the presence of the sediment bed, for which it has been shown that the HT equation is invalid. Bellinsky et al. (2005) introduced an anisotropy coefficient η, giving $k = 1.5\eta u^2$. Taking u as described in Equation (1.10), Bellinsky et al. (2005) defined the Shields parameter as

$$\theta_c = \frac{1.5\eta C^2 (f_g S^{3/2} M^{1/2} z_c^{-1})^2}{g(s-1)d} \tag{3.3}$$

where Bellinsky et al. (2005) used $\eta = 1$, C as 0.25, following the experiments of Hopfinger and Toly (1976) and z_c is the critical distance where u_c is defined. That is, the values of θ_c used in Bellinsky et al. (2005) were functions of frequency, stroke, mesh size and distance away from the grid.

The most important question was how the critical $z = z_c$ value was determined for Equation (3.3). The most ideal point is in the near-bed region where the fluid forces

Name	S (cm)	Re_M	Z (cm)	z_c	range of d (μm)	$s = \rho_s/\rho$
Lyn (1995)	5	≈ 7200	15	in the near-bed region	$150 - 180$	2.46
Medina (2002)	1.2	350 - 600	2.95	at the bed	$71 - 149$	2.3
Liu (2003)	3	1000 - 9000	13-20	$0.5d_{50}$ away from bed	450	1.16
Bellinsky (2005)	3.7	2187 - 4174	9.6	5.08 cm above bottom	$76 - 2000$	$2.3 - 3.84$
Present study (2011)	8	2800 - 12400	16, 18	$\approx 0.1M$ from bed	$80 - 1100$	1.18&2.5

Table 3.5: Summary of past incipient motion research using an oscillating grid. Z denotes the distance from virtual origin to the sediment bed. The symbol z_c defines the distance above the bed surface where u_c is taken for the determination of the critical Shields parameter. The Bellinsky (2005) point was obtained through private communication.

directly act on the particles. For characterisation of θ_c using turbulence generated by an oscillating-grid, various z_c points were used. This is shown in Table 3.5. All of the studies agreed on taking a point in the near-bed region except for the work of Bellinsky et al. (2005) who took at z_c at approximately 5.08 cm from the sediment bed. At this point, Bellinsky employed u_c taken at $25d \leqslant \mathcal{Z} \leqslant 668d$ above the bed surface, large compared to the sediment size. At such distance, the fluid forces obtained will not really be an accurate representation of the actual forces acting on the particles. Therefore, the Shields parameter θ measured at this point will be underestimated.

Medina (2002) and Lyn (1995) both taken the u_c values at $\approx d$ (i.e. the size of sediment examined) above the bed surface. Both studies obtained the θ_c using Equation (3.3), where coefficient $\eta = 1$ was taken and z_c is taken as the distance from virtual origin to the bed surface (i.e. $z_c = z - d$). It was stressed in Section 3.2 that in the near-bed region, the HT equation is no longer valid. While the author understands the conceptual simplicity of adopting the HT equation, the author believes that the significant changes to the turbulence structure in the near-bed region will have a notable impact on the value of u_c which (when calculated with Equation (3.3)) underestimates the actual behaviour. The study of Liu et al. (2006) only employed one sediment size. The critical Shields parameter was obtained using Equation (3.2), where the u_c value is measured at $0.5d_{50}$ (i.e. equivalent to 0.25 mm) above the bed surface. Although using the z_c point at such a height to obtain u_c is an ideal indicator, it is not suitable for the range of sediment sizes described here. The smallest sediment size is $80\,\mu$m, that is the height $0.5d_{50} \approx 0.04$ mm is very small and the fluid velocity measurement techniques to measure at such small distances are not yet available.

Recall that for experiments described here, within the Re_l range available, each experiment showed the amplification of u is within the surface-influenced layer at $\xi \approx 0.3$ to 0.4 above the bed surface (see Figure 3.12(a)). Thus, taking into account the changes of turbulence structure at near-bed region, a different approach to determining u_c was undertaken in this study, which deviates from previous studies (of using Equation (3.3)) (Lyn, 1995; Bellinsky et al., 2005). Let $\langle u \rangle_b$ denotes the horizontal fluid velocity component measured as the peak amplification value, during the interaction period. The $\langle u \rangle_b$ measured at this distance, which is as close to the bed surface is a reliable velocity measurement and could be consistently obtained using the PIV set up described. Under critical impact conditions, sediment grains are brought into motion only by the peak value of the bed shear stress, which is expected to scale with $\sim \rho \langle u \rangle_b^2$. Hence, in the present context, the

Shields parameter was defined as

$$\theta = \frac{\langle u \rangle_b}{(s-1)dg}. \tag{3.4}$$

Thus, the corresponding critical Shields parameter, by taking u_c equal to critical $\langle u \rangle_b$ (i.e. the critical conditions that give rise to the incipient sediment motion) is given by

$$\theta_c = \frac{u_c^2}{(s-1)dg} \tag{3.5}$$

The approach adopted here uses a velocity scale characteristic of the peak variation in the near-bed second order turbulence characteristics. To minimise error associated with u_c, each u_c value was taken by averaging from at least five measurements. The value of u_c was taken as the peak value of $\langle u \rangle_b$ in the range $\xi \approx 0.3 - 0.4$ and was chosen as it is representative of the most energetic turbulent eddies in the near-bed region.

3.3.1 Measurements of critical criteria for a horizontal bed

The measured values of θ_c are now presented. First, attention is focussed on the horizontal-bed case ($\beta = 0$), henceforth denoted θ_{c0}. Using dimensional arguments, Shields (1936) proposed a relationship between the critical Shields parameter and the boundary Reynolds number $Re_* = u_{*c}d/\nu$, which has since largely been verified by experimental data obtained in steady turbulent channel flows (White, 1970; Mantz, 1977). As already noted, the critical bed shear velocity u_{*c} (and hence Re_*) was not measured in the experiments reported here. However, we expect the depth of the inner viscous sublayer within the surface-influenced layer will have thickness of order $\delta_v = (d/Re_l)$. Therefore, under critical conditions, the hydrodynamic drag and lift forces acting on the near-surface sediment grains will depend on k_s/δ_v, where k_s is the (bed) roughness length-scale, which will be $\mathcal{O}(d)$. Hence, for the experiments reported here we expect $\theta_{c0} = f(Re_p, d/\delta_v)$, where $d/\delta_v = u_c d/\nu$.

Figure 3.14(a) shows the values of θ_{c0} plotted against the relative roughness d/δ_v and particle Reynolds number Re_p (in Figure 3.14(b)), for each of the eleven sediment types. Separate data symbols have been used to differentiate between diakon ($s = 1.18$) and ballotini ($s = 2.5$) sediments. The error bars of θ_{c0}, d/δ_v and Re_p are based on the typical variability of d, u_c and w_s. As the term u_c is present in both abscissa and ordinate for the plots of θ_c against d/δ_v and created an inherent problem in the determination of θ_c in open
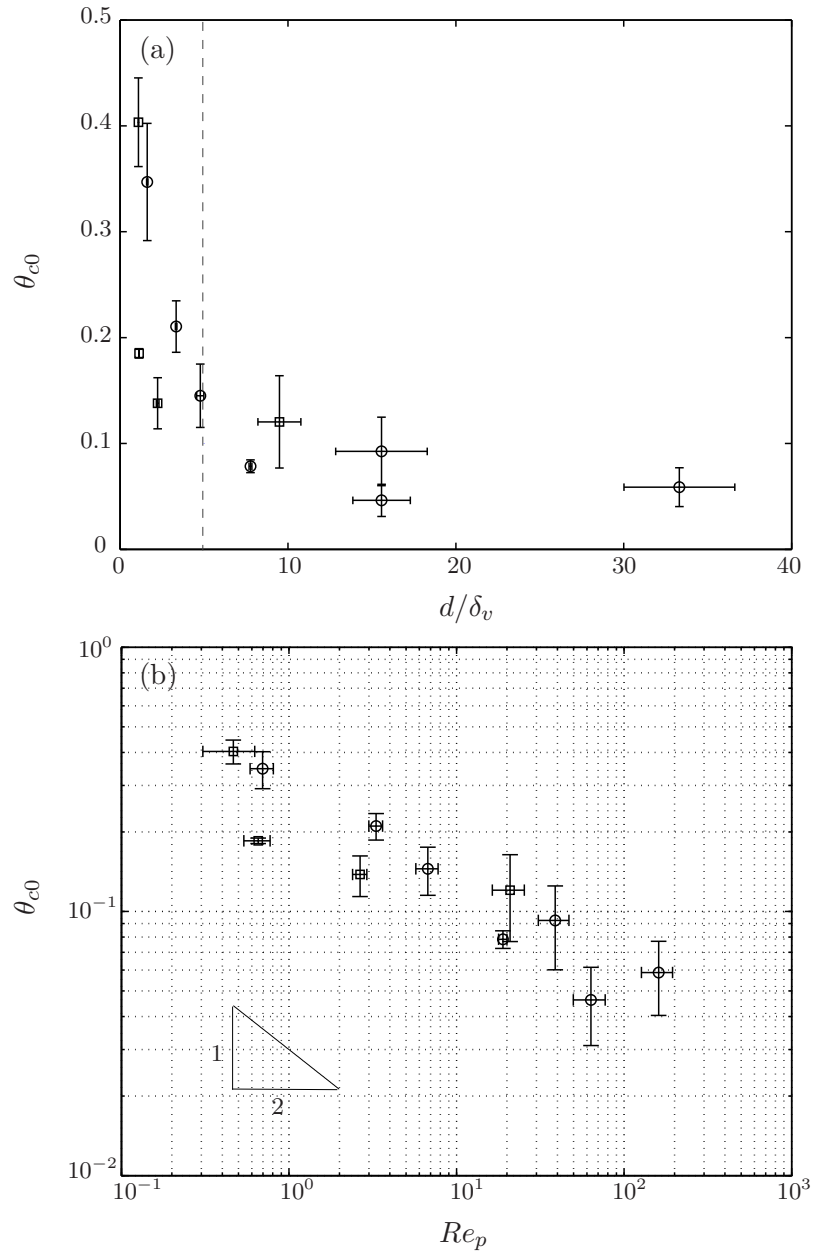
Figure 3.14: Measured values of critical Shields parameter θ_c against (a) d/δ_v and (b) Re_p. Sediments are ballotini ($\circ$), Diakon ($\square$). The dashed line in (a) shows the limit of smooth-bed and the triangle-solid line in (b) shows the theoretical curve $\theta_c \sim Re_p^{-1/2}$. Vertical error bars show the variability in the measured values of u_c whilst the horizontal error bars are from the w_s and d_{50} calculations.

channel flow (Buffington and Montgomery, 1997), the critical θ_c is plotted against particle Reynolds number Re_p. Values of each sediment Re_p are presented in Table 3.1 in Section 3.1. Recall that $Re_p = w_s d / \nu$, where w_s is the terminal settling velocity. This represents the intrinsic properties of the bed material, and is independent of the flow conditions acting on the bed. The measured values of θ_c are plotted against Re_p in Figure 3.14(b). The empirical relation $\theta_c = \iota Re_p^{-n_{og}}$ was obtained using least squares, where ι and n are empirical constants. For the horizontal bed case ($\beta = 0$), empirical constants ι and n_{og} were found to be 0.25 and 0.316, respectively with a fitted line r^2 value of 0.848.

Although the θ_c reported in Figure 3.14 were not obtained using u_{*c}, as in the critical shear velocity in steady turbulent channel flows, a number of qualitative consistencies can be identified. In particular, White (1970) classified bedforms, under threshold conditions, as hydraulically smooth or rough. For the experiments considered here, a hydraulically rough bedform corresponds to when the roughness length-scale (k_s) is comparable to (or larger than) the boundary-layer depth and so the surface sediment grains are exposed to hydrodynamic drag (F_D) and lift (F_L) forces that are $\mathcal{O}(\rho u_c^2 d^2)$. For a hydraulically smooth bedform, k_s is significantly smaller than the boundary-layer depth, allowing a laminar viscous sublayer to be established in the fluid immediately above the bed surface, within which viscous stresses act to significantly reduce the drag and lift forces acting on exposed surface sediment. That is, when k_s is comparable to, or smaller than the viscous-sublayer thickness δ_v, the surface sediment grains are exposed to velocities $\mathcal{O}(u_c k_s / \delta_v)$ (Wiberg and Smith, 1987) and so the drag and lift forces are $\mathcal{O}(\rho \varepsilon^2 u_c^4 d^4 / \nu^2)$, where $\varepsilon = k_s / d$ (where $0 < \varepsilon \leq 1$) (Krishnan and Leighton, 1995). The data reported by White (1970) (and other studies e.g. Brownlie (1982) and Lamb et al. (2008)) suggests that hydraulically smooth bedforms correspond to $Re_* \leq 5$ (typically, $d \lesssim 200\text{-}300\,\mu$m for natural sediments), in which case the critical Shields parameter is found to increase significantly with decreasing Re_*, due to the damping effect of the viscous sublayer (White, 1970). Conversely, when $Re_* > 10$, this viscous damping effect ceases to be evident and the critical Shields parameter is found to vary very little with Re_* [and is constant for $Re_* > 5$ (i.e. $d \geq 3\,$mm for natural sediments)] (Lamb et al., 2008). Despite general scatter, a similar pattern can be identified in the data reported in Figure 3.14(a). That is, for $d / \delta_v \leq 5$ ($Re_p \leq 7$) the measured values of θ_{c0} increase monotonically with decreasing d / δ_v, whereas for $d / \delta_v > 5$, $\theta_{c0} \approx 0.05$ (and near-constant), which suggests that, here, the viscous damping effect becomes significant for $d / \delta_v \leq 5$ (which corresponds to $d \lesssim 350\,\mu$m). Also note that in Figure 3.14, $\theta_{c0} \approx 0.4$ for the finest sediment, whereas $\theta_{c0} \approx 0.05$ for the larger grain sizes.

This factor of eight difference is the same as that reported in White (1970) for comparable grain sizes. For the experiments considered, a rough bedform corresponds to when the roughness length scale is comparable to, or larger than the viscous sublayer.

Furthermore, under threshold conditions with $\beta = 0$, incipient grain motion occurs when the drag force F_D overcomes the net frictional force $\lambda_f(W - F_L)$ acting on the grain, where λ_f denotes the friction coefficient between grains and $W = \pi(s - 1)\rho g d^3/6$ is the grain's submerged weight. Hence, for hydraulically rough bedforms the above condition reduces to $\theta_{c0} \sim \mathcal{O}(1)$ (and constant). However, when $k_s/\delta_v \lesssim 1$ and the bedform is hydraulically smooth, the corresponding condition gives $\theta_{c0} \sim \nu/\varepsilon[(s - 1)gd^3]^{1/2}$, so that θ_{c0} is dependent on the grain size and density. Moreover, for sediment grains for which Stokes' Law $w_s = 2(s - 1)gd^2/9\nu$, is valid, this condition reduces to $\theta_c \sim Re_p^{-1/2}$ (Eames and Dalziel, 2000). With limited points for hydraulically smooth bedforms, it is difficult to determine the exponent $m = 1/2$ in the $\theta_{c0} \sim Re_p^{-m}$ scaling. Nonetheless, the measured values of θ_{c0} for $Re_p \leq 7$ show reasonable agreement with $\theta_{c0} \sim Re_p^{-1/2}$, which is shown in Figure 3.14(b) by the slope of the solid-line triangle. Finally, note that, for fine-grained sediments cohesive forces can become dominant in comparison with the grain weight. However, this situation occurs only for very fine particles with $d \lesssim 30\,\mu m$ considerably smaller than the grain sizes used here (Phillips, 1980). Hence, here, the effects of cohesion have been ignored throughout.

It is pertinent to note that the transition zone (i.e. the characteristic dip in the traditional Shields diagram (see Figure 1.1)) was not observed in Figure 3.14(b). The dip is attributed to the fluctuating lift forces acting on the particles (Zanke, 2003). The particle sizes in the transitional region are comparable, or bigger than the viscous sublayer $(d \approx \delta_v)$, that is the upper surface of the grain protrudes out of δ_v, exposing itself to high fluctuating velocity components (in turbulent flow). The pressure differences in the vertical direction, between the lower (where it lies in δ_v) and the upper surface of the grain resulted lift forces. Note that for hydraulically smooth and rough bedforms, the turbulence-induced pressure differences is negligible.

Some scatter was observed in the data, believed due to be the subjectivity of the threshold sediment motion determination. Recall that the critical conditions for incipient sediment motion was defined as when intermittent sediment motions were observed at each corner of the sediment bed. In an attempt to minimise the error, each data point represents an average taken from a number of repeats of the same nominally identical experiments, with the sediment layer reformed between each experiment.
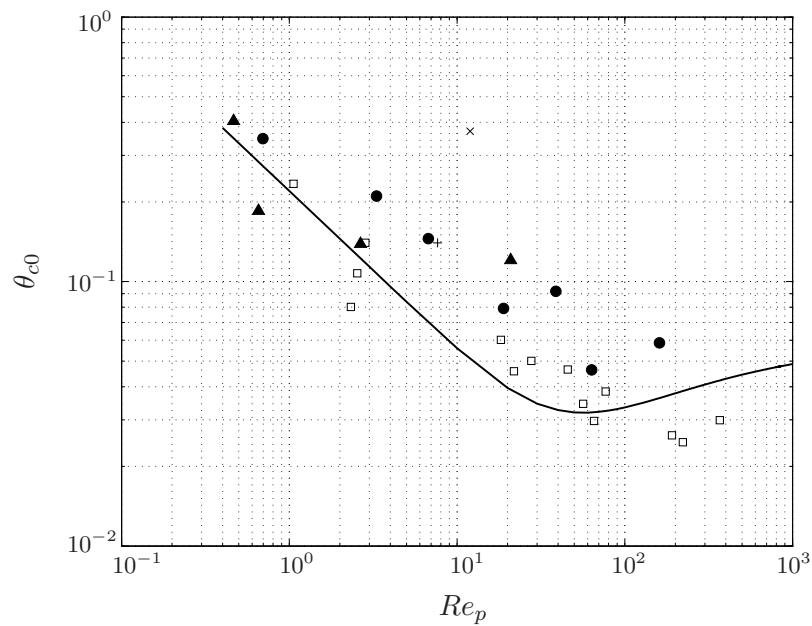
Figure 3.15: The measured critical Shields parameter θ_c plotted together with data extracted from Lyn (1995), Bellinsky (2005) and Liu (2006). The different data point styles represent different sediment types, specifically: ballotini ($\bullet$), Diakon ($\blacktriangle$), Bellinsky ($\square$), Lyn($+$) and Liu($\times$). The solid line is the Shields curve calculated using the relationship from Brownlie (1981).

It should be noted that characterizing using zero-mean turbulence generated from the experimental procedure described above is expected to overestimate the critical Shields parameter obtained from the Shields diagram (see Figure 1.1). Such estimates are typically based on thresholds for incipient sediment motion in a steady turbulent channel flow, in which case the mean velocity profile is well understood and the u_{*c} can be estimated using standard formulae e.g., $u_{*c} = \sqrt{gH\beta}$, where H is the hydraulic depth. For qualitative comparison, the values of θ_c obtained here were compared with the Shields profile. The measured θ_{c0} also is quantitatively and qualitatively compared with the previous studies of Lyn (1995), Bellinsky et al. (2005) and Liu et al. (2006). The comparison is shown in Figure 3.15. The discussion will start with the comparison of measured θ_c obtained in this study with the modified Shields curve which is calculated using the relationship developed by Brownlie (1981), $\theta_c = 0.22R_p^{-0.6} + 0.06\exp(-17.77R_p^{-0.6})$, with $R_p = \sqrt{(\gamma - 1)gd^3}/\nu$. The term R_p depends only on the physical characteristics, permitting a qualitative comparison with the Shields curve. Note that the data reported in this study corresponds to zero-mean turbulence, whereas the Shields curve is obtained from steady turbulent channel flow. Hence, the comparison is primarily qualitative. The range of Re_p available in this study was limited (i.e. $0.5 - 163$), from the hydraulically smooth flow ($Re_p \leq 7$) to the hydraulically rough flow ($Re_p > 7$). Over this range, the θ_c data were qualitatively consistent with the traditional Shields curve (see Figure 3.15).

Although the definition of critical velocity u_c used here differed from the previous OGT studies of Lyn (1995), Bellinsky et al. (2005) and Liu et al. (2006), all the data from these studies were plotted for comparison. Figure 3.15 shows these data compared with data reported here. The range of dimensionless particle sizes used in Bellinsky et al. (2005)'s are all within the smooth, transitional and rough regimes, $1 \leqslant Re_p \leqslant 370$. The values of θ_c reached an essentially constant value for $Re_p > 15$, of $0.03 < \theta_c < 0.05$. It has been noted that for $Re_p > 50$, the data of Bellinsky et al. (2005) reached a constant $\theta_c \approx 0.03$ value, much lower than the Shields curve and the data reported here. A linear regression analysis applied to the data of Bellinsky was conducted utilising the $\theta_c = \iota Re_p^{-n_{og}}$ relationship, and empirical coefficients ι and n_{og} were found to be 0.16 and 0.342, respectively. These coefficients are comparable to the ones measured in this study, particularly the slope n_{og} (which is 0.316 for this study and 0.342 for Bellinsky). A detailed analysis of the bed roughness effect was performed on Bellinsky's data by plotting θ_c against d/δ_v and is shown in Figure 3.16. The data from Bellinsky et al. (2005) was extracted and was re-calculated in terms of d/δ_v, where $\delta_v = \nu/u_c$ was employed. Figure 3.16 shows that
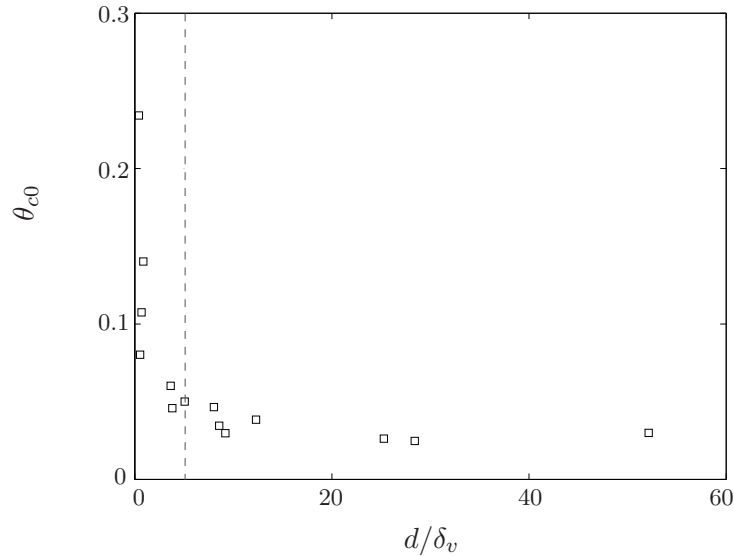
Figure 3.16: Measured values of critical Shields parameter θ_c obtained from Bellinsky(2005) against (a) d/δ_v. Data from Bellinsky(2005) was extracted and re-calculated for d/δ_v values. The dashed line corresponds to the $d/\delta_v = 5$, value taken as the upper limit of hydraulically smooth.

the hydraulically smooth region limit was also obtained at $d/\delta_v \leq 5$, comparable to the current study. Note that the data obtained in Bellinsky et al. (2005) also did not show any significant 'dip' in the transition region (as shown in the Shields diagram).

Quantitatively, Bellinksy's data have lower values than those measured in this study for all the Re_p ranges. This is because Bellinsky defined u_c from the homogeneous region, and ignored the amplification of u in the surface-influenced layer resulting in an underestimate of θ_c. The differences in characterizing the threshold of sediment motion (where Bellinsky et al. (2005) offered no detail) may also be a contributing factor. Although several differences exist in the method of data analysis employed in this study in comparison with Bellinsky et al. (2005), the important point to note is that both studies produced a similar qualitative trend in the data for θ_{c0}. The work of Lyn (1995) and Liu et al. (2006) only reported one type of sediment and size, and also were included in Figure 3.15. The data point obtained by Lyn (1995) falls in the range of measured θ_c (in this study), where as the point in Liu et al. (2006) suggests the value is overestimated. The reason for the overestimation could not be ascertained.

Figure 3.15 suggests that estimates for θ_c obtained using zero-mean turbulence, at

least for a horizontal bed, produced a similar profile with the established Shields diagram (based on flows with a mean flow). This supports the concept that the fluctuating velocity components control the critical criteria for sediment motion and so should be accounted for when estimating the bed-load sediment transport.

3.3.2 Measurements of critical criteria; for sloping beds

We now consider how the measured values of θ_c were affected by systematic increases in bed slope, relative to $\beta = 0$. Recall that four angles of bed slope were considered and henceforth θ_c for each β is denoted as $\theta_{c\beta}$. The data are compared with a force-balance model, based on the required condition for incipient sediment motion on a sloping bed (Wiberg and Smith, 1987; Chiew and Parker, 1994). Previous bed-slope studies have used this approach, but focussed exclusively on hydraulically rough bedforms with $d \geq 500\mu$m (Chiew and Parker, 1994; Dey and Debnath, 2000; Lamb et al., 2008). However, for the sediment types used here, the damping effect of the viscous sublayer also needs to be considered, and so the force-balance model is rederived to account separately for hydraulically rough and hydraulically smooth bedforms.

Consider a planar bedform consisting of cohesionless, monodisperse sediment, which is inclined with bed slope $\beta = \tan \alpha$ (where $0° \leq \alpha \leq \varphi$). Using the notation introduced above, incipient motion of a surface sediment grain (in the down-slope direction) occurs when the force balance

$$F_D + W \sin \alpha = \lambda_f (W \cos \alpha - F_L), \tag{3.6}$$

is satisfied. The symbol C_f is the friction coefficient. Note that, in the absence of flow ($F_D = 0$, $F_L = 0$) incipient motion occurs only when the bed slope is at the repose limit, $\beta_r = \tan \varphi$. Applying these conditions in Equation (3.6) gives

$$\lambda_f = \tan \varphi \equiv \beta_r. \tag{3.7}$$

Assuming that the sediment grains are spherical, the forces W can be written as

$$W = \pi(s - 1)\rho g d^3/6, \tag{3.8}$$

and the drag F_D and lift forces F_L acting on the particles are presented as

$$(F_D, F_L) = \begin{cases} \pi(C_D, C_L)\rho\varepsilon^2 u_c^4 d^4/2\nu^2 & \text{(smooth beds),} & \text{(3.9a)} \\[3mm] \pi(C_D', C_L')\rho u_c^2 d^2/2 & \text{(rough beds),} & \text{(3.9b)} \end{cases}$$

where C_D, C_D', C_L and C_L' are the drag and lift coefficients, which in general are functions of Re_p and Re_M. Substituting Equations (3.8) and (3.9) into Equation (3.6) gives (after some manipulation),

$$\theta_c = \begin{cases} \left[\dfrac{\mathcal{K}\nu^2}{\varepsilon^2(s-1)gd^3} \left(1 - \dfrac{\beta}{\beta_r}\right)\cos\alpha \right]^{1/2} & \text{(smooth beds),} & \text{(3.10a)} \\[5mm] \mathcal{K}'\left(1 - \dfrac{\beta}{\beta_r}\right)\cos\alpha & \text{(rough beds),} & \text{(3.10b)} \end{cases}$$

where the coefficients $\mathcal{K}$ and $\mathcal{K}'$ are given by

$$\mathcal{K} = \frac{\beta_r}{3\left(C_D + \beta_r C_L\right)}, \tag{3.11a}$$

$$\mathcal{K}' = \frac{\beta_r}{3\left(C_D' + \beta_r C_L'\right)}. \tag{3.11b}$$

For a horizontal bed ($\alpha = 0°, \beta = 0$), Equation (3.10) reduces to

$$\theta_{c0} = \begin{cases} \left[\dfrac{\mathcal{K}_0\nu^2}{\varepsilon^2(s-1)gd^3} \right]^{1/2} & \text{(smooth beds),} & \text{(3.12a)} \\[5mm] \mathcal{K}_0' & \text{(rough beds),} & \text{(3.12b)} \end{cases}$$

where $\mathcal{K}_0$ and $\mathcal{K}_0'$ are henceforth used to denote the respective values of $\mathcal{K}$ and $\mathcal{K}'$ when $\beta = 0$. Then, noting that $\theta_{c\beta}/\theta_{c0} = u_{c\beta}^2/u_{c0}^2$, Equations (3.10) and (3.12) can be combined to give

$$\frac{u_{c\beta}}{u_{c0}} = \begin{cases} \left[\dfrac{\mathcal{K}}{\mathcal{K}_0}\left(1 - \dfrac{\beta}{\beta_r}\right)\cos\alpha \right]^{1/4} & \text{(smooth beds),} & \text{(3.13a)} \\[5mm] \left[\dfrac{\mathcal{K}'}{\mathcal{K}_0'}\left(1 - \dfrac{\beta}{\beta_r}\right)\cos\alpha \right]^{1/2} & \text{(rough beds),} & \text{(3.13b)} \end{cases}$$

where $u_{c\beta}$ denotes the value of u_c at each β. The expression for rough beds in Equation (3.13b) has been applied in a number of previous studies (Whitehouse and Hardisty, 1988; Chiew and Parker, 1994; Dey et al., 1999). Note that in these aforementioned studies, the critical velocity u_c is estimated using a standard empirical formulation based on the streamwise time-averaged mean velocity. Both Equations (3.13) predict that the bedform becomes more mobile as the bed slope is increased, with $u_{c\beta}/u_{c0} \to 0$ as $\beta/\beta_r \to 1$ (and $\alpha/\varphi \to 1$). Comparing both Equations (3.13a) and (3.13b) shows that the effective bed roughness can have a significant effect. That is, the damping due to the viscous sublayer acts as a stabilizing influence for smooth beds, thereby reducing the rate at which the bed mobility increases with bed slope.

In general, one would expect that the coefficients $\mathcal{K}/\mathcal{K}_0$ and $\mathcal{K}'/\mathcal{K}'_0$ to be functions of the particle characteristics (Re_p) and the fluid flow (Re_M). That is, the flow characteristics near-bed determines C_D and C_L, subsequently affecting the coefficients $\mathcal{K}/\mathcal{K}_0$ and $\mathcal{K}'/\mathcal{K}'_0$ through Equations (3.11). However, the approximation $\mathcal{K}'/\mathcal{K}'_0 = 1$ has been used previously by other researchers in applying Equation (3.13b), which implies that $\mathcal{K}' = \mathcal{K}'(Re_p)$ and is unaffected by changes to the required critical flow conditions that arise when the bed slope is altered (between $0 \leq \beta \leq \beta_r$). The ratio $\mathcal{K}'/\mathcal{K}'_0 = 1$ has been used previously and is consistent with the experimental data for hydraulically rough bedforms (Whitehouse and Hardisty, 1988; Chiew and Parker, 1994; Dey and Debnath, 2000). In particular, Chiew and Parker (1994), using natural sediments with d between 500 - 2700 μm and streamwise bed slopes in the range $0 \leq \beta/\beta_r \leq 0.85$, found good agreement with measurements of u_{*c}/u_{*c0} obtained from a steady closed-conduit flow, where the critical bed shear velocity (u_{*c}) was estimated using a standard empirical formulation based on the streamwise time-averaged mean flow velocity.

Figure 3.17 shows the measured $u_{c\beta}/u_{c0}$, plotted against β/β_r, with each sediment type indicated by a different data symbol (see caption). Equations (3.13) with $\mathcal{K}/\mathcal{K}_0 = 1$ and $\mathcal{K}'/\mathcal{K}'_0 = 1$ assumed, have been included for comparison and are shown by the solid line (rough bedforms) and broken line (smooth bedforms), respectively. Each line was computed using $\beta_r = \tan\varphi$ with $\varphi = 30°$, which is the average value of the eleven repose angles reported in Table 3.1. To prevent saturation, error bars have been included for particle D (which are largely representative) and particle B (which exhibit the largest degree of variability). The tabulated data presented in Figure 3.17 is also included in Appendix A, together with the corresponding values of d/δ_v. It is worth highlighting here that, for each sediment type, the relative roughness d/δ_v decreases with increasing bed
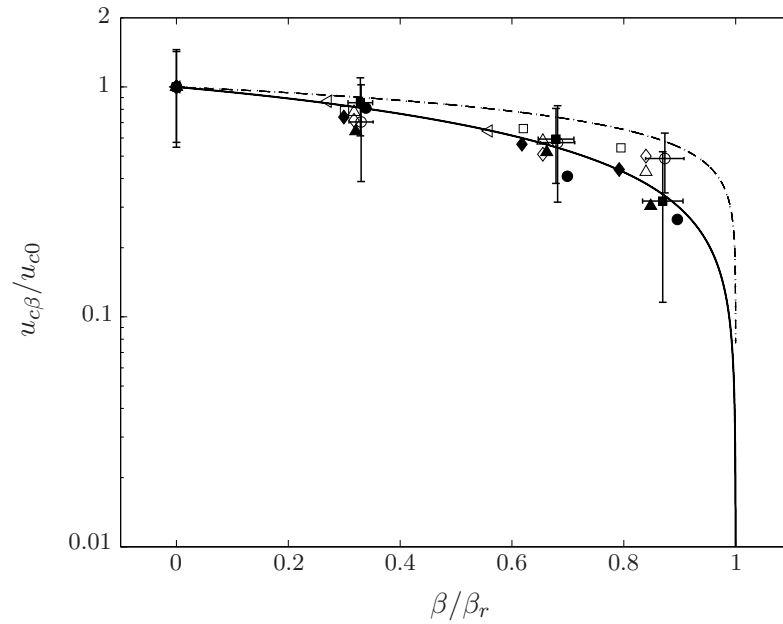
Figure 3.17: Measured values of $u_{c\beta}/u_{c0}$ against bed slope β/β_r for both hydraulically rough and smooth bedforms, presented as filled and open legends, respectively. Particle A ($\bullet$), Particle B ($\blacksquare$), Particle C ($\blacktriangle$) and particle H ($\blacklozenge$) are rough bedforms where as Particle D ($\circ$), Particle E ($\square$), Particle F ($\triangle$), Particle G ($\diamond$), and Particle I ($\triangleleft$) are categorised in smooth bedforms. Solid and dashed lines represents the prediction for hydraulically rough and smooth boundaries, respectively.

slope.

The values of $u_{c\beta}/u_{c0}$ are plotted according to their respective bedform type i.e. smooth or rough bedforms in Figure 3.17. Note that although Figure 3.14 determines the limit of hydraulically smooth bedforms to be at $d \leq 200\,\mu\text{m}$, as bed slope increases ($\beta > 0$), for particle D ($d \approx 374\,\mu\text{m}$), the relative roughness d/δ_v shifted to a smooth bedform. For this analysis, rough bedforms are defined by particles with $d > 374\,\mu\text{m}$ and below this limit a smooth bedform is said to exist. The hydraulically rough bedform is discussed first. Recall that the values of θ_{c0} reported in Figure 3.14 suggest that, for the sediment types used here, the transition to rough bedform behaviour (where the viscous damping effect is insignificant) corresponds to $d/\delta_v > 5$. Over the range of bed slopes considered here ($0 \leq \beta/\beta_r \leq 0.9$), the data for sediments in the hydraulically rough region satisfy $4.2 \leq d/\delta_v \leq 33.3$ and the corresponding values of $u_{c\beta}/u_{c0}$ are well described by Equation (3.13b). The critical shear velocity steadily decreases as the bed slope increases. These values of $u_{c\beta}/u_{c0}$ appear to be independent of grain size (within the level of general scatter), which supports the validity of the $\mathcal{K}'/\mathcal{K}'_0 = 1$ assumption (suggested in previous studies). The measured $\theta_{c\beta}$ values measured are all observed to be either falling on or slightly under the predicted line. It is believed that besides the effect of additional weight components, critical sediment motion on an angled bed is misrepresented as the motion due to particle agitation.

It has been shown that the hydraulically smooth particles all satisfy $0.8 \leq d/\delta_v \leq 7.8$, within the limit of hydraulically smooth region. As illustrated in Figure 3.17, the data did not fall on the prediction line (of Equation (3.13a)) and is better described by the rough region profile until $\beta/\beta_r \approx 0.75$. This is believed to be to the fact that for smaller particles, the energy of eddies impinging on the bed surface disrupts the viscous sublayer and exposes the particles to energetic fluid, lowering θ_c. However, as the bed slope increased to $\beta/\beta_r > 0.75$, the corresponding effective bed roughness is sufficient to alter the behaviour of the bedform from hydraulically rough to hydraulically smooth. The low flow strength increases the viscous sublayer thickness and acts as protection layer for the surface particles. Note that although the measured values of θ_c generally followed the prediction lines, the level of scatter is quite apparent in Figure 3.17 since the obtained critical shear stress may vary significantly because it depends on what degree of bed mobility is set as the threshold condition (Shvidchenko and Pander, 2000).

3.4 Summary

The experimental analysis in the near-bed region confirmed that quasi-isotropic homogeneous turbulence suffers inhomogeneity due to the interaction with the sediment bed. The inhomogeneous region (i.e. the surface-influenced layer) was observed up to $1.5l_\infty$ above the bed surface. The r.m.s. horizontal velocity was amplified and reached a peak value at $\xi \approx 0.3$ at the expense of decreasing r.m.s. vertical velocity for $Re_l > 110$. This inter-component energy transfer indicates that a coherent structure of splat/antisplat phenomena occur in the process. For the flow with $Re_l \leq 100$, no amplification of r.m.s. horizontal velocity and non-monotonic decrease of r.m.s. vertical velocity were observed within the surface-influenced layer, suggesting in changes of the turbulence structure and the velocity profile deviates from the standard profile of Hunt and Graham (1978). For all the sediment types used here, the critical conditions for sediment motion were observed for $Re_l > 110$ (using $S = 8$ cm).

The critical Shields parameter 'θ_c' values were estimated using the near-wall peak value of the r.m.s. horizontal velocity, measured at the point at $\xi \approx 0.3 - 0.4$ (equivalent to $\mathcal{Z}/M \approx 0.1$) above the bed surface. The critical Shields parameter θ_c on a horizontal bed is a function of Re_p. The measured values of θ_{c0} on a horizontal bed case ($\beta = 0$) were compared with traditional measurements of the critical Shields parameter obtained in turbulent channel flows [by applying the expressions obtained in Brownlie (1982)]. Although they were notably different in magnitude and no 'dip' in the transitional region was observed (for the range of particles discussed here), a similar qualitative trend was identified. In particular, the values of θ_{c0} reported here suggest that the threshold for hydraulically smooth bed forms is $d/\delta_v \approx 5$ (which corresponds to $d \sim 350\mu$m). For $d/\delta_v \approx 5$, the measured values of θ_{c0} were observed to increase monotonically with decreasing d/δ_v. For $d/\delta_v > 5$, the effects of viscous damping cease to be evident, and so θ_{c0} was near constant. These observations are consistent with smooth-bedform threshold $Re_* \approx 10$ (corresponding to $d \approx 200 - 300 \ \mu$m) identified by previous studies (White, 1970). The measured θ_{c0} are also quantitatively and qualitatively compared with the profile obtained from Bellinsky et al. (2005) and a similar profile was obtained.

The data reported here also shows that bed slope plays an important role in the critical criteria for the onset of sediment motion. Estimation of the critical Shields parameter requires the bed slope to be accounted for, with the bed becoming more mobile with increasing bed slope due to the additional downslope gravitational force. The measured

values of θ_c obtained for bed slopes $0 \leq \beta/\beta_r \leq 0.9$ were compared with a simple force-balance model, based on the required condition for incipient grain motion on a sloping bed. The standard derivation of this model, corresponding to hydraulically rough bedforms, takes the form given in Equation (3.13b) (Chiew and Parker, 1994). Here, the model was extended to account for the case of hydraulically smooth beds. That is, for $k_s/\delta_v \leq 1$, the near-surface sediment grains are exposed to reduce drag and lift forces, which here are assumed $\mathcal{O}(\rho\varepsilon^2 u_c^4 d^4/\nu^2)$. In this case, the corresponding model takes the form given in Equation (3.13a). Comparing Equations (3.13a) and (3.13b) shows that the damping effect of the viscous sublayer acts as a stabilizing mechanism for smooth beds, reducing the rate at which the bed mobility increases with bed slope. The measured values of $u_{c\beta}/u_{c0} = (\theta_{c\beta}/\theta_{c0})^{1/2}$ were consistent with Equation (3.13), particularly for the hydraulically rough bedfroms. Particles in the hydraulically smooth bedforms however, have been shown to coincide with the hydraulically rough bedform prediction line, although the deviation to the smooth bedform starts to occur as the bed slope becomes close to the angle of repose. For lower $\beta/\beta_r \leq 0.75$, energetic eddies disrupt the viscous sublayer, exposing the adjacent near-surface sediment to increased hydrodynamic drag and lift forces, thereby reducing θ_c.

Chapter 4

Measurements of critical criteria for incipient sediment motion by vortex ring

An alternative approach to delineate how a complex, intermittent turbulent flow interacts with and moves sediment is to consider turbulence as an ensemble of elemental vortex structures in the form of vortex rings (Munro et al., 2009). The vortex ring is used here in a similar context with the oscillating-grid turbulence experiment, and is intended to represent an idealised model for the unsteady interaction between an isolated eddy and a sediment layer. The vortex ring represents one of the simplest vortex structures, which can be easily and consistently produced in the laboratory. One notable advantage of using the vortex ring is that conditions for incipient grain motion can be defined objectively, and determined with high degree of repeatability. Moreover, the dynamics of vortex-ring interaction with solid boundaries have been discussed from previous experimental studies and numerical simulations (Walker et al., 1987; Orlandi and Verzicco, 1993). Thus, using a vortex ring permits an analysis in isolation (in the absence of mean flow) of the sediment movement by individual vortices.

Munro et al. (2009) employed the vortex ring to characterise the flow condition giving rise to the incipient sediment motion, in particular, the horizontal bed $\beta = 0$ case. This section extends the study of Munro et al. (2009) by investigating the effect of bed slope. One of the aims in this section is to qualitatively compare the overall trend of the critical Shields parameter θ_c obtained by an idealised eddy i.e., vortex ring (VR) with the θ_c mea-

sured in the previous oscillating-grid (OG) experiments. One should bear in mind that the nature of both flows are different in that vortex ring is a steady laminar single eddy where as the oscillating-grid turbulence produces multiple random eddies interacting with each other throughout the whole distance from the grid to the sediment bed. Although the method of generating turbulence and the initial state of the turbulence structure is different, the sediment movement induced by both methods is similar. The energetic eddies stretched and increase the bed shear stress acting on the particles, entraining them out from their stationary position in a circular splash (Munro et al., 2009). Sediment trajectories under the influence of energetic turbulence produced by the OG were also observed in a circular splash. This will be extended further in the next chapter. The key difference between the flows is that the VR experiments generate one energetic eddy, whereas in OG experiments, multiple energetic eddies are seen to interact with the sediment bed.

4.1 Experiment arrangement

A sketch of the apparatus is shown in Figure 4.1. Each experiment was performed in an 80 litre acrylic tank containing water. The sediment types used were as described in Table 3.1. Each sediment layer was formed in a shallow tray at the base of the tank (see Figure 4.1), with the surface of the layer prepared by carefully drawing a straight-edged scraper across the top rim of the tray. This produce a flat, close-packed bed of consistent mean depth 0.5 cm. The bed slope was set by tilting the tray using a threaded depth gauge attached to one side of the tray, and a threaded nut was used to set the required angle α (as shown in Figure 4.1). To prevent the sediment bed from sliding on the smooth tray surface when tilted, the tray base was roughened by gluing to its surface a thin layer of Particle A ($d = 1087\,\mu\mathrm{m}$). The experiments were performed at a range of bed angles between $0° \leq \alpha \leq \varphi$. Recall that φ denotes the repose angle for a given sediment type. The corresponding bed slope is henceforth defined as $\beta = \tan\alpha$, and $\beta_r = \tan\varphi$ denotes the bed slope at the repose limit.

Each vortex ring was generated using a uniform cylindrical tube (internal diameter $D_0 = 4\,\mathrm{cm}$, length $40\,\mathrm{cm}$) clamped in position above the tank with the outlet submerged below the water's free-surface (see Figure 4.1). The tube inlet was sealed with an airtight fitting and connected to a cycle track pump by a length of hose. Actuation of the pump caused the air cavity inside the tube to expand, forcing a pre-determined volume of water from the tube outlet. As the fluid 'slug' exits the tube, the vortex sheet shed at
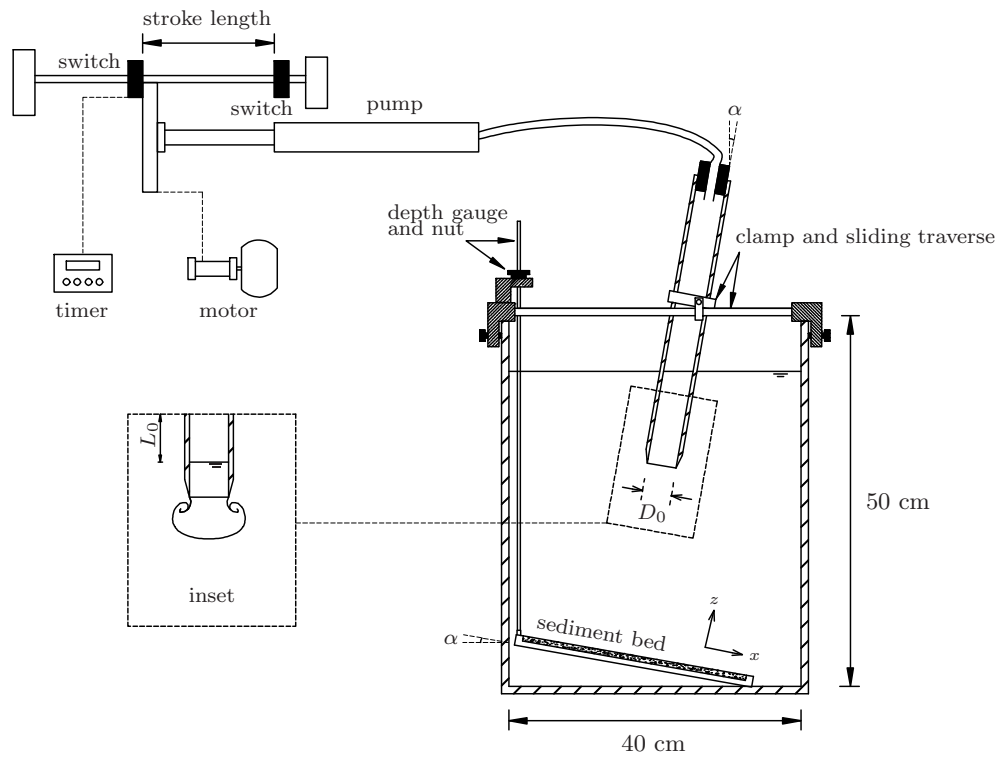
Figure 4.1: Sketch of vortex ring experiment setup. α denotes the angle of bed slope.

the lip of the outlet rolled up to form the vortex ring (see inset of Figure 4.1) (Saffman, 1975). Once fully formed each vortex ring propagated away from the outlet along the central symmetry axis of the tube, until interacting with the sediment layer. Attention was focussed on interactions in which the central propagation axis of the vortex ring was aligned to be perpendicular to the bed surface. This ensured that the qualitative characteristics of the ring flow field, during the interaction, were the same for each bed slope. Hence, an adjustable clamp and traverse mechanism was used to tilt and hold the tube at the corresponding angle α to the vertical (as shown in Figure 4.1).

Once fully formed, each vortex ring travelled a relatively short distance (approximately $5D_0 = 20\,\text{cm}$) before the ring structure and trajectory were noticeably affected by the presence of the sediment layer, which occurred when the core of the ring had reached a height of approximately $D_0/2$ above the bed surface (Munro et al., 2009). Over this short distance very little ambient, irrotational fluid is entrained within the ring structure [by diffusion] (Maxworthy, 1972; Saffman, 1975). Hence, prior to being affected by the presence of the sediment layer, the ring diameter (D_{vr}) and axial propagation speed (U_{vr}) were approximately constant.

The important characteristics of each vortex ring D_{vr} and U_{vr} were determined by the tube diameter, $D_0 = 4\,\text{cm}$, and the stroke length and stroke time of the pump (see Figure 4.1) (Munro et al., 2009). For the experiments described here, a fixed stroke length of $20\,\text{cm}$ was used throughout, which produced a fluid slug of length $L_0 = 9.5\,\text{cm}$ (i.e., $L_0/D_0 = 2.4$). The pump actuation rate was controlled by attaching the pump handle to a motor-driven spool by a length of nylon cord (see Figure 4.1). The pump stroke time was controlled by adjusting the rotation rate of the motor, and measured using a digital timer connected to two switches positioned to detect the start and end of the pump stroke (see Figure 4.1). With this system the ring diameter D_{vr} and, most importantly, the propagation speed U_{vr} were controlled by adjusting the pump stroke time (Munro and Dalziel, 2003; Munro et al., 2009).

For a given sediment type and bed slope 'β', the critical conditions for incipient motion were determined by repeating an experiment, each time systematically increasing the pump stroke time 'thereby decreasing U_{vr}' until grain motion was only just observed to occur, with any further increase in stroke time resulting in no motion. During this procedure the sediment layer was re-scraped and made flat prior to each repeat. Once the appropriate stroke time for critical conditions had been identified, the velocity field of the corresponding vortex ring was measured using PIV, the details of which are given below.

Note that, the PIV data captured the ring flow-field over the entire impact region, and at each stage during the interaction. To minimise the experimental errors associated with the incremental increase of the pump stroke time, the entire procedure described above was repeated several times (for each sediment type and bed slope) so that an average could be taken. The velocity data were also used to directly measure U_{vr} and D_{vr} for each vortex ring from the period before the ring's trajectory was affected by the sediment layer. The values of U_{vr} and D_{vr} reported here are the corresponding averages obtained from the repeated experiments, which had typical variability of $\pm 6\%$ and $\pm 4\%$, respectively. Over the range of critical impact conditions analysed in this article, the corresponding vortex ring Reynolds number, $Re_{vr} = UD_{vr}/\nu$, was varied between 450 and 3360 (where $0.8 \leq D_{vr}/D_0 \leq 1.2$).

4.1.1 The PIV measurements

The vortex ring velocity fields were obtained using two-dimensional planar PIV (as obtained in OG experiments). Small neutrally buoyant tracer particles were added to the water volume, and a narrow vertical light sheet of approximate thickness 2 mm was used to illuminate the seeding particles within the vertical midplane of the vortex ring trajectory. The motion of the tracer particles was recorded using a high-speed Dantec Nanosense MkIII digital camera (with 1280×1024 pixel resolution and frame rate set at $600\,\mathrm{Hz}$), positioned to view horizontally through the transparent sidewall of the tank (corresponding to the view shown in Figure 4.1). For the sloping beds, the camera was tilted on its side, at the angle α, so that the surface of the sediment layer appeared horizontal at the base of each image. The velocity fields were calculated directly from the captured images using the PIV algorithm within Digiflow (Dalziel). Images were recorded throughout the interaction period, but also during the period prior to impact so that U_{vr} and D_{vr} could be determined.

4.2 Results

For the experiments described in this section, the boundary layer induced by the interaction between the vortex ring and the sediment bed evolves spatially and with time. Moreover, the velocity profile within this region is not known, with previous studies being exclusive to a vortex ring interacting with solid (non-porous) surfaces, with axisymmetry assumed and for values of Re notably smaller than those considered here (Walker et al.,

1987). Hence, an analogous standard parameterisation was not possible and an alternative estimate for bed shear stress τ_b was required, based on the available fluid velocity data. The following approach was adopted.

Let $u_b(x,t)$ denote the horizontal fluid velocity component measured above the bed surface at height $z_b = 0.2\,\text{cm}$ [*i.e.*, $u_b(x,t) = u(x, z_b, t)$], which is as close to the bed surface at which reliable velocity measurements could be consistently obtained using the PIV setup described. Under critical impact conditions, sediment grains are brought into motion only by the peak value of the bed shear stress, which we expect to scale with $\rho \hat{u}_b^2$, where $\hat{u}_b$ denotes the maximum (or peak) value of $u_b(x,t)$ attained during the interaction period. During an interaction, the instantaneous peak values of $u_b(x,t)$ occurs directly below the vortex ring core, with the overall peak value '$\hat{u}_b$' attained when the ring core is at its closest point to the bed surface (Munro et al., 2009). Hence, in the present context, the Shields parameter for vortex ring experiment was defined as

$$\theta = \frac{\hat{u}_b^2}{(s-1)dg}. \tag{4.1}$$

The corresponding critical Shields parameter is given by

$$\theta_c = \frac{\hat{u}_{bc}^2}{(s-1)dg}, \tag{4.2}$$

where $\hat{u}_{bc}$ denotes the value of $\hat{u}_b$ measured under critical impact conditions. As already noted, for a steady turbulent channel flow τ_b is defined in terms of a velocity scale based on the time-averaged mean velocity. The approach adopted here uses a velocity scale characteristic of the peak variation in the time-dependent near-bed velocity during the interaction period.

4.2.1 On a horizontal bed case

The case of a horizontal bed, $\beta = 0$, impacted by a VR is first examined, henceforth the critical Shields parameter is denoted as θ_{c0}. As already noted, the critical bed shear velocity, u_{*c}, and hence Re_*, was not measured. However, in the region below the ring core, the depth of the boundary layer established adjacent to the bed surface is expected to be approximately $D_{vr}/Re_{vr}^{1/2}$. Likewise, the inner viscous sublayer in this region will have the thickness of order $\delta_v = (D_{vr}/Re_{vr})$ (Munro et al., 2009). Hence, for the VR experiments reported here, θ_c is a function of Re_p and d/δ_v. For the experiments considered here,
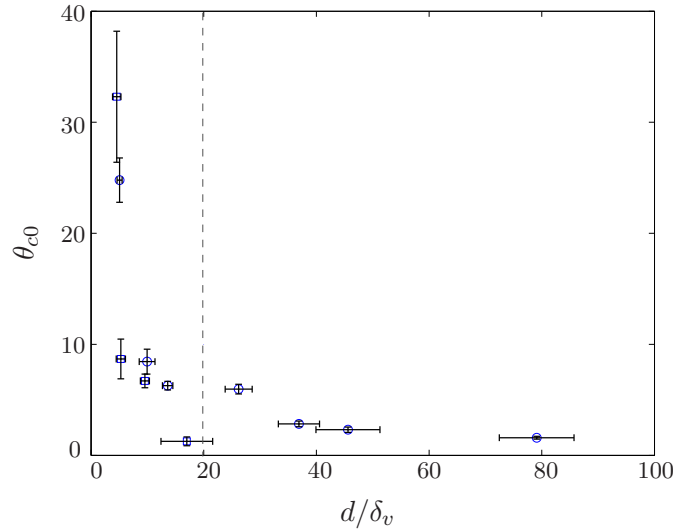
Figure 4.2: Measured values of the critical Shields parameter θ_c against (a) d/δ_v and (b) Re_p. Sediments are ballotini ($\circ$), Diakon ($\square$). The dashed line shows the limit of hydraulically smooth bedforms. Vertical error bars show the variability in the measured values of u_c whilst the horizontal error bars are from the w_s and d_{50} calculations.

a hydraulically rough bedform corresponds to when the roughness length-scale (k_s) is comparable to or larger than the boundary-layer depth and so the surface sediment grains are exposed to drag and lift forces that are $\mathcal{O}(\rho \hat{u}_{bc} d^2)$. In a hydraulically smooth bedform, a laminar viscous sublayer is established in the fluid immediately above the bed surface, within which viscous stresses act to significantly reduce the drag and lift forces acting on exposed surface sediment. For k_s comparable, or smaller than, δ_v, the surface sediment grains are exposed to drag and lift forces of $\mathcal{O}(\rho \varepsilon^2 \hat{u}_{bc} d^4/\nu^2)$, where $\hat{u}_{bc} = \mathcal{O}(1)$ has been used, and $\varepsilon = k_s/d_p$ (where $0 < \varepsilon \leq 1$). Figure 4.2 show the values of θ_{c0} plotted against d/δ_v for each sediment type. Data suggests that for $d/\delta_v \leq 20$ ($Re_p \leq 20$), the measured values of θ_{c0} increase monotonically and reached near-constant value when $d/\delta_v > 20$ ($Re_p > 20$). Thus, the limit of hydraulically smooth bedforms, in these VR experiments corresponds to $Re_p \leq 20$ (which corresponds to $d \leq 350\,\mu$m), in agreement with White (1970) who found $d \leq 200 - 300\,\mu$m for natural sediments. Above this limit are the rough bedforms. Figure 4.3 shows the critical Shields parameter obtained from turbulence produced in the OG and VR experiments against dimensionless particle Reynolds number Re_p. Measured θ_c also are plotted together with the Shields curve calculated using the Brownlie (1981) expression. Separate data symbols have been used to differentiate between
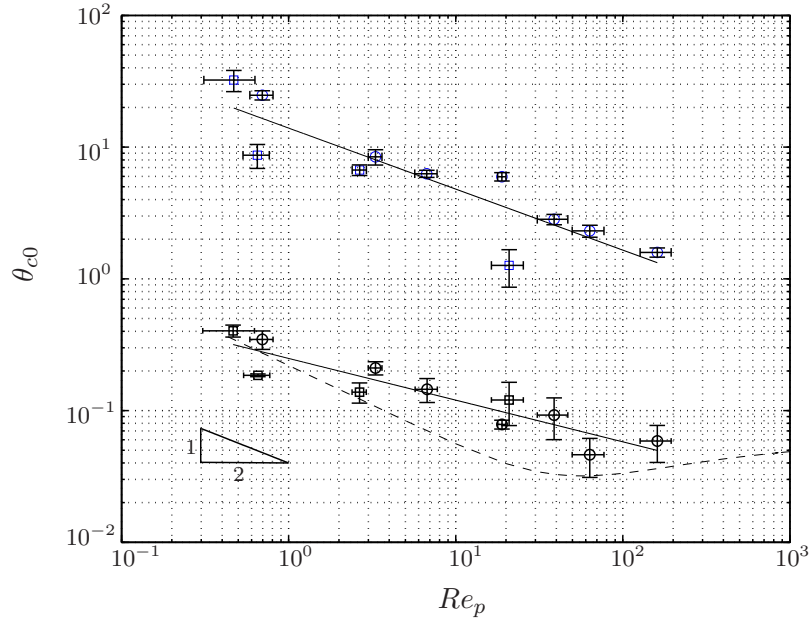
Figure 4.3: Critical Shields parameter obtained using OGT represented here with ballotini (∘), Diakon (□) and from the vortex ring experiments with (data points are blue coloured) ballotini (∘) and Diakon (□). Vertical error bars plotted for the vortex ring data are the measured variability of $\hat{u}_{bc}$ and horizontal bars are the errors associated with d_{50} and w_s. The triangle-solid line shows the theoretical curve $\theta_c \sim Re_p^{-1/2}$. The solid line represents the fit analysis for each profile and the dashed line is the Shields curve calculated using Brownlie (1981).

θ_{c0} obtained in VR and OG, respectively. The error bars for θ_{c0} and Re_p obtained from the VR experiments are based on the typical variability of d, $\hat{u}_{bc}$, w_s and U_{vr}. Attention is firstly focused on the θ_{c0} profile obtained from the VR experiments. The θ_{c0} reported in Figure 4.3 are two orders of magnitude larger than the traditional Shields curve and the profile obtained from the OG experiments. Therefore, a direct quantitative comparison with the values obtained using steady turbulent channel flows is precluded. However, a number of qualitative consistencies can be identified. For the hydraulically smooth region where $Re_p \lesssim 20$, the measured values of θ_{c0} increase monotonically with decreasing Re_p, where as for $Re_p > 20$, θ_c reaches a near-constant value at $\theta_{c0} \approx 2$. Also note that in Figure 4.3, $\theta_{c0} \approx 11$ for the finest sediment, whereas $\theta_{c0} \approx 2$ for the larger grain sizes. This factor of five difference is the same as that reported in White (1970) for comparable grain sizes.

In addition, the measured θ_{c0} in the hydraulically smooth bedforms was also compared to the reduced incipient grain motion condition of $\theta_{c0} \sim Re_p^{-1/2}$, where it is assumed that the terminal settling velocity for an isolated grain is given by $w_s = (s-1)gd^2/18\nu$ (Batchelor, 1967). The VR data in Figure 4.3 again displays consistency with this description. In particular, the measured values of θ_{c0} for $Re_p \leq 10$ show reasonable agreement with $\theta_{c0} \sim Re_p^{-1/2}$, which is shown in Figure 4.3 by the slope of the solid-line triangle. Note that as the sediment sizes used here are $d > 30\,\mu$m (the limit where cohesive forces becomes dominant), the effects of cohesion have been ignored throughout.

The comparison of the θ_{c0} profile between the VR and the OG experiments is now presented. Recall that the θ_c profile obtained by OG used u_c as the peak value of r.m.s. horizontal velocity at $z_c \approx 0.5$ cm above the bed surface. As stated above, the θ_{c0} obtained by VR are two orders of magnitude larger than the Shields curve and the θ_c obtained by OG. This is due to the differences in the velocity scale used in obtaining each θ_c. In the VR experiments, the absolute peak velocity at near bed was used, and of course will give essentially higher θ_{c0} values than when calculated using r.m.s. velocity (for OG experiments). Despite the general scatter, there is a qualitative resemblance in the profiles of the data obtained by both VR and OG in Figure 4.3. Notice that θ_{c0} is steadily decreasing as Re_p increases without any 'dip' in the transition between the smooth to the rough region. The Shields curve is plotted together with the θ_{c0} measured in both OG and VR experiments to give a description of the θ_c profile obtained in an open channel flow. The data suggests that the θ_c profiles captured by both methods are qualitatively comparable with the traditional Shields diagram.

An empirical computation of $\theta_{c0} = \iota_{vr} Re_p^{-n_{vr}}$ (similar to the one previously adopted for the OG data) was carried out and values of the coefficients ι_{vr} and n_{vr} were found to be 13.953 and 0.463, respectively. Comparing the coefficients ι and ι_{vr} offers no physical link as the flows and experimental setup for both methods were different. However, the data in Figure 4.3 shows that slope of $\theta_{c0} \sim Re_p$ relation in the data obtained from vortex ring experiments $n_{vr} = 0.463$ is slightly higher than that determined from the result of the OG experiments ($n_{og} = 0.316$). Due to the steady and laminar propagation of a VR, n_{vr} suggests that for critical conditions for incipient sediment motion, the rate of critical energy changes is higher for one idealised large scale eddy and is more influential on sediment motion than random intermittent eddies. The conserved energy available in the vortex ring creates higher bed shear stress, reducing the θ_c as the sediment size gets larger ($Re_p \to \infty$). In other word, for a specific sediment type on a fixed bed slope, the decreasing rate of θ_c when the sediment size is changed is more for a single idealised eddy than the random intermittent eddies.

4.2.2 On a sloping bed

The measured values of $\theta_{c\beta}$, which were affected by systematic increases in bed slope, relative to $\beta = 0$ is now presented. The data are also compared with the force-balance model described in Equation (3.13b) for hydraulically rough bed forms and Equation (3.13a) for hydraulically smooth bed forms. Figure 4.4 shows the measured $u_{c\beta}/u_{c0}$ obtained from both VR and OG experiments, plotted according to bedforms, i.e. the hydraulically rough in Figure 4.4(a) and hydraulically smooth in Figure 4.4(b). Each sediment type was indicated by a different data symbol, and each experiment setup was differentiate by a different colour (see caption). For each curve, $\beta_r = \tan\varphi$, was calculated using $\varphi = 30°$, corresponding to the average value of the eleven repose angles reported in Table 3.1. To prevent data saturation, error bars have been included for Particle A (which are largely representative) and Particle H (which exhibit the largest degree of variability) for VR experiments. For OG experiments, errors associated with Particle B and Particle D were shown. Data obtained by VR will be discussed first. The values of $u_{c\beta}/u_{c0}$ shown in Figure 4.4 are well described by Equation (3.13), either falling on, or in, the 'transition' region between the two predicted trends. Furthermore, recall that the transition to smooth-bed behaviour (where the effects of viscous damping are dominant) corresponds to $d/\delta_v \leq 20$. This property is further supported by Figure 4.4.
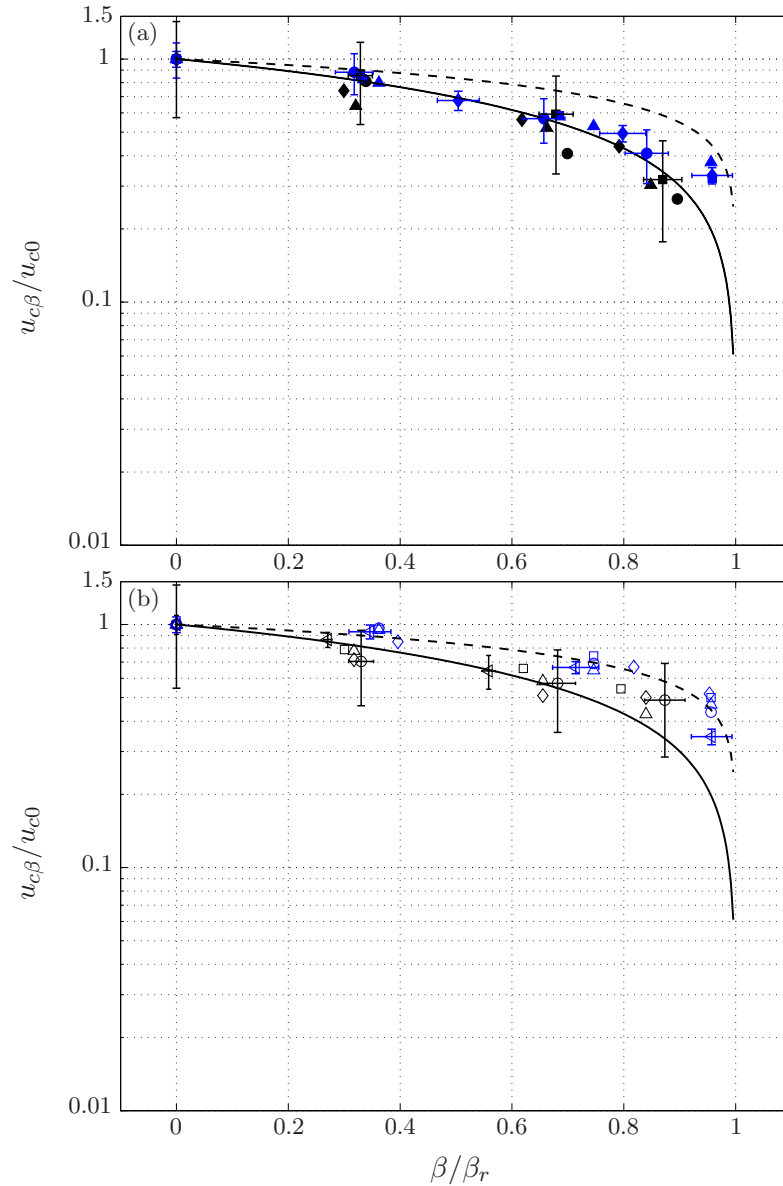
Figure 4.4: Measured values of $u_{c\beta}/u_{c0}$ against bed slope β/β_r for (a) hydraulically rough and (b) smooth bedforms. Black and blue data points represent the values obtained from grid turbulence and vortex ring experiments, respectively. Corresponding solid curves are the theoretical prediction. In (a), a filled data point represents Particle A ($\circ$), Particle B ($\square$), Particle C ($\triangle$) and Particle H ($\diamond$), whereas in (b), an open data point represents Particle D ($\circ$), Particle E ($\square$), Particle F ($\triangle$), Particle G ($\diamond$) and Particle I ($\triangleleft$).

Consider first the data for hydraulically smooth bedforms shown in Figure 4.4(b). Over the range of bed slopes considered here ($0 \leq \beta/\beta_r \leq 0.95$), the data for these sediment types satisfy $1.47 \leq d/\delta_v \leq 26.2$, and the corresponding values of $\hat{u}_{bc}/\hat{u}_{bc0}$ shown in Figure 4.4(b) are well described by the trend predicted in Equation (3.13a). Moreover, these values of $\hat{u}_{bc}/\hat{u}_{bc0}$ appear to be independent of grain size within the level of general scatter, which supports the validity of the $\mathcal{K}/\mathcal{K}_0 = 1$ assumption (suggested by previous studies). Now consider the data for the larger sediment types, which are shown in Figure 4.4(a). The data for Particle A, B and C all satisfy $13.2 \leq d/\delta_v \leq 79.1$. Moreover, the measured values of $\hat{u}_{bc}/\hat{u}_{bc0}$ corresponding to $d/\delta_v \geq 20$ agree with the trend predicted by Equation (3.13b) (and with the $\mathcal{K}'/\mathcal{K}_0' = 1$ assumption). However, the values of $\hat{u}_{bc}/\hat{u}_{bc0}$ satisfying $d/\delta_v \leq 20$, either fall in the region between the two curves, or are better described by Equation (3.13a). As illustrated by Figure 4.4(a), this departure from Equation (3.13b) typically occurs when the bed slope has increased beyond $\beta/\beta_r \approx 0.85$. Hence, for these sediment types the data suggest that, as the bed slope approaches the repose limit, the corresponding decrease in effective bed roughness k_s/δ_v is sufficient to alter the behaviour of the bedform from hydraulically rough, to hydraulically smooth.

Note that, for Particle H (with $d = 751 \, \mu$m, indicated by blue filled $\diamond$), the data satisfy $9.76 \leq d/\delta_v \leq 17.0$ over the range of bed slopes considered here. The corresponding values of $\hat{u}_{bc}/\hat{u}_{bc0}$ either fall on the trend predicted by Equation (3.13b), or in the transition region between the two curves. The reason for this is not known. However, it is worth reiterating that these data exhibit, by far, the largest degree of uncertainty.

Comparison with the $u_{c\beta}/u_{c0}$ obtained by OG is now discussed. The data in Figure 4.4(a) shows that the measured $u_{c\beta}/u_{c0}$ by VR and OG within the hydraulically rough region agreed with the predicted trend quite well. Although at $\beta/\beta_r > 0.8$, the values of $u_{c\beta}/u_{c0}$ from the VR experiments departs from Equation (3.13b), it is thought this is due to the decreasing in effective bed roughness, altering the bedform behaviour from hydraulically rough to hydraulically smooth. The hydraulically smooth particles obtained in the VR experiments shows a decreasing $u_{c\beta}/u_{c0}$ with increasing bed slope, closely following the predicted profile, where as data obtained by OG were found to be slightly lower. It is also interesting to see in Figure 4.4(a) that for the hydraulically rough bedform, the OG data closely follows the prediction line and the VR data falls between the rough and smooth bedform prediction lines, near the angle of repose. Within the hydraulically smooth region as shown in Figure 4.4(b), however, the OG data departs from the theoretical curve but the VR data is in close agreement with Equation (3.13a). The reason for this is believed

to be that the difference of critical velocity employed by both methods in describing θ_c. Another reason that may contribute is the deviation in defining the critical conditions for incipient motion in both setups.

4.3 Summary

Although the measured values of θ_{c0} obtained by vortex ring were notably different in magnitude, a similar qualitative trend was identified with the critical Shields parameter values obtained in turbulent channel flows (Brownlie, 1981). In particular, the values of θ_{c0} reported here suggest that the threshold for hydraulically smooth bedforms to be $d/\delta_v \approx 20$ (which corresponds to $d \approx 350\mu\text{m}$). Below this threshold, the bed roughness (k_s) is comparable to (or smaller) than the viscous-sublayer thickness, and so viscous stresses act to significantly reduce the hydrodynamic drag and lift forces acting on the near-surface sediment grains. Consequently, for $d/\delta_v \leq 20$, the measured values of θ_{c0} were observed to increase monotonically with decreasing d/δ_v. For $d/\delta \geq 30$, the effects of viscous damping cease to be evident, and so θ_{c0} was near constant. These observations are consistent with smooth-bedform threshold $Re_* \approx 10$ (corresponding to $d \approx 200 - 300\,\mu\text{m}$) identified by previous studies (White, 1970). The measured values of $\hat{u}_{bc}/\hat{u}_{bc0}$ were consistent with Equations (3.13), either falling on, or in the region between the smooth-bed and rough-bed cases when $d/\delta_v \leq 20$ in agreement with the threshold identified for the θ_{c0} data.

The main conclusion from this section is that for the range of Re_p discussed, the θ_{c0} profiles obtained by turbulence in the absence of mean flow were qualitatively similar to the traditional Shields curve. Values of θ_{c0} were steadily increased in the hydraulically smooth bedforms and reached near-constant in the hydraulically rough bedforms. The data measured by both methods demonstrate that bed slope has a significant influence on the threshold condition for sediment motion. The measured θ_c values obtained for bedslopes $0 \leq \beta/\beta_r \leq 0.95$ were consistent with the predicted line for hydraulically rough bedforms. Particles in hydraulically smooth bedforms show a consistent trend with Equation (3.13a), where measured θ_c were found either to be slightly lower, falling on, or in the region between the two predicted trends.

Chapter 5

The characteristics of sediment interaction

This chapter describes a preliminary investigation, conducted at the end of PhD period to identify how near-bed turbulence interacts with and moves sediment. To provide additional insight into the interaction characteristics, the PIV technique was also adapted to measure the velocity field of the displaced sediment grains (within the transverse plane of the bed surface) during the interaction. Measurement of the velocity of the displaced sediment grains was restricted to the $\theta/\theta_c > 1$ case and two sediment types with comparable sizes. These restrictions preclude using the sediment velocity data for an in-depth parametric analysis, and so the focus here was to provide novel data that could be used to illustrate in detail the impact characteristics of sediment trajectory under the influence of zero-mean turbulence.

5.1   Experimental apparatus and setup

A similar experimental setup as discussed in Chapter 3 was used. The complete schematic of the experimental setup is illustrated in Figure 5.1. The grid was positioned so that the bed surface was always at $z \approx 2.5M - 2.6M$. For consistency, a stroke of 8 cm was used throughout with frequency varied between 3 to 3.1 Hz, resulting in Reynolds numbers, Re_M, of approximately 12000. For sediment interaction close to the critical condition (i.e. $1 \leqslant \theta/\theta_c \leqslant 1.5$), it was noted that only a minimal amount of sediment motion was induced. Hence, to ensure that detectable and/or observable levels of sediment motion
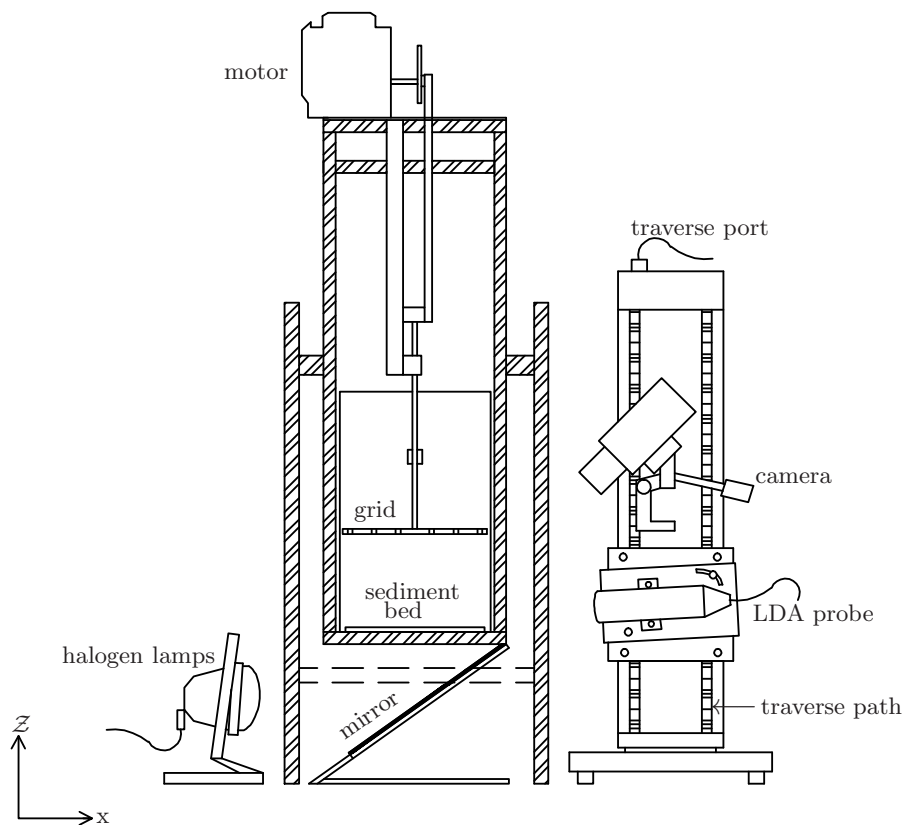
Figure 5.1: A side view schematic representation of the experimental setup for the turbulence-particle interaction experiments. The LDA probe is attached to a plate that can be tilted up to 5°, and is mounted on a traverse system.
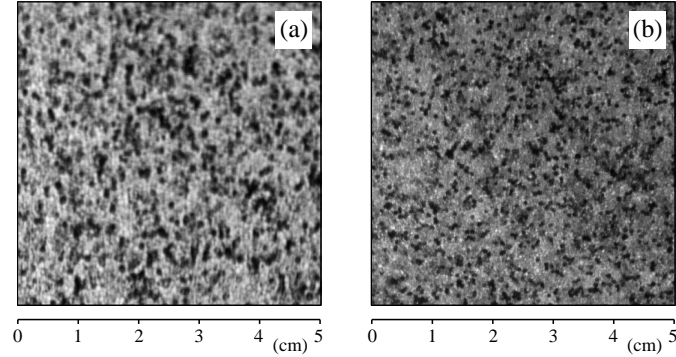
Figure 5.2: Images showing two different layers of mixed black and transparent particles, (a) Ballotini with $d_p = 701\,\mu$m (Particle B), and (b) Diakon with $d_p = 751\,\mu$m (Particle H). In both images the mixture ratio is 30% black, 70% transparent, and the region shown is an area of $5 \times 5\,\text{cm}^2$ on the bed surface.

occurred, the experiments were performed in the range $\theta/\theta_c \approx 4.3$ and 4.8. Attention was also restricted to horizontal beds, $\beta = 0$.

Particle	s	f_g (Hz)	θ/θ_c	Re_M ($\times 10^3$)
B	2.50	3.1	4.26	12.6
H	1.18	3.0	4.76	12.2

Table 5.1: Summary of experimental parameter.

The aforementioned experimental procedure was restricted to Particles B and H (with $d \approx 701$ and $750\,\mu$m, respectively). These two types of particle were chosen as sediment size $d > 700\,\mu$m was required to resolve the structure of the sediment grains in the images captured. Although Particle A ($d = 1087\,\mu$m) was within this classification, higher f_g (more than 5 Hz) was needed to acquire satisfactorily intense particle movement, whereby PIV was able to pick up the sediment motion. Therefore, for the experimental setup available, this was not feasible. Note that a too energetic interaction could result in a significant number of sediment grains being resuspended above the impact region (Munro et al., 2009), which would obstruct the camera view and affect the sediment velocity measurements. For this reason, particularly for Particle H due to low density, attention was restricted to impacts (of sediment motion and trajectory) which resulted in a minimal level of resuspension. The experimental parameters i.e., the frequency used, f_g, corresponding values of θ/θ_c and Re_M are summarised in Table 5.1.

Each sediment layer of depth 1 cm was prepared as described in Section 3.1. The

velocity of the displaced sediment grains were measured using a simple adaptation of standard PIV. In this case, a random pattern structure was established within the bed using black sediment grains added to, and mixed thoroughly with, the otherwise transparent sediment. The transparent sediment bed is illuminated by using two high power halogen lamps and the light was directed up into the tank by a mirror located beneath the tank base (see Figure 5.1). To track the sediment motion black opaque sediment grains were added to the otherwise transparent sediment (with ratio 10:1 transparent to black) which acted as tracer particles. Images of the two seeded sediment layers produced in this way (prior to impact) are shown in Figure 5.2. In each case, the basic properties of the black particles (d and Re_p) were the same as those corresponding regular sediment. Best results were obtained using a particle mixture ratio of about 30% black to 70% transparent.

A high speed digital camera was supported on a tripod and positioned to view down onto the sediment layer. The images were captured using the NanoSense II high speed camera with 1024×1280 pixel resolution at 12 bits per pixel, used in conjunction with a Nikon Zoom-Nikkor 60 mm F2.8 $\sim$ 11 lens. The digital camera was positioned at a distance of 20 cm from the tank and was focused to view vertically down onto the sediment layer surface at an angle of approximately $53.1°$ (ideally at $90°$). This was the maximum permissible angle to avoid any image distortion caused by the perspex tank. Note that the camera could not be positioned to view vertically down into the tank due to the presence of the grid. The camera was positioned to capture as wide as possible region of the sediment bed while still sufficiently resolving the structure of the grains in the bed. As the turbulence interacted with and displaced the near-surface sediments, the motion and trajectories of the tracer grains were captured in the images. Measurements of the particle trajectories were obtained using the PIV software in Digiflow (Dalziel research) using an interrogation window of 15×15 square pixels. To satisfactorily resolve the short time scale associated with each eddy impact, it was necessary for the image sequences to be captured using the high speed camera sampling at 200 and 400 Hz for particle H and B, respectively.

Within the field of view, intermittent sediment motions could occur randomly in the sediment plane. It should be noted that due to the tilted view of the PIV camera, the spatial resolution in the y (transverse) direction is limited. To obtain the physical scale of velocity, the pixel image coordinates were converted to physical coordinates using the linear-mapping procedure in Digiflow. For this, an array of $1 \times 1 \, \mathrm{cm}^2$ grids was placed on the bottom of the tank and an image was taken. The physical grid was then used

velocity range (hor)	$-0.07 \sim 0.07$ m/s
velocity range (ver)	$-0.07 \sim 0.07$ m/s
max acquisition time	30 s
max no. of bursts	5000
detection mode	coincidence
data collection mode	burst
burst sampling time	8.53×10^{-5} s
tracer	$1\,\mu$m glass powder

Table 5.2: Summary of main LDA settings

to identify orthogonal points that could be used in the mapping procedure. For each set of experiments, the sediment velocity data was obtained during the entire experimental period. The sediment velocity fields were obtained in terms of the right-handed Cartesian coordinates $(x, y, 0)$, defined by the (x, y)-axes in the transverse plane of the bed surface at $\mathcal{Z} = 0$. The particle velocities, denoted by $u_p(x, y, t)$ and $v_p(x, y, t)$ for the horizontal and transverse components respectively, were obtained under the same interaction conditions and at corresponding times during the impact.

The fluid velocity measurements (to calculate θ) were obtained using a 2D Laser Doppler Anemometry (LDA) FlowLite optic (Dantec dynamics) operating in the back scatter mode. The LDA probe was placed at distance of approximately 10 cm from the tank and at a height parallel to the sediment bed. In order to (closely) represent the actual fluid velocity acting on the particle, it was imperative for detailed flow measurements to be made at points near to the sediment bed. Therefore, the LDA laser beams were directed into the tank through the side wall so that the beam intersection point (with measuring volume of approximately $650\,\mu$m in length and $77\,\mu$m in diameter) was positioned at height $\mathcal{Z} = 0.5$ cm ($\xi \approx 0.3$) above the bed, corresponding to the point of r.m.s. horizontal velocity amplification. Within this setup, the average sampling rate of the LDA was approximately 10 - 50 Hz and the measurement was taken at $T = 90$ s.

Tap water was used, and the dissolved minerals present in the water were sufficient enough to act as tracer particles. However, to improve the LDA sampling rate, a small volume amount of polyamide particles ($\rho_s = 1.03\,g/\text{cm}^3$) with mean diameter of $5\,\mu$m were added. The signal response of the LDA was processed by a DANTEC 57N10 Burst Spectrum Analyser (BSA). The BSA software analysed each burst and obtained the velocity measurements from the frequency of the scattered light signal. The detection mode used

is 'coincident', which enabled simultaneous measurements of both horizontal and vertical velocity components. A summary of the most important LDA settings used is shown in Table 5.2. In this chapter, the (instantaneous) measured fluid velocities will be denoted by $\tilde{u}_f(t)$ horizontal and $\tilde{w}_f(t)$ vertical. Note that the Shields parameter θ presented in Table 5.1 was calculated as $\theta = u_f^2/[(s-1)gd]$, where u_f is the r.m.s. horizontal fluid velocity and is calculated as

$$u_f = (\overline{u_f'^2})^{1/2} = \sqrt{\frac{1}{N-1}\sum_{n=1}^{N}(\tilde{u}_f(t_n) - \overline{u_f})^2}, \tag{5.1}$$

where u_f' and $\overline{u_f}$ are the fluctuating and mean fluid velocities, respectively and $n = 1, 2, 3, ..., N$ and N is the total population of $\tilde{u}_f$.

5.2   Results

5.2.1   A typical turbulence-sediment interaction

A qualitative description of a typical sediment 'splash' induced by the interacting turbulence is presented. The term splash is used here to characterise the typical sediment movement induced by the impingement of an energetic eddy with the sediment bed. Recall that we will present the data two sediment types: Particle B with $\theta/\theta_c = 4.26$ and Particle H with $\theta/\theta_c = 4.76$. Note that from Table 5.1, the level of flow strength at near-bed region is comparable for both sets of data. In both cases $\beta = 0$. Throughout the period of capturing images, intermittent energetic sediment movement on the bed surface was observed. However, to describe the sediment's motion, we isolate one energetic interaction for each data set. Upon scrutinizing approximately 10 frames at the initially identified interaction period, the point from which particle movement was visible to the naked eye was taken to be t_0 with the range of the t_0 error circa $\pm 0.0125 - 0.025$ s (≈ 5 frames).

Figures 5.3 and 5.4 illustrate a typical splash event, shown in a transverse plane of particle velocity fields with vorticity distributions for Particle B ($\theta/\theta_c = 4.26$) and Particle H ($\theta/\theta_c = 4.76$), respectively. To prevent data saturation, only every the 30th velocity vector has been included in each of the velocity fields shown in Figures 5.3 and 5.4. For each impact, the corresponding horizontal and transverse particle velocities at one fixed point (in the y-direction), denote as $u_p(x)$ and $v_p(x)$, respectively are shown. The point is usually taken corresponding to the middle of the eddy impingement, shown as thick
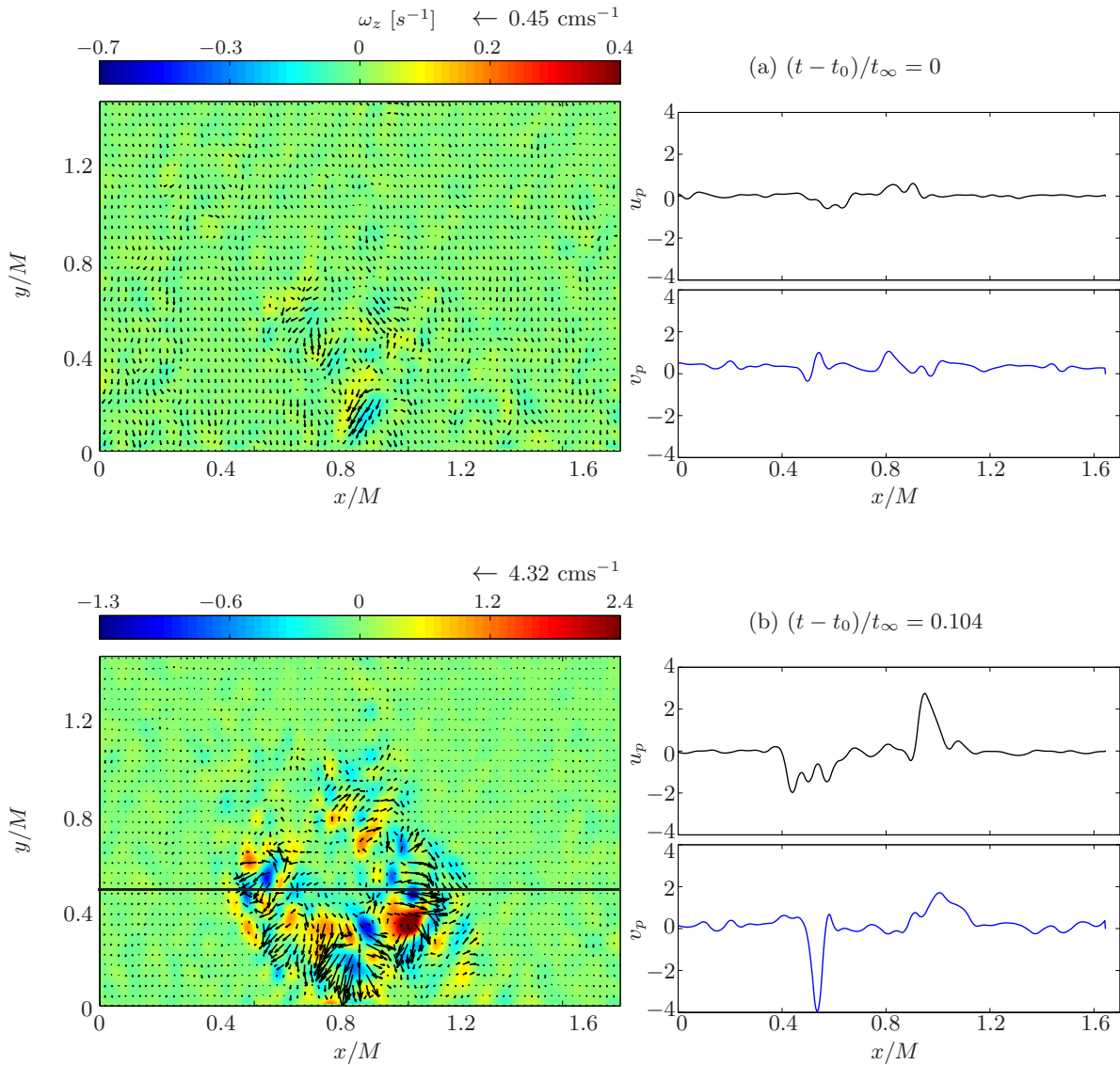
Figure 5.3: Sequences of measured particle velocity fields for Particle B ($d = 701\,\mu$m) with vorticity $\omega_z = \partial u_p/\partial y - \partial v_p/\partial x$ distributions (shown as left figure) and corresponding horizontal u_p and transverse particle velocity v_p at a fixed point obtained at corresponding dimensionless times with $t_\infty = 0.723$. The impact shown corresponds to turbulence produced from $S = 8$ cm, $f = 3.1$ Hz, $\theta/\theta_c = 4.26$ interacting with a sediment layer of particle B (with $\beta = 0$). Correspond maximum horizontal particle velocity is shown on the top right corner of left figure. The solid black line in (b) illustrates the corresponding $y-$point where u_p and v_p were taken.
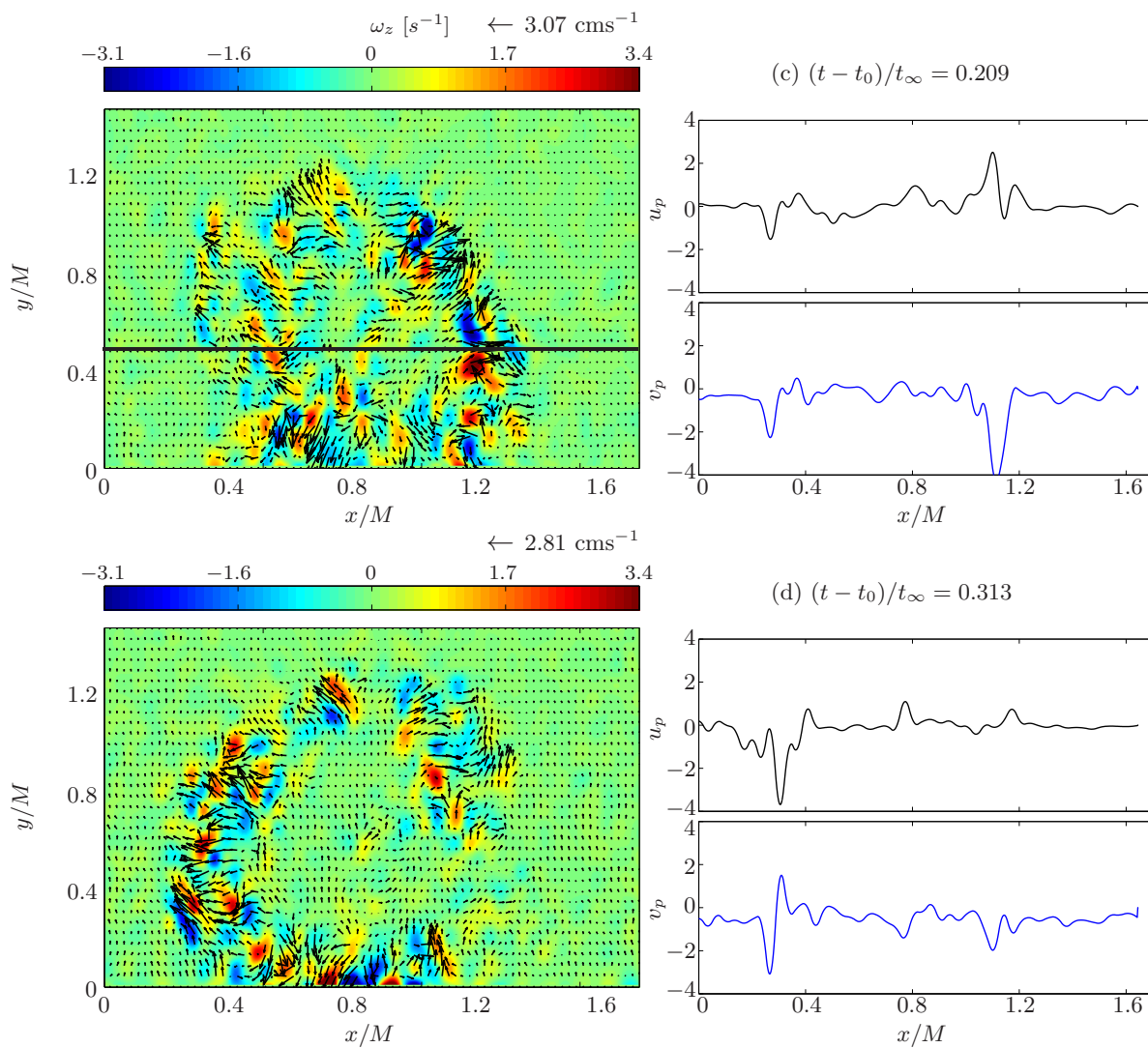
The solid black line illustrates the corresponding point where u_p and v_p were taken.
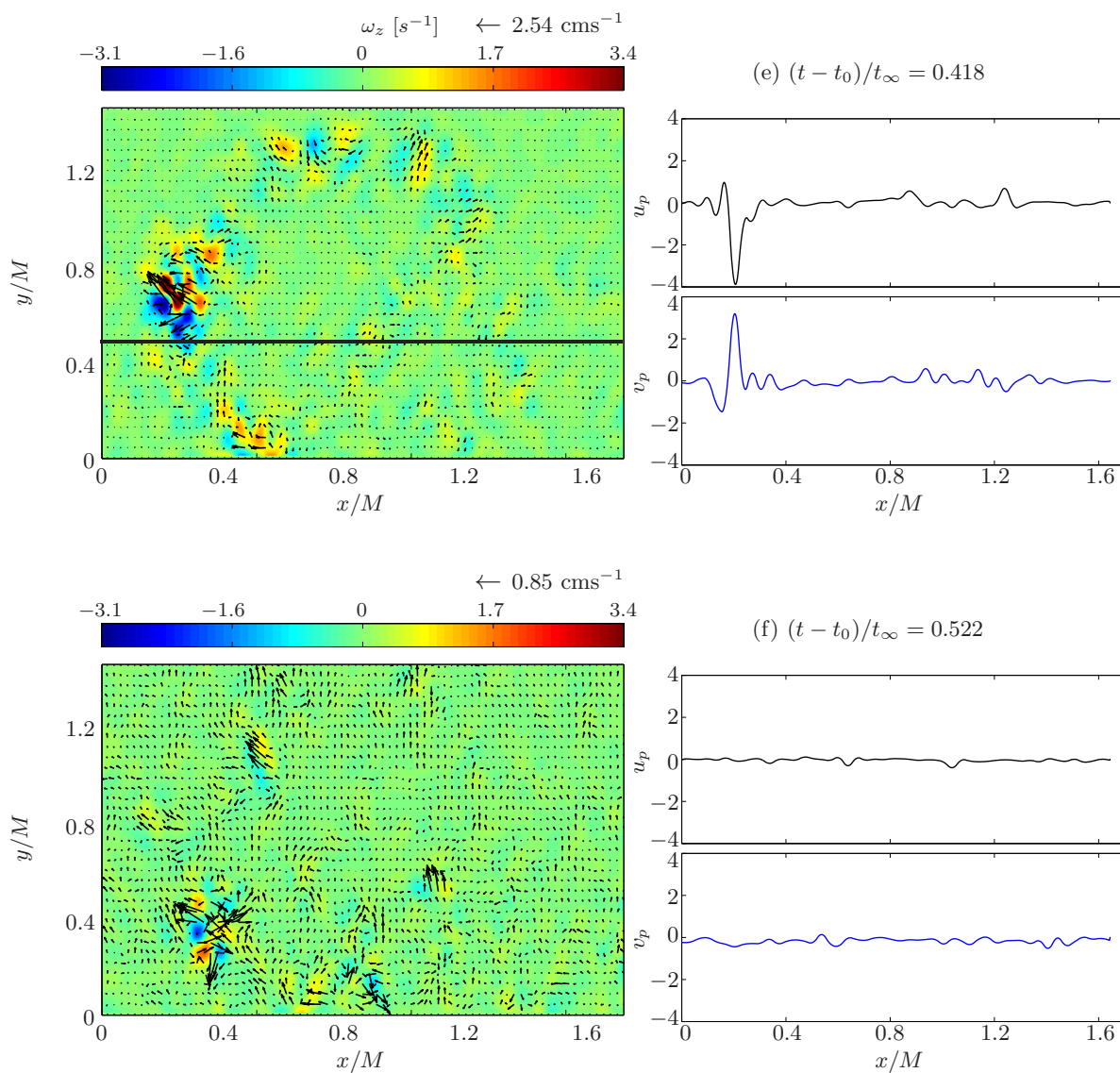
The solid black line illustrates the corresponding point where u_p and v_p were taken.
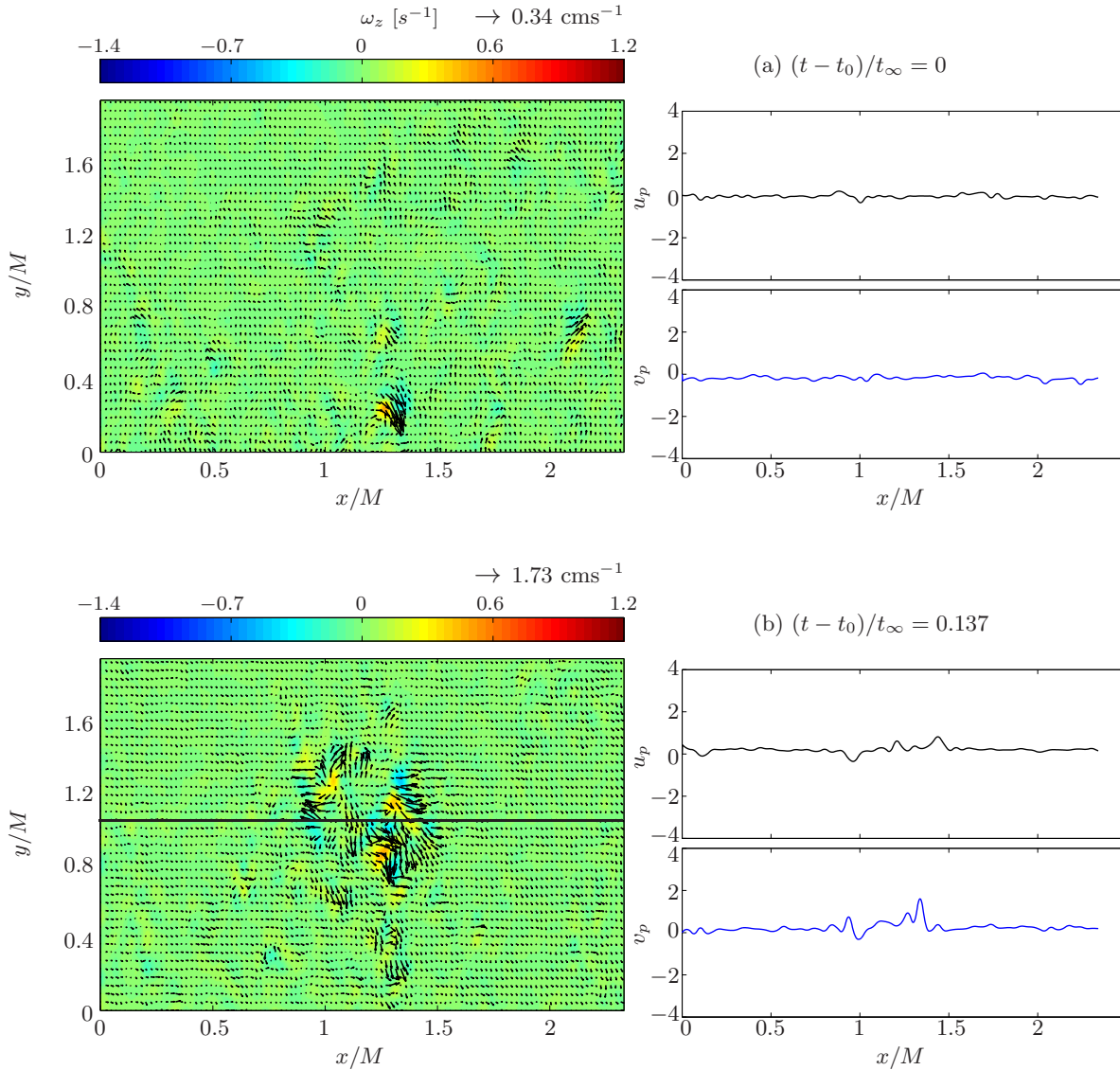
Figure 5.4: Sequences of measured particle velocity fields for Particle H ($d = 751\,\mu$m) with vorticity $\omega_z = \partial u_p/\partial y - \partial v_p/\partial x$ distributions (shown as left figure) and corresponding horizontal u_p and transverse particle velocity v_p at a fixed point obtained at corresponding dimensionless times with $t_\infty = 1.525$. The impact shown corresponds to turbulence produced from $S = 8$ cm, $f = 3$ Hz, $\theta/\theta_c = 4.76$ interacting with a sediment layer of particle H (with $\beta = 0$). Correspond maximum horizontal particle velocity is shown on the top right corner of left figure. The solid black line in (b) illustrates the corresponding $y-$point where u_p and v_p were taken.
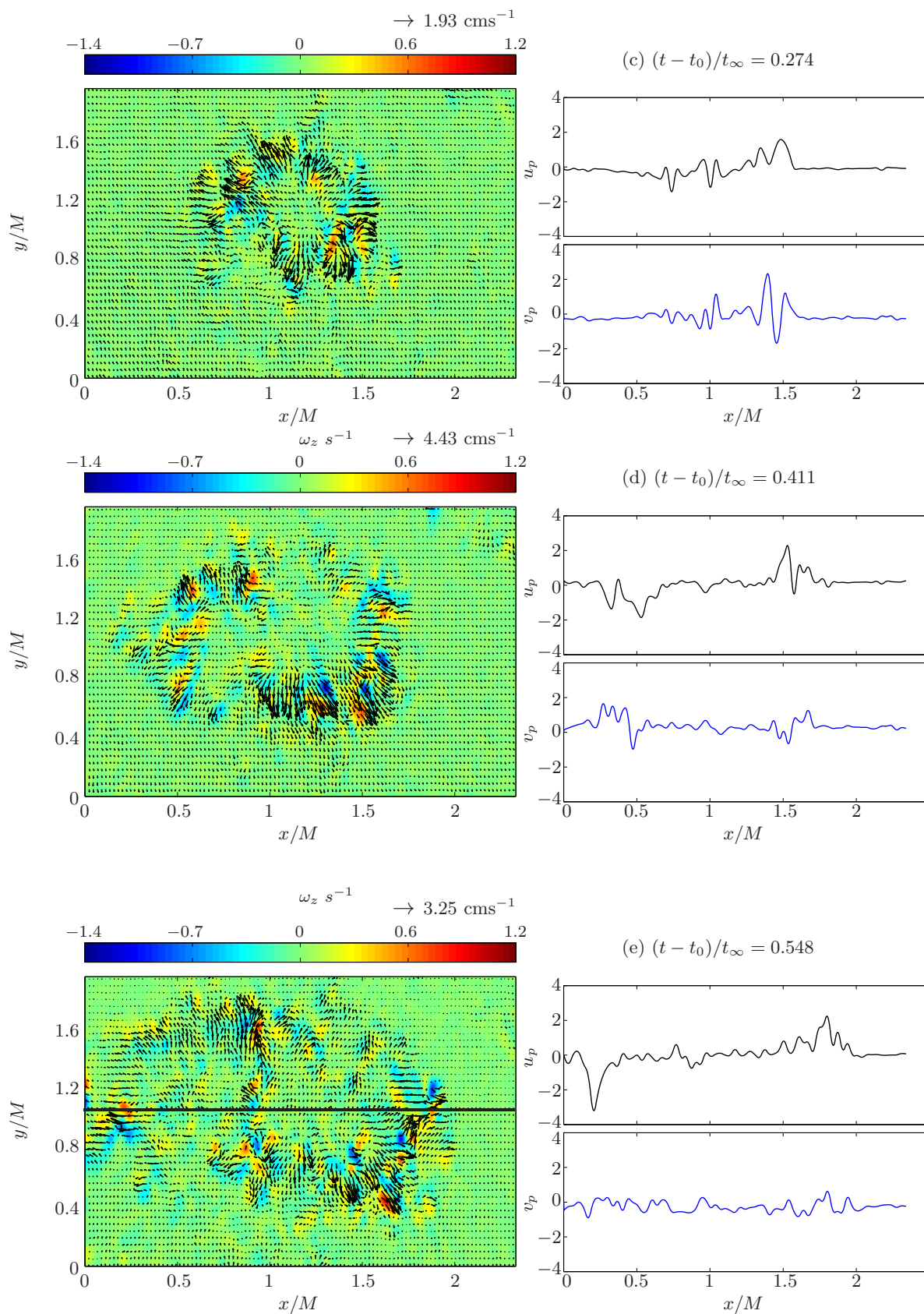
The solid black line illustrates the corresponding point where u_p and v_p were taken.
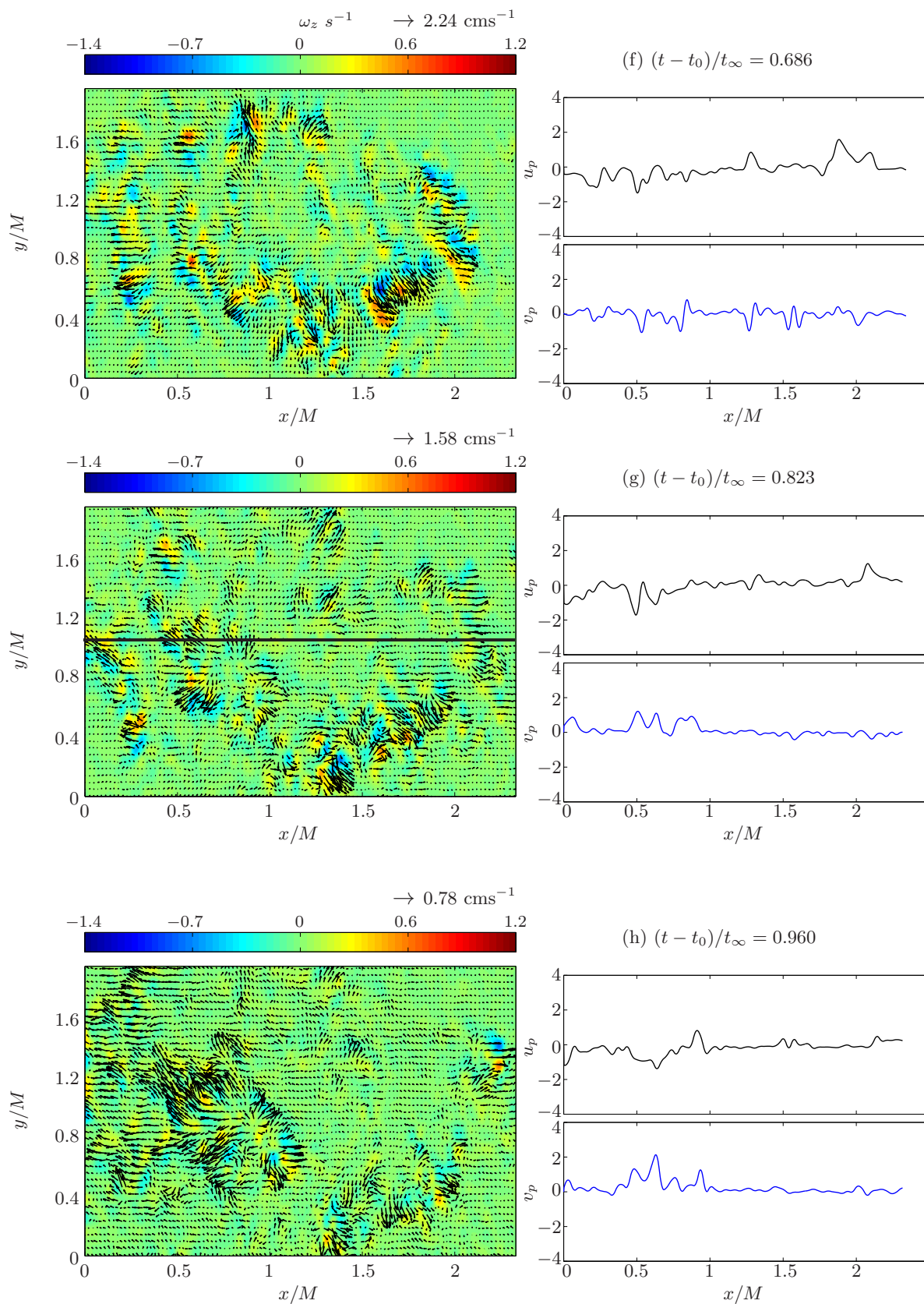
The solid black line illustrates the corresponding point where u_p and v_p were taken.

black line for each case (for example, see Figure 5.3(b)). Corresponding dimensionless times $(t - t_0)/t_\infty$ are shown at the top of each figure, where $t_\infty = l_\infty/u_\infty$ is the integral time scale. The value of l_∞ was calculated using the relation $l_\infty = 0.1z$ and u_∞ was computed using Equation (1.10), with $z = 13.5$ cm and $z = 15.5$ cm for Particle B and H, respectively. The averaged maximum particle velocity in the (x, y) plane is also shown for each time evolution at the top corner.

Figures 5.3 and 5.4 show that the typical particle trajectories take the form of a circular splash with dominant horizontal and transverse particle velocities. At other regions where $\theta < \theta_c$, no trajectory was observed. As an energetic eddy approaches the bed surface, momentum is transferred from the fluid vertical velocity component to the motion parallel to the bed surface (i.e., horizontal and transverse fluid velocity) due to the formation of a splat event. Recall the splat and antisplat events described in Figure 3.6 in Section 3.2. The increasing momentum in the transverse plane induces bed shear stress in the near-bed region. During interaction, the bed shear stress increases and acts to thin the inner viscous sublayer, thereby exposing the near-surface sediment grains in this region to greater hydrodynamic drag and lift forces (Munro et al., 2009). At $(t - t_0)/t_\infty = 0$, significant particle movement was not detectable. When the condition $\theta > \theta_c$ is satisfied, near surface sediment grains are brought into motion. At this point in time, the sediment grains are subjected to a nonzero component of horizontal and transverse fluid velocity which acts to propel them away from the bed surface, forming the characteristic particle splash. Consequently, the PIV started to capture the particle movement, giving a corresponding increase to u_p and v_p (in two opposite directions). For example, Figure 5.3(b) shows two distinct peaks of u_p and v_p (at $t = 0.104t_\infty$). Note that u_p and v_p increased within the same distance x/M (see Figure 5.3(b)). Corresponding increasing particle velocities u_p and v_p suggesting that the particles movement is induced by the splat events. As the stretched eddy diameter increases, the radius of splash increases. Both u_p and v_p also increase until reaching an instantaneous peak velocity at $t = 0.21t_\infty$ and $t = 0.25t_\infty$ for Particle B and H, respectively, where the bed shear stress is maximum (Munro et al., 2009). Note that at this point ($t = 0.21t_\infty$) in Figure 5.3, the length of intense particle motion with high u_p and v_p is approximately $1M$. In Figure 5.4 for Particle H, however where u_p reached peak velocity at $t = 0.41t_\infty$, the length of visible particle movement is approximately $1.3M$. For both particle type, the integral length scale within the homogeneous region l_∞ is approximately 1.4 cm. Thus, the maximum length (i.e. at peak velocity) of sediment movement induced by the energetic eddy (in terms of l_∞) is 3.57 and 4.64 for Particle

B and Particle H, respectively. After the peak velocity is reached, the bed shear stress starts to decay. Even so, they are still high to induce particle movement and the radius of splash still increasing. Subsequently, horizontal and transverse particle velocities u_p and v_p, respectively start to decrease and the length where the particle motion were seen, are to be decreasing too. Decreasing shear stress resulted in fewer entrained particles and insufficient energy to keep the particle in motion. When the bed shear stress is no longer sufficient to induce particle movement, particles settle back to the bed. At this point, the PIV detected no significant particle movement and the circular splash disappeared. Note that for Figure 5.4(h) at $(t - t_0)/t_\infty = 0.96$, the intense particle motion between $0.5 \leq x/M \leq 1$ is a new energetic interaction.

For the data set used in Figures 5.3 and 5.4, although a circular sediment displacement was observed, over the splash period, the particle trajectories were seen not to be able to sustain a coherent circular displacement (for example, see Figure 5.3(d) and Figure 5.4(d)). The reason behind this could be the fact that the horizontal and transverse fluid velocities acting on the particles (in the isolated spots) have been dissipated by the viscous forces. Viscous friction along the bed prevents the total amount of kinetic energy being transferred to the tangential components (by splat events) (Perot and Moin, 1995; Bodart et al., 2010). Thus, the fluid velocities (in the transverse plane) acting on the particles are reduced and the energy available is not sufficient to keep the particles in (intense) motion. Another possible reason is due to the low intensity of the particle movement, whereby the movement of particles was not able to be picked up by PIV.

Both examples show that the duration of particle movement induced by energetic eddies is within one eddy turnover time (equivalent to t_∞), in the examples shown $t = 0.52t_\infty$ and $t = 0.96t_\infty$ for Particle B and H, respectively. Note that although θ/θ_c are comparable between the two cases discussed, the maximum diameter of circular splash attained for Particle H (in Figure 5.4) is approximately $2M$, where as for Particle B (in Figure 5.3), the maximum diameter is approximately $1.1M$. The longer sediment displacement and larger splash diameter for Particle H is because the particles are easily entrained into the turbulence structure above the bed due to its low particle relaxation time (i.e. low density). It was also observed that the mode of sediment grain displacement for particle B was dominantly rolling. Rolling particles moved with a persistent contact with bed resulted energy (transferred from the high momentum fluid) within the particles has always need to overcome the resistance forces (imposed by the bed), leading to more energy dissipation. As the bed is mobile, the effective friction coefficient is higher, enhancing the

momentum transfer to the bed (Lajeunesse et al., 2010). Thus, the energy within the level of flow strength discussed (for Particle B) to induce particle motion, is reduced. Particle H, however was observed to move dominantly in a saltating mode. Saltating particles are entrained into the outer flow, have minimum contact with sediment bed and are easily entrained by the turbulence structure. This gives longer times and distances of particle displacement for Particle H. Under the turbulence-particle interaction discussed here, the distance of particle displacements induced by the turbulence are found up to approximately $41.2d$ and approximately $91.2d$ away from the eddy center for Particle B and H, respectively. Recall that d is the sediment size.

It is worth highlighting that as the fluid velocity in the near-bed region was not spatially measured, the spatial fluid velocity 'i.e.' instantaneous horizontal and vertical fluid velocities evolution along the bed surface could not be investigated. Thus, a detailed analysis on how the splat and antisplat events interact, and move sediment is currently not feasible.

5.3 Summary

The adaptation of using PIV to measure particle velocities was able to identify circular (splash) particle trajectories. Identifiable increasing horizontal and transverse particle velocities indicate that particle trajectories are induced by the splat events. However, particle velocity measurements using PIV is very much dependent on how many particles are displaced within the interrogation area to obtain accurate measurements, and therefore was not considered suitable to investigate particle movement under a low strength of fluid flow.

During the interaction, horizontal and transverse particle velocities increased as the energetic eddy approached and stretched along the bed surface, attaining peak values at $(t-t_0)/t_\infty \approx 0.41$ for Particle B and $(t-t_0)/t_\infty \approx 0.25$ for Particle type H. After reaching peak values, both u_p and v_p decrease to zero as the bed shear stress decays. These preliminary experiments provide an initial setup for future work on employing the zero-mean turbulence and to study its interaction with a sediment layer. Further experiments to investigate the particle behaviour under higher θ/θ_c and varying sediment type (i.e. density and size) will be beneficial. Note that due to the time restriction of the PhD period, this investigation was not conducted.

Chapter 6

Summary and Conclusions

6.1 Summary of thesis

The experiments reported in this thesis investigated the interaction between zero-mean turbulence generated by an oscillating-grid in a water tank and a sloping 'planar' sediment layer. In specific terms, the tests undertaken focused on analysing how the critical conditions for incipient sediment motion 'in terms of the critical Shields parameter θ_c' would be affected by sediment characteristics (i.e. size and density) and by systematically increasing the bed slope. θ_c was defined in terms of the peak r.m.s. horizontal fluid velocity measured adjacent to the bed in the surface-influenced layer. Previous bed slope studies used data obtained in steady turbulent channel (or conduit) flows, and focussed exclusively on hydraulically rough bedforms (typically $d \gtrsim 500\ \mu$m), and bed slopes between $0 \leqslant \beta/\beta_r \leqslant 0.8$ (Chiew and Parker, 1994; Lamb et al., 2008). The experiments reported here included both hydraulically smooth and hydraulically rough beds (using sediments with d in the range 80 to 1087 μm) and bed slopes $0 \leqslant \beta/\beta_r \leqslant 0.9$.

The oscillating-grid mechanism used in this study was found to produce steady quasi-isotropic homogeneous turbulence which had statistical properties similar to that reported in previous studies (Thompson and Turner, 1974; Hopfinger and Toly, 1976; Silva and Fernando, 1992; Cheng and Law, 2007). This provided a basis for the study of the critical conditions for sediment motion by a turbulent flow in which the fluctuations were dominant in comparison to the mean flow. This chapter summarises the conclusions of this work and outlines the key areas for further investigation.

6.1.1 Oscillating-grid generated turbulence

In this study, the turbulence produced by the vertical oscillating-grid is consistent with the standard results obtained by Thompson and Turner (1974) and Hopfinger and Toly (1976). The region of quasi-isotropic homogeneous turbulence was found at $z \geq 2.5M$ away from the grid midplane (i.e. virtual origin). Within the quasi-isotropic homogeneous region, the turbulence was found to decay spatially according to the power law $u \propto z^{-n_u}$, with $n_u = 1.22$ (for horizontal velocity component). The longitudinal integral length scale increased linearly with z as, $l = \beta_l z$ with the empirical coefficient $\beta_l = 0.11$. Previous oscillating-grid studies only focussed on the determining the decay law for the horizontal velocity fluctuations and assumed the decay law for vertical components $n_w = n_u = 1$ because of isotropy. This was extended further in this study to investigate the decay behaviour of the r.m.s. vertical velocity component w according to $w \propto z^{n_w}$. It was found that n_w (with values of 1.44) has higher value than n_u (with values of 1.22) when $S/M \leqslant 0.8$. However, for $S/M > 0.8$, the n_u and n_w were both comparable at approximately 1.

In this study, the sediment bed was positioned at a distance between $z \approx 3M$ and $3.5M$ corresponding to a region where the turbulence is quasi-isotropic and homogeneous in the absence of the bed. The presence of the sediment bed disrupted the turbulence structure, and a region of inhomogeneity (i.e. the surface-influenced layer) was observed up to a distance $1.5l$ above the bed surface. Within the surface-influenced layer, the r.m.s. horizontal velocity component u was amplified at approximately $0.1M$ above the bed, at the expense of r.m.s. vertical velocity due to the kinematic ($w = 0$) boundary condition. Changes in the r.m.s. velocity profile at near sediment bed indicated the occurrence of 'splat-antisplat' events, following standard changes of zero-mean turbulence structure at (solid) boundaries (Perot and Moin, 1995; Campagne et al., 2006; Bodart et al., 2010). The consistent occurrence of the r.m.s. horizontal velocity amplification at a distance of approximately $0.1M$ above the sediment bed provides a sensible fluctuating velocity scale for defining the critical Shields parameter θ_c.

6.1.2 Critical criteria for incipient sediment motion

The profile obtained from the measured values of θ_c on a horizontal sediment bed against particle Reynolds number is qualitatively comparable with the established Shields diagram obtained in turbulent channel flow. The profile also demonstrates that the limit for hydraulically smooth bedforms is $d/\delta_v \approx 5$ (which corresponds to $d \sim 350\,\mu\text{m}$), in agreement

with White (1970). Below $d < 350\,\mu$m, the bed roughness (k_s) was comparable to, or smaller than the viscous-sublayer thickness, and so viscous stresses act to significantly reduce the hydrodynamic drag and lift forces acting on the near-surface particles. Consequently, the measured values of θ_c for $d/\delta_v \lesssim 5$ were observed to increase monotonically with decreasing d/δ_v. For hydraulically rough bedforms $d/\delta_v \gtrsim 5$, the effects of viscous damping ceased to be evident, leading to θ_c becoming near constant. These observations are consistent with smooth-bedforms limit of $Re_* \approx 5$ (corresponding to $d \approx 200-300\,\mu$m) identified in previous studies (Shields, 1936; White, 1970).

Bed slope has been shown to have a significant effect on θ_c. The bed becomes more mobile with increasing bed slope due to the additional downslope gravitational force acting on the near-surface sediment. The measured values of θ_c obtained for bed slopes $0 \leqslant \beta/\beta_r \leqslant 0.9$, were compared with a simple force-balance model, based on the criteria for threshold sediment motion on a sloping bed. The standard derivation of this model, corresponding to hydraulically rough bedforms is shown by Equation (3.13b). In this study, the model was extended to account for the case of hydraulically smooth beds. That is, for $k_s/\delta_v \lesssim 5$, near-surface sediment grains are exposed to reduced drag and lift forces, which here are assumed $\mathcal{O}(\rho\epsilon^2 u_c^4 d^4/\nu)$ (Krishnan and Leighton, 1995; Eames and Dalziel, 2000). In this case, the corresponding model takes the form given in Equation (3.13a). Comparing both equations shows that the damping effect of the viscous sublayer acts as a stabilizing mechanism for smooth beds, reducing the rate at which the bed mobility increases with bed slope. The measured values of $u_{c\beta}/u_{c0}$ for hydraulically rough bedforms were consistent with theoretical predictions obtained using Equation (3.13b). However, the θ_c obtained in the hydraulically smooth bedforms were lower than the predicted curve and acted in a similar fashion to a hydraulically rough bedform for $\beta/\beta_r \leq 0.65$. This is believed to be due to the interaction of intermittent energetic eddies disrupting the viscous sublayer and reducing the critical velocity u_c needed to move the particles. Approaching the angle of repose $\beta/\beta_r > 0.65$ however, the transition to hydraulically smooth bedforms was observed and falls in the region between the two predicted trends of hydraulically smooth and rough bedforms. Furthermore, the data shows a transition in behaviour between the smooth-bed and rough-bed cases when $d/\delta_v \approx 5$ (in agreement with the threshold identified from the θ_{c0} data.

The basis of the arguments used to derive Equation (3.13a) in hydraulically smooth bedforms are not unique to the interaction considered in this thesis, and are expected to apply also to fully turbulent flows.

A qualitative comparison with the θ_c measured by turbulence in the form of vortex ring, a laminar single idealised eddy, was also conducted for the bed slope ranges $0 \leq \beta/\beta_r \leq 0.95$. The measured values of θ_{c0} obtained by both methods produced similar profile to the traditional Shields curve. The data obtained by vortex ring experiments also show that bed slope has a significant influence on the critical conditions for incipient sediment motion. The measured θ_c were consistent with the predicted values (using Equations (3.13)), with values either falling on, or in the region between the two bed cases. These findings show that the turbulence in the absence of mean flow provides a similar θ_c profile to the values obtained using statistically steady turbulent flow. Thus, the fluctuating components are responsible for the critical condition that gives rise to the incipient motion and should been take into account in calculating bed-load sediment transport.

6.1.3 Turbulence-particle interaction

A preliminary description of how zero-mean turbulence interacts, and moves sediment was presented. The simple adaptation of PIV to obtain the particle velocity proved reliable, although it is restricted in only being able to identify particle movement under flow higher than the critical condition $\theta/\theta_c > 4$ for particles with relative density $s = 2.5$ and $\theta/\theta_c > 1.5$ for particle with $s = 1.18$. Noticeable levels of sediment could not be detected below this limit.

Energetic eddies impinging on the sediment bed and increase the local bed shear stress at the near-surface particles, thereby exceeding the threshold for critical sediment motion, which consequently initiates particle movement. The horizontal velocity acts as the driving force for the sediment motion and transports them along the bed in a 'splat' event. The sediments trajectories during the interaction show the individual grains are being displaced in a circular pattern, giving dominant horizontal and transverse particle velocities. The particles moved with increasing velocity until they reached peak velocity. After this time, the turbulence, hence the bed shear stress decays resulting in decreasing particle velocities. The particle velocities decreased back to zero to the point where the particles settled back to the bed. The particles that interacted with an energetic eddy were capable of achieving a maximum distance $x/d \approx 90$ (depending on the sediment density) away from its original position.

6.2 Thesis conclusions

The main difference employed in this study is that the turbulence intensity level (in terms of the horizontal component) is $u/\overline{u} \geq \mathcal{O}(1)$, whereas in the developed traditional Shields diagram, the turbulence intensity level is $u/\overline{u} \leq \mathcal{O}(1)$. The critical conditions that give rise to the incipient sediment motion thus is calculated using r.m.s. horizontal velocity. The effect of the fluctuating velocity components on the θ_c values over the range of sediment size and density discussed here produced comparable profile with the traditional Shields diagram. The similarity of Shields parameter profile obtained is due to the statistically stationary flow used. The fluctuating forces acting on a particle and affect its mobility could be from the fluctuating drag or lift forces, turbulence-induced pressure gradient or from vortex shedding from a protruding particle. Regardless how the turbulence is generated, it is expected that the critical Shields profile would remains similar, i.e. an increase of θ_c for hydraulically smooth bedform (i.e. as the sediment size decrease) and reached near-constant value of θ_c as the sediment size falls under the hydraulically rough bedform.

The incipient sediment motion on bed slope depends on the bed roughness. Smaller sediment submerged within the viscous sublayer where the effect of viscous is significant and this more energy needed (in a large scale eddy) to firstly disrupt the viscous sublayer and induced sediment movement. The value of θ_c on a bed slope from horizontal bed decreases as approaching to the angle near repose limit. The additional weight component (parallel to the bed), subsequently reducing the effective weight parallel to the bed lowering the θ_c particularly for sediment in the hydraulically rough bedform.

6.3 General conclusions

The problem of sediment transport is extremely complex. It is impossible to incorporate and/or simulate all inter-related or inter-dependent factors such as physical sediment characteristics, flow behaviour and bedform features in one experiment and to subsequently produce a single relation capable of representing exhaustively all flow types for different natural streams. Nonetheless, this study has provided further insight into the versatility and reliability of the Shields curve in the case of zero-mean turbulence for horizontal and angled sediment beds.

6.4 Recommendations for future work

Proposals for future research are outlined below as follows;

1. Experiments in Chapter 5 are extended to larger sediment sizes and higher turbulence impacted on sediment bed. Detailed measurements of the particle (motion) front position, frontal speed and acceleration induced by turbulence is of particular interest. Particle velocities are obtained using the simple adaptation of PIV (as discussed here). The level of turbulence is adjusted by changing the stroke and frequency of oscillation.

   To provide a better understanding of how the near-bed turbulence interacts with and moves the sediment, analysis on the correlation between sediment trajectories and the corresponding fluid velocity acting on the particles is important. Fluid velocity is measured using a Laser Doppler Anemometer (LDA) and particle velocity is obtained using PIV. Both the PIV and the LDA measurements should be placed within the same region of interest. A few studies have attempted to investigation this correlation in a fully turbulent flow (Sechet and Guennec, 1999; Papanicolaou et al., 2002), but faced difficulties in getting sufficient quality measurements of particle motion within the same position of the fluid velocity measurement point. A similar investigation i.e. the interaction of turbulence in the form of single idealised eddy vortex ring with sediment on a bed was conducted by Munro et al. (2009). This can be serve as a basis for the approach of analysing data. It should be noted however that the key difference between the turbulence generated by oscillating-grid and vortex ring is the latter is a laminar flow with high degree of repeatability. Turbulence generated by an oscillating-grid is not.

2. Measurements are made of critical conditions for incipient sediment motion under increasing external turbulence in an open channel flow. Lots of studies have been devoted to the study of turbulence and sediment transport where the focus was mainly on 'internally' generated near-bed turbulence. Examples include the turbulence caused by the flow separation at the crests of bedforms (Nelson et al., 1995; Liu, 2006) and particle entrainment due to coherent funnel vortices (Kaftori et al., 1995; Niño and Garcia, 1996). In a natural flow environment however, extra turbulence may be generated 'externally', for example, as in the case of flow past hydraulic structures, such as pipelines or bridge piers. Vortex shedding from these structures can contri-

bute to increasing turbulence and would have an impact on the critical conditions for incipient sediment motion. Bed-load sediment transport increased a factor of 6 when a 20% increase in the turbulence has been found (Sumer et al., 2003). This indicates that θ_c has been significantly reduced and the sediment is easily entrained.

Experiments can be performed in a flume, with the external turbulence generated by a series of oscillating-grids. Sumer et al. (2003) employed this method to investigate the influence of turbulence on bed-load sediment transport. The grid is placed at the entrance of the flume and the sediment bed is put at the centre of the flume, so that the turbulence that reached the bed is statistically steady. The level of turbulence generated is adjusted using the frequency of oscillation and the distance between the grids to the sediment bed. The critical Shields parameter θ_c is defined using the horizontal velocity component in the near bed region. The measurement of fluid velocity can be obtained by using the non-intrusive LDA. Values of θ_c over varying sediment size and shape are averaged using an ensemble average. Besides sediment characteristics, variable parameters including the effects of bed forms and bed slope can be included and investigated.

Appendix A

Summary of measured data obtained in OGT.

Table A.1: A summary of the data presented in Figure 3.17 (listed in group of hydraulically smooth and rough boundary). Note that for Particle I, the data at angle 25° is discarded as the Re_l is below acceptable limit.

Label	α (°)	u_c (cms^{-1})	β/β_r	θ_c (10^{-2})	d/δ_v
D	0	2.086	0.000	7.91	7.798
	10	1.470	0.339	3.93	5.496
	20	1.194	0.699	2.59	4.465
	25	1.018	0.896	1.89	3.807
E	0	2.171	0.000	14.54	4.782
	10	1.712	0.300	9.04	3.771
	20	1.431	0.620	6.32	3.152
	25	1.179	0.795	4.29	2.597
F	0	2.310	0.000	23.66	3.541
	10	1.800	0.317	14.37	2.759
	20	1.350	0.655	8.08	2.069
	25	0.987	0.840	4.32	1.513
G	0	2.022	0.000	34.71	1.617
	10	1.448	0.317	17.81	1.159

Continued on next Page. . .

114

Table A.1 – Continued

Label	α (°)	u_c (cms^{-1})	β/β_r	θ_c (10^{-2})	d/δ_v
	20	1.031	0.655	9.02	0.825
	25	1.012	0.840	8.70	0.810
I	0	0.819	0.000	13.88	2.242
	10	0.710	0.270	10.42	1.943
	20	0.527	0.558	5.75	1.443
A	0	3.063	0.000	5.87	33.297
	10	2.480	0.339	3.85	26.958
	20	1.252	0.699	0.98	13.606
	25	0.813	0.896	0.41	8.840
B	0	2.198	0.000	4.63	33.297
	10	1.878	0.329	3.38	26.958
	20	1.305	0.679	1.63	13.606
	25	0.701	0.870	0.47	8.840
C	0	2.758	0.000	9.19	15.517
	10	1.770	0.321	3.78	9.958
	20	1.437	0.662	2.49	8.085
	25	0.838	0.848	0.85	4.713
H	0	1.264	0.000	12.09	9.492
	10	0.935	0.296	8.62	7.026
	20	0.712	0.611	4.99	5.346
	25	0.553	0.782	3.01	4.155

Appendix B

RODOS Specifications

Principle:	aerosol jet	particle-particle-collisions
		particle-wall-collisions
		velocity gradients
Dispersion:	pressure	0.1-6 bar
	injector airflow	300 l/min
	extraction	streamlined
Feeding:	VIBRI funnel dosing	vibrator feeder: mg - kg
	APIROS tube feed	microfeeder: μ g - mg
QA-system:	guarantee	50000 shots: 4 g cement PZ 35
Operation:	software-controlled	standard operating procedures (SOPs)
Application:	HELOS laser diffraction	0.1-3500 μm
	measuring ranges	R1 -R7

Table B.1: Technical specifications of laser diffraction RODOS.

Bibliography

D. Aronson, A.V. Johansson, and L. Lofdahl. Shear-free turbulence near a wall. *J. Fluid Mech.*, **338:363–385, 1997.**

J.F. Atkinson and L. Damiani. Turbulence measurements in a grid mixing tank. *Meccanica*, **21:87–93, 1986.**

J.F. Atkinson, L. Damiani, and D.R.F. Harleman. A comparison of velocity measurements using a laser anemometer and a hot-film probe, with application to grid-stirring entrainment experiments. *Phys. Fluids*, **30:3290–3292, 1987.**

G.K. Batchelor. *The theory of homogenous turbulence.* **Cambridge University Press, 1953.**

G.K. Batchelor. *An introduction to Fluid Mechanics.* **Cambridge University Press, 1967.**

M. Bellinsky, H. Rubin, Y.Agnon, E.Kit, and J.F. Atkinson. Characteristics of resuspension, settling and diffusion of particulate matter in a water column. *Env. Fluid. Mech.*, **5:415–441, 2005.**

J. Bodart, J.B. Cazalbou, and L. Joly. Direct numerical simulation of unsheared turbulence diffusing toward a free-slip or no-slip surface. *J. Turbulence*, **11:1–17, 2010.**

W.R. Brownlie. Prediction of flow depth and sediment discharge in open channels. Technical Report Report No. KH-R-43A, California. Inst. Tech. , Pasadena, California, 1981.

W.R. Brownlie. *Prediction of flow depth and sediment discharge in open channels*. PhD thesis, California Institute of Technoldogy, Pasadena, California, 1982.

B.H. Brumley and G.H. Jirka. Near-surface turbulence in a grid-stirred tank. *J. Fluid Mech.*, 183:235–263, 1987.

J. M. Buffington and D.R. Montgomery. A systematic analysis of eight decades of incipient motion studies, with special reference to gravel-bedded rivers. *Water Res. Res.* , 33:1993–2029, 1997.

G. Campagne, J.-B. Cazalbou, L. Joly, and P. Chassaing. Direct numerical simulation of the interaction between unsheared turbulence and a free-slip surface. In *European Conferenc on Computation Fluid Dynamics, ECCO-MAS CFD*, 2006.

G. Campagne, J.-B. Cazalbou, L. Joly, and P. Chassaing. Direct numerical simulation of the interaction between unsheared turbulence and a free-slip surface. In P. Wesseling, E. Onate, and J. Periaux, editors, *European Conference on Computation Fluid Dynamics, ECCOMAS CFD*. TU Delft, The Netherlands, 2008.

G.J. Chakrapani. Factors controlling variations in river sediment loads. *Curr. Sci.* , 88:569–575, 2005.

N. S. Cheng and A. W. K. Law. Measurements of turbulence generated by oscillating grid. *J. Hyd. Eng.* , 127:201–207, 2007.

Y. Chiew and G. Parker. Incipient sediment motion on non-horizontal slopes. *J. Hyd. Res.* , 32:649–660, 1994.

P.A. Davidson. On the large-scale structure of homogenous two-dimensional turbulence. *J. Fluid Mech.*, 20:431–450, 2007.

S. Dey and K. Debnath. Influence of streamwise bed slope on sediment threshold under stream flow. *J. Irrigation. and. Drainage. Eng.* , 126:255–263, 2000.

S. Dey, H.K. Dey Sarker, and K. Debnath. Sediment threshold under stream flow on horizontal and sloping beds. *J. Eng. Mech.* , 125:545–553, 1999.

I. Eames and S. B. Dalziel. Dust resuspension by the flow around an impacting sphere. *J. Fluid Mech.* , 403:305–328, 2000.

H. J. S. Fernando and I. P. D. D. DeSilva. Note on secondary flows in oscillating-grid, mixing-box experiments. *Phys. Fluids*, 5:1849–1851, 1993.

L.A. Giménez-Curto and M.A. Corniero. Entrainment threshold of cohesionless sediment grains under steady flow of air and water. *Sedimentology*, 56:493–509, 2009.

A. Gyr. Towards a better definition of the three types of sediment transport. *J. Hydr. Res.* , 21:1–15, 1983.

I.A Hannoun, H.J.S Fernando, and E.J. List. Turbulence structure near a sharp density interface. *J. Fluid Mech.*, 189:189–209, 1988.

E. J. Hopfinger and P. F. Linden. Formation of thermoclines in zero-mean-shear turbulence subjected to a stablizing bouyancy flux. *J. Fluid Mech.*, 114:157–173, 1982.

E. J. Hopfinger and J. A. Toly. Spatially decaying turbulence and its relation to mixing across density interfaces. *J. Fluid Mech.*, 78:155–175, 1976.

J.C.R. Hunt. Turbulence structure in thermal convection and shear-free boundary layers. *J. Fluid Mech.*, 138:161–184, 1984.

J.C.R. Hunt and J.M.R. Graham. Free-stream turbulence near plane boundaries. *J. Fluid Mech.*, 84:209–235, 1978.

D. Kaftori, G. Hetsroni, and S. Banerjee. Particle behavior in the turbulent boundary layer. i. motion, deposition and entrainment. *Phys. Fluids*, 7:1095–1105, 1995.

A.N. Kolmogorov. Dissipation of energy in a locally isotropic turbulence. *American. Math. Soc. Trans.* , 8:87, 1941.

H. Kramer. Sand mixtures and sand movement in fluvial models. *Trans. ASCE*, 100:798–878, 1935.

G.P. Krishnan and D.T. Jr. Leighton. Inertial lift on a moving sphere in contact with a plane wall in a shear flow. *Phys. Fluids*, 11:2538 – 2545, 1995.

E. Lajeunesse, L. Malverti, and F. Charru. Bed load transport in turbulent flow at the grain scale. *J. Geophys. Res.* , 115:F04001, 2010.

M. P. Lamb, W. E. Dietrich, and J. G. Venditti. Is the critical shields stress for incipient sediment motion dependent on channel-bed slope? *J. Geophys. Res.* , 113:1–20, 2008.

C. Liu, A. Huhe, and L. Tao. Sediment incipience in turbulence generated in a square tank by a vertically oscillating grid. *J. Coastal Res.* , 39:465–468, 2006.

C.R. Liu. Experiment study on sediment incipience in backward-facing step flow. *J. Hydrodyn.* , 19:173–179, 2006.

D. A. Lyn. Observations of initial sediment motion in a turbulent flow generated in a square tank by a vertically oscillating grid. In *ASCE Water Res. Eng. Conf.* , San Antonio, USA, 1995.

J. Magnaudet. High-reynolds-number turbulence in a shear-free boundary layer: revisiting the hunt-graham theory. *J. Fluid. Mech.* , 484:167–196, 2003.

P. Mantz. Incipient transport of fine grains and flakes by fluids-extended shields diagram. *J. Hydr. Div.* , 103:601–615, 1977.

T. Maxworthy. The structure and stability of vortex rings. *J. Fluid Mech.*, 51: 15–32, 1972.

T. J. McDougall. Measurements of turbulence in a zero-mean-shear mixed layer. *J. Fluid Mech.*, 94:409–431, 1979.

S. P. McKenna and W. R. McGillis. Observations of flow repeatability and secondary circulation in an oscillating grid-stirred tank. *Phys. Fluids*, 16: 3499–3502, 2004.

S.R. McLean. Turbulence structure over two-dimensional bed forms: Implications for sediment transport. *J. Geoph*, 99:729–747, 1994.

P. Medina. *Start of sediment motion and resuspension in turbulent flows: Applications of zero-mean flow grid stirred turbulence on sediment studies*. PhD thesis, Universidad Politécnica de Cataluña, 2002.

M.S. Mohamed and J.C. LaRue. The decay power law in grid-generated turbulence. *J. Fluid Mech.*, 219:195–214, 1990.

E. R. Mueller, J. Pitlick, and J. Nelson. Variation in the reference shields stress for bed load transport in gravel-bed streams and rivers. *Water Resour. Res.* , 41:1–10, 2005.

R. J. Munro and S. B. Dalziel. Attenuation technique for measuring sediment displacement levels. *Exp. Fluids*, 37:399–408, 2003.

R. J. Munro, N. Bethke, and S. B. Dalziel. Sediment resuspension and erosion by vortex rings. *Phys. Fluids*, 21:1–16, 2009.

J.M. Nelson, R.L. Shreve, S.R. McLean, and T.G. Drake. Role of near-bed turbulence structure in bed-load transport and bed form mechanics. *Water Resources. Res.* , 31:2071–2086, 1995.

Y. Niño and M. H. Garcia. Experiments on particle-turbulence interactions in the near-wall region of an open channel flow: implications for sediment transport. *J. Fluid Mech.*, 326:285–319, 1996.

R.I. Nokes. On the entrainment rate across a density interface. *J. Fluid Mech.*, 188:185–204, 1988.

P. Orlandi and R. Verzicco. Vortex rings impinging on walls: axisymmetric and three-dimensional simulations. *J. Fluid Mech.*, 256:615, 1993.

A.S. Paintal. Concept of critical shear stress in loose boundary open channels. *J. Hydr. Res.* , 9:91–113, 1971.

A.N. Papanicolaou, P. Diplas, N. Evaggelopoulos, and S. Fotopoulos. Stochastic incipient motion criterion for spheres under various bed packing conditions. *J. Hyd. Eng.* , 128:369–380, 2002.

B. Perot and P. Moin. Shear-free turbulent boundary layers. part 1. physical insights into near-wall turbulence. *J. Fluid Mech.*, 295:199–227, 1995.

M. Phillips. A force balance model for particle entrainment into a fluid stream. *J. Phys. D: App. Phys.* , 13:221–233, 1980.

C. Poelma. *Experiments in particle-laden turbulence simultaneous particle/fluid measurements in grid-generated turbulence using particle image velocimetry*. PhD thesis, Technische Universiteit Delft, 2004.

H. Rouse. Experiments on the mechanics of sediment suspension. In *Proc. of the 5th Int. Congress of Applied Mechanics*, pages 550–554, Cambridge, MA, 1939.

P. G. Saffman. On the formation of vortex rings. *Stud. Appl. Math.* , 54: 261–268, 1975.

M.W. Schmeeckle, J.M. Nelson, and J. Pitlick. Direct numerical simulation of bedload sediment transport. In *12th ASCE Engineering Mechanics Conference Proceedings*, 1998.

P. Sechet and B. Le Guennec. The role of near wall turbulent structures on sediment transport. *Water Res.* , 33:3646–3656, 1999.

A.F Shields. *Application of similarity principles and turbulence research in bed-load movement*. US Dept of Agr. ,Soil Conservation Service Cooperative Library, California Institute of Technology, Pasadena, Calif., 1936.

A. B Shvidchenko and G. Pander. Flume study of the effect of relative depth on the incipient motion of coarse uniform sediments. *Water Res. Res.* , 36: 619–628, 2000.

A. B. Shvidchenko and G. Pender. Initial motion of streambeds composed of coarse uniform sediments. In *Proc. Instn. Civ. Engrs. Water & Mar. Engng.*, 2000.

S.S Shy, C.Y. Tang, and S.Y. Fann. A nearly isotropic turbulence generated by a pair of vibrating grids. *Exp. Thermal and Fluid Sci.* , 14:251–262, 1997.

I. P. D. De Silva and H. J. S. Fernando. Some aspects of mixing in a stratified turbulent patch. *J. Fluid Mech.*, 240:601–625, 1992.

I. P. D. De Silva and H. J. S. Fernando. Oscillating grid as a source of a nearly isotropic turbulence. *Phys. Fluids*, 6:2455–2464, 1994.

J.E. Stiansen and S. Sundby. Improved methods for generating and estimating turbulence in tanks suitable for fish larvae experiments. *Scientia. Marina.* , 65:151–167, 2001.

B. M. Sumer and R. Deigaard. Particle motions near the bottom in turbulent flow in an open channel. part 2. *J. Fluid Mech.*, 109:311–337, 1981.

B. M. Sumer, L.H.C. Chua, N.S. Cheng, and J. Fredsoe. Influence of turbulence on bed load sediment transport. *J. Hyd. Eng.* , 129:585–596, 2003.

Tennekes and Lumley. *A First Course in Turbulence.* Manchester Institute of Technology, 1972.

H. Tennekes. Eeulerian and lagrangian time microscales in isotropic turbulence. *J. Fluid Mech.*, 67:349, 1975.

S. M. Thompson and J. S. Turner. Mixing across an interface due to turbulence generated by an oscillating grid. *J. Fluid Mech.*, 67:349–368, 1974.

J. S. Turner. The influence of molecular diffusivity on turbulent entrainment across a density interface. *J. Fluid Mech.*, 33:639–656, 1968.

S.I. Voropayev, Y.D. Afanasyev, and G.J.F. van Heijst. Two-dimensional flows with zero net momentum: evolution of vortex quadrupoles and oscillating grid turbulence. *J. Fluid Mech.*, 282:21–44, 1995.

J. D. A. Walker, C. R. Smith, A. W. Cerra, and T. L. Doligalski. The impact of a vortex ring on a wall. *J. Fluid Mech.*, 181:99–140, 1987.

S. J. White. Plane bed tresholds for fine grained sediments. *Nature*, 228: 152–153, 1970.

R.J.S. Whitehouse and J. Hardisty. Experimental assessment of two theories for the effect of bedslope on the threshold of bed-load transport. *Marine. Geology.* , 79:135–139, 1988.

P. L. Wiberg and J. Duncan Smith. Calculations of the critical shear stress for motion of uniform and heterogenous sediments. *Water Resources Res.* , 23:1471–1480, 1987.

B. Wu, D.S.V. Maren, and L. Li. Predictability of sediment transport in the yellow river using selected transport formula. *Int. J. Sed. Res.* , 23:283–298, 2008.

Y.K. Yi. *Characteristics of oscillating grid flows.* PhD thesis, Purdue University, 2002.

U.C.E. Zanke. On the influence of turbulence on the initiation of sediment motion. *Int. J. Sed. Res.* , 18:1–15, 2003.